NANOPARTICLES
FOR FOCAL THERAPY IN EARLY STAGES OF LOCALIZED PROSTATE CANCER

Inaugural dissertation

for the attainment of the title of doctor
in the Faculty of Mathematics and Natural Sciences
at the Heinrich Heine University Düsseldorf

Presented by

Maryam Youhannayee
from Rasht, Iran

Düsseldorf, August 2020

NANOPARTICLES
FOR FOCAL THERAPY IN EARLY STAGES OF LOCALIZED PROSTATE CANCER

Inaugural-Dissertation

zur Erlangung des Doktorgrades
der Mathematisch-Naturwissenschaftlichen Fakultät
der Heinrich-Heine-Universität Düsseldorf

vorgelegt von

Maryam Youhannayee
aus Rasht, Iran

Düsseldorf, August 2020

aus dem Institut für Angewandte Physik der Heinrich-Heine-Universität Düsseldorf

Gedruckt mit der Genehmigung der Mathematisch-Naturwissenschaftlichen Fakultät der Heinrich-Heine-Universität Düsseldorf

Referent: Prof. Dr. Mathias Getzlaff
Korreferent: Dr. med. Robert Rabenalt

Tag der mündlichen Prüfung: 11.08.2020

It is not because things are difficult that we do not dare, it is because we do not dare that they are difficult.

Lucius Annaeus Seneca

ZUSAMMENFASSUNG

Unter dem Begriff Nanopartikel sind magnetische Nanopartikel der interessanteste Kandidat für Diagnose und Krebstherapie. Die Wissenschaftler forschen an der Optimierung der Eigenschaften der Partikel, einschließlich der Größe, Form, Beschichtung und des magnetischen Verhaltens oder der Erwärmungseigenschaften. Der Kernschalentyp der magnetischen Nanopartikel ist ein wichtiger Faktor, der seine Internalisierung über normale und Krebszellen moduliert. In dieser Studie werden Magnetit-Nanopartikel (MNP), die mit N-(2-Aminoethyl)-3-aminopropyltriethoxysilan (Aminosilan - APTES) bedeckt sind, verwendet. Diese werden durch Kopräzipitationsmethode einer wässrigen Lösung von Eisen(III)-chlorid- und Eisen(II)-sulfat-Eisensalzen mit Ammoniumhydroxid als Basis synthetisiert. Durch APTES werden die Nanopartikel funktionalisiert, um die Lebensfähigkeit der und die Affinität zu den Krebszellen zu erhöhen. Die strukturellen und morphologischen Eigenschaften dieser Partikel werden durch Transmissionselektronenmikroskopie (TEM), Röntgenbeugung (XRD) und Fouriertransformierte Infrarotspektroskopie (FTIR) charakterisiert. Es wird ein Diphenyltetrazoliumbromid (MTT-Test) durchgeführt, um die Lebensfähigkeit der Zellen nach Behandlung mit MNP und APTES-MNP zu überprüfen. Zur Untersuchung der zellulären Aufnahme in vitro werden zwei Prostatazelllinien untersucht: PC3 als krebsartige Zelllinie und BPH1 als gutartige Epithelzelllinie (normale Zellen). Beide Zelllinien werden für 24 h mit unterschiedlichen Konzentrationen von MNP und APTES-MNP (100 und 500 μg/ml und eine unbehandelte Probe als Kontrolle) inkubiert. Anschließend werden TEM und Durchflusszytometrie-Analysen (FC) durchgeführt, um die zelluläre Aufnahme von MNP und APTES-MNP zu überwachen. Die FC-Daten weisen eine Zunahme der Granularität nach der Behandlung mit hoher Konzentration der Partikel auf. Die Resultate zeigen, dass die PC3-Krebszellen mehr APTES-MNP im Vergleich zu den gutartigen BPH1-Zellen aufnehmen. Im Gegensatz dazu korreliert die Aufnahme von MNP durch die BPH1-Zellen mit den Kontrollzellen effizienter als die von PC3-Zellen. Die Ergebnisse der FC- und TEM-Analysen veranschaulichen eine zunehmende Affinität der Nanopartikel zur Krebszellen (PC3) im Vergleich der BPH1-Zellen. Ziel des Projekts ist die Betrachtung der Affinität zwischen MNP und APTES-MNP auf PC3-Tumorzellen und gutartigen BPH1-Zellen. Dieser Ansatz könnte dazu beitragen, die Effizienz der Hyperthermie bei Prostatakrebs durch die Internalisierung von Partikeln in die Zellen oder die Assoziation an die Membran zu optimieren.

Magnetotaktische Bakterien sind aufgrund ihrer magnetischen und hochgradig gleichförmigen Eigenschaften auch ein perfekter Kandidat für die Hyperthermie. Hier haben wir versucht, die Kultivierung, Extraktion und Charakterisierung von zwei Arten von magnetotaktischen Bakterien zu optimieren. Die Größenverteilung der Nanopartikel beträgt bei beiden Bakterien etwa 20 bis 70 nm mit einer durchschnittlichen Größe von 43 nm für Magnetospirillum magnetitactic und 40,6 nm für Magnetospirillum gryphiswaldense.

SUMMARY

Among nanoparticles, magnetic nanoparticles are the most appealing candidate for diagnosis and cancer therapy. The researchers are tempting to improve the particles properties, including the size, shape, coating, and magnetic behavior or heating characteristics. Core shell type of magnetic nanoparticle is an important property that modulates their internalization via normal and cancer cells. In this study, magnetite nanoparticles (MNP) covered by N-(2-aminoethyl)-3-aminopropyltriethoxysilane (aminosilane - APTES) were synthesized by co-precipitation of aqueous solution of ferric chloride and ferrous sulfate iron salts with ammonium hydroxide as a base and functionalized by APTES to increase the viability and affinity of the particles to the cancer cells. The structural and morphological properties of these particles were characterized by transmission electron microscopy (TEM), X-ray diffraction (XRD) and Fourier transformed infrared spectroscopy (FTIR). 3-(4,5-dimethyl-2-thiazolyl)-2,5-diphenyl tetrazolium bromide (MTT assay) was carried out to check the viability of the cells treatment with MNP and APTES-MNP. To study the cellular uptake in vitro, two prostate cell lines were investigated: PC3 as a cancerous cell line and BPH1 as a benign epithelial cell line (normal cells). Both cell lines were incubated for 24 h with different concentrations of MNP and APTES-MNP (100 and 500 μg/ml and one untreated sample as control). TEM and flow cytometry (FC) analyses were subsequently carried out to monitor the cellular uptake of MNP and APTES-MNP. FC data revealed an increase in cell granularity following the treatment with high concentration of the particles. Data showed that PC3 cancer cells take up more APTES-MNP with respect to control cells than BPH1 benign cells and in contrast BPH1 cell uptake MNP correlated to control cells more efficient than PC3 cells. The results from FC and TEM analyses demonstrate increasing affinity of particles to cancer cell line (PC3). In this project we investigated the effect of surface functionalization of NP to affinity of the MNP and APTES-MNP on PC3 cells as a malignancy prostate cell and BPH1 benign cells as normal cells. This approach may help to optimize the efficiency of hyperthermia for prostate cancer through internalization of particles to the cells or attaching to the membrane.

Magnetotactic bacteria is also a perfect candidate for hyperthermia because of their magnetic and highly uniform, nanoscale crystal properties. Here we tried to optimized the cultivation, extraction and characterization of two types of magnetotactic bacteria. The size distribution of nanoparticles is about 20 to 70 nm for both bacteria with the average size of 43 nm for

magnetospirillum magnetitactic and 40.6 nm for magnetospirillum gryphiswaldense.

CONTENTS

1 INTRODUCTION

Nanoscale technology started in 1959 by Richard Feynman´s lecture by the title of "There is plenty of room at the bottom". Feynman focused on the very small size scale. By synthesis of the nanometer range materials all properties are influenced by their size and shape. But "what are nanomaterials?"
There are lots of research, publications and books, which are talking about nanomaterials. They are the intersections of different scientific major: physics, chemistry, biology and material science (Figure 1.1).

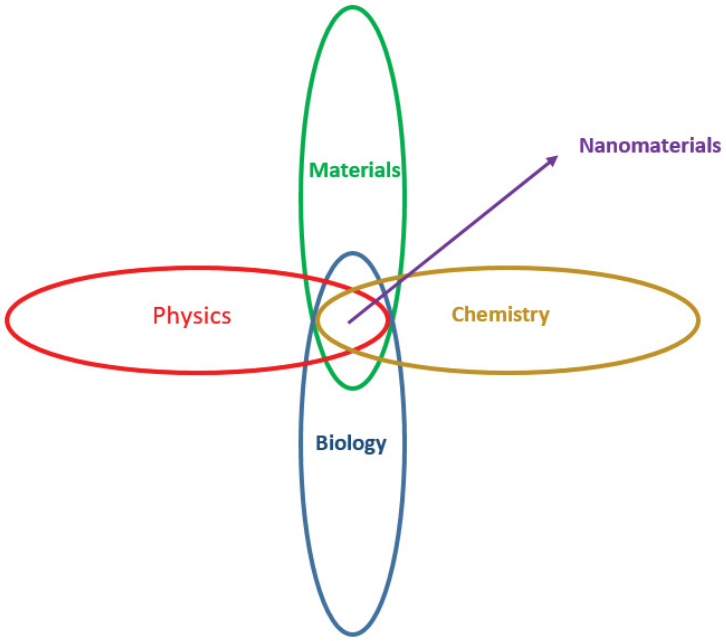

Figure 1.1: The intersection of physics, chemistry, biology and materials resulted in nanomaterials and lead this to an interdisciplinary project. The figure is based on [1].

The nanomaterials are smaller than 100 nm in all or at least in one dimension and their properties depend on their size and shape [1]. Nanotechnology is explained as an engineered systems at the molecular scale. There are two approaches in nanotechnology: *Top-down* and *bottom-up*. Top-down method definition is using the big pieces of materials in order to make smaller or planned product. Conversely, in bottom-up methods synthesizing and producing nanoparticles, nanotubes or other nano-scale product by means of atoms and molecules is

carried out. Figure 1.2 shows exemplary one bottom-up process to produce particles and other nano-sized objects.

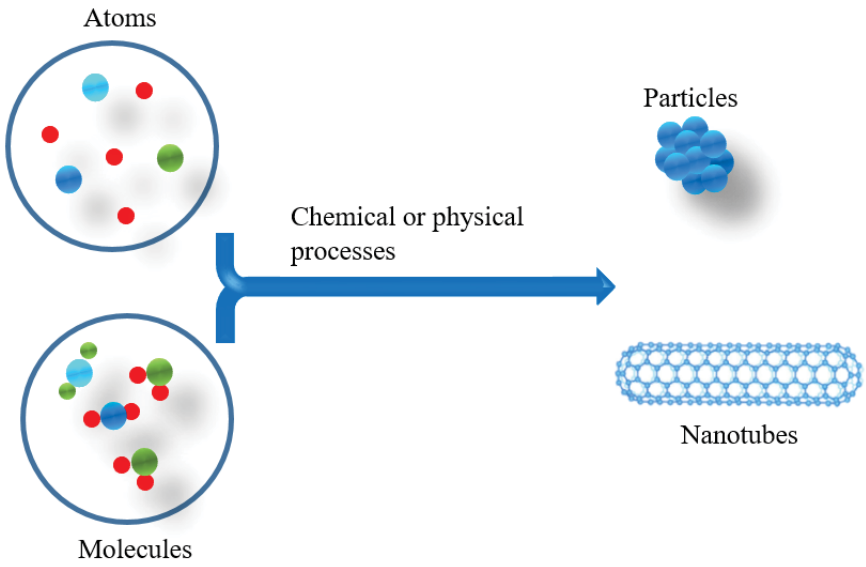

Figure 1.2: The bottom-up process is presented here by application of atoms and molecule and forming the nanomaterials such as nanoparticles and nanotubes. The figure is based on [1].

."Nano" is a prefix in "nanoparticles" word and coming from the ancient Greek language. That means smaller than the most particles. In the metric system, nanometer is the unit of length and equal to one billionth (10 Angstrom) [2].

$$1\text{nm} = 10^{-9}\text{m} \tag{1.1}$$

Applications of magnetic nanoparticles are increasing in the most research fields specifically in biological and medical branches. There are two reasons for using nanoparticles. On one hand by increasing the control in chemical and morphological design and application of different coating for colloidal stabilization. On the other hand, medicine society attitude on magnetic field applications in different medical areas such as radiology, neurosurgery and oncology. Moreover with the help of reproducible synthetic protocols, nanoparticles with the size range of 1 to 100 nm are synthesized with good quality. There are different methods for nanoparticles surface modification in order to increase the colloidal stability and also for their corrosion and dissolution. Many reasons support interests of medicine to magnetic nanoparticles. The main factor stay behind the very small size of particles. With the simple comparison, it can be understood how they can deal with organs in the body. The cell size is about 10-100 μm therefore nanoparticles are much smaller that cells. Viruses with 20 – 450 nm are somehow comparable with them. This is also true for protein (5-50 nm) and genes (2 nm wide and 20-450 nm long). That is why they can easily circulate in human bloodstream

and also very tiny lung capillaries. By circulation in the body through bloodstream they can cross cells and interact with their organelles.

This thesis: It is focused on synthesis of magnetite nanoparticles and functionalization of them with silane layer. The nanoparticles are produced by wet chemically methods (co-precipitation). Different characterizations are applied to investigate the morphological, physical and magnetic properties of particles.
Subsequently the interactions of the nanoparticles with cells are investigated to optimize the use for hyperthermia. The effect of silane coating on the particles is also considered for controlling the viability of the cells and evaluation of particles´ uptake.
As the last part, anaerobic bacteria is cultivated in order to enhance the hyperthermia effect in cancer treatment as they show promising results. Biomineralization is the way that anaerobic bacteria produces magnetite nanoparticles.

Chapters: This thesis consist of five chapters. The scientific background is explained in chapter two. Magnetism of materials and magnetic nanoparticles and specifically magnetite nanoparticles are explained. The theory behind the magnetotactic bacteria are supported in follows. In the next two sections applications of MNPs such as hyperthermia and fate of nanoparticles-cells interaction can be seen more in details.
In chapter three and four the experimental background of different instruments and the experimental set up of samples are explained respectively. The used instruments are introduced with their structure and components in chapter three like: DLS,TEM, XRD, FTIR, OEMF and VSM. Synthesis, coating of the MNPs, cell culture and all treatments for different variety of measurements are also covered in chapter four.
Finally in chapter five the results of the project are shown and discussed. The morphology and size of MNPs are defined by DLS and TEM. XRD and FTIR proved the presence of pure magnetite nanoparticles and aminosilane coating respectively. TEM and FACS are applied to evaluate the NPs uptake qualitatively and quantitatively. The viability of the prostate cells are examined after treatments by MNPs. The last section of this chapter introduces the cultivation and enrichment of magnetotactic bacteria for hyperthermia in order to be continued in other projects in the form of PhD or master project for future.

2 THEORETICAL BACKGROUND

2.1 Introduction

The background of magnetism in materials and magnetic nanoparticles will be discussed and some topics are explained such as magnetocrystalline anisotropy, magnetic domain, and hysteresis loop. In the following, iron oxide and specifically one of the most frequently used method (Co-precipitation) for synthesizing the particles will be introduced and the necessity of coating of nanoparticles will be discussed. At the end of this section, more details of the synthesis procedures and steps will be explained. The application of nanoparticles are the contents of next section, which are focusing on magnetic fluid hyperthermia in more detail. The fate of nanoparticles-cell interaction and particles uptake by the cells are the last section of this chapter.

2.2 Magnetism in materials

Where does the magnetism of solid materials come from? The answer raises from the contribution of electrons in solid structure and their quantum mechanical properties which play an important role. The magnetic moment of an electron constitutes of spin angular momentum S and orbital angular momentum L that contribute in total angular momentum J.

$$J = L + S \tag{2.1}$$

Due to the orbital angular momentum, an electron behaves like a circulating electric current which results in a magnetic moment with its associated magnetic field. Additionally, the electron has a magnetic moment because of spin angular momentum. The spin magnetic moment interacts with the orbital motion magnetic field and results in spin-orbit coupling. This interaction of electrons results in macroscopic behavior of materials in nature.

2.2.1 Types of magnetism

There are different magnetic classifications of materials on a macroscopic scale such as diamagnetic, paramagnetic and collective magnetic materials [3]. The magnetic dipole´s ar-

rangement in these materials reacts differently when a magnetic field is applied and then switched off [4, 5]. B is called magnetic induction and is actually the response of materials when an external magnetic field H is applied. The relation of H and B defines a characteristic property of materials. In vacuum this relationship is given by:

$$B = \mu_0 H \tag{2.2}$$

where μ_0 is the vacuum permeability. But materials are experiencing different magnetic induction inside and this difference is due to their magnetization M:

$$B = \mu_0(H + M) \tag{2.3}$$

As mentioned, materials have different response to an external magnetic field and are therefore divided into different magnetic classification, which is explained below. The susceptibility χ plays an important role in this classification. χ characterizes the relation between magnetization M and external field. If M and H are parallel, there is a linear relation between them and these materials are called *linear material*:

$$M = \chi H \tag{2.4}$$

Under this situation there is also a linear relation between B and H:

$$B = \mu_0(1 + \chi)H \tag{2.5}$$

$$= \mu_0 \mu_r H \tag{2.6}$$

where μ_r is the permeability which shows how the material is permeable to a magnetic field.

Diamagnetism Diamagnetic materials have no magnetic dipole without an external magnetic field but after application of a magnetic field, very small and weak induced dipoles are observed (Figure 2.1). Diamagnetic materials show purely induction effect due to an external magnetic field. By application of the magnetic field H, induced magnetic dipole are oriented antiparallel to the applied field according to Lenz' rule. Due to this antiparallel alignment the susceptibility of diamagnetic material is negative:

$$\chi^{\text{dia}} = \text{const.} < 0 \tag{2.7}$$

All the materials are showing the diamagnetic property except the materials, which exhibit paramagnetism and collective magnetism because they dominate due to their large strength.

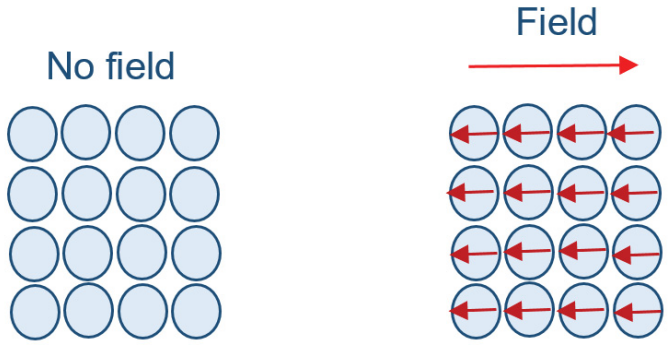

Figure 2.1: The arrangement of magnetic dipoles in diamagnetic materials is illustrated in this figure in the absence (left) and presence (right) of an external magnetic field. The figure is based on [6]

Paramagnetism The magnetic property in paramagnetic materials is mostly stronger than in diamagnetic materials. Paramagnetic materials have permanent magnetic moments which are randomly oriented and they will be all oriented in one direction by applying the external magnetic field. The thermal fluctuation can prevent these orientation. In opposite to the diamagnetic materials, paramagnetic materials are showing positive susceptibility Figure 2.2:

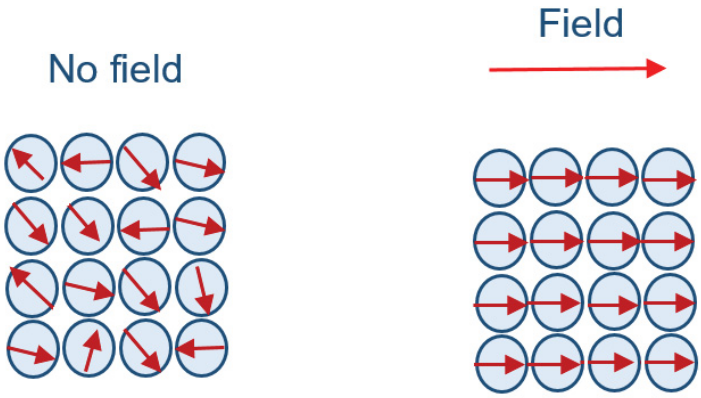

Figure 2.2: Orientation of magnetic dipoles in paramagnetic materials in the absence (left) and presence (right) of external magnetic field. The figure is based on [6]

$$\chi^{\text{para}} > 0 \tag{2.8}$$

$$\chi^{\text{para}} = \chi^{\text{para}}(T) \tag{2.9}$$

Collective magnetism The collective magnetism includes ferromagnetism, ferrimagnetism and antiferromagnetism. The susceptibility is showing very complicated functionality in comparison to dia- and paramagnetism. There are different factors, which play a role in this parameter [3]:

$$\chi^{\text{coll}} = \chi^{\text{coll}}(T, H, \text{"History"}) \tag{2.10}$$

The exchange interactions between permanent magnetic dipole are causing the collective magnetism. The spontaneous magnetization exists below the critical temperature (T_{crit}).

Ferromagnetism Ferromagnetic materials are the materials, which show spontaneous magnetization even without applying an external magnetic field, they always have magnetic dipoles oriented parallel with respect to their neighbors. Ferromagnetism exists in the temperature range:

$$0 < T < T_{\text{Crit}} = T_C \tag{2.11}$$

At $T = 0$ all magnetic moments exhibit an aligned orientation and above the Curie temperature T_C the ferromagnetic materials lose their permanent magnetic alignment.

Antiferromagnetism In antiferromagnetic materials, the adjacent magnetic moments tend to align anti-parallel to each other with the identical sublattice of magnetic moment. Therefore, the overall magnetization is zero. Below the critical temperature which is called *Néel* temperature T_{N} magnetic moments are aligned spontaneously and their neighbors with the same amount of magnetic moments aligned spontaneously in the opposite direction. In antiferromagnetic materials, the two neighbor sublattices with magnetization M_{A} and M_{A} are related:

$$|M_{\text{A}}| = |M_{\text{B}}| \neq 0 \text{ for } T < T_{\text{N}} \tag{2.12}$$

$$M_{\text{A}} = -M_{\text{B}} \tag{2.13}$$

Above the critical temperature, antiferromagnets behave similar to paramagnetic materials under application of an external magnetic field.

Ferrimagnetism The behavior of ferrimagnets are somehow similar to that of ferromagnets in a way that below the critical temperature they have spontaneous magnetization even

without presence of external magnetic field. The ferrimagnetic materials like antiferromagnetic materials have antiparallel alignment of localized magnetic moments because of exchange coupling between adjacent magnetic ions. The magnetization of one sublattice is greater than the other one which is oriented oppositely in their neighborhood. The relation of two ferromagnetic sublattices A and B with different magnetization M_A and M_B is:

$$M_A \neq M_B \text{ for } T < T_C \tag{2.14}$$

An overview concerning to collective magnetic materials are depicted in Figure 2.3.

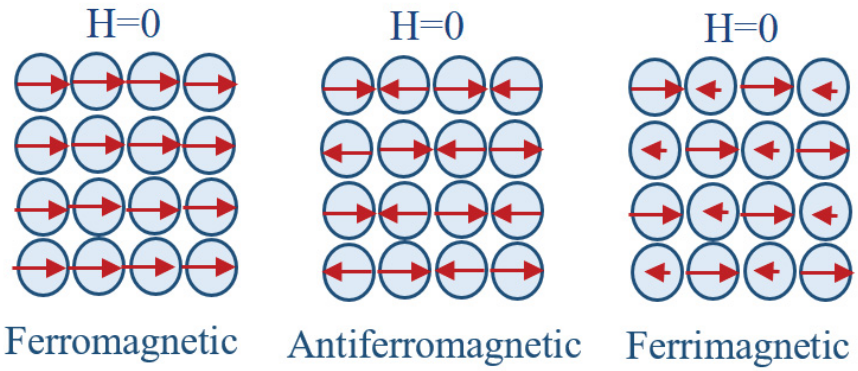

Figure 2.3: Magnetic dipoles are illustrated in ferromagnetic, antiferromagnetic and ferrimagnetic from left to right respectively in the absence of external magnetic field as published in [6]

2.2.2 Magnetocrystalline anisotropy

Anisotropy is the quality of materials specially single crystals of solid elements and components which exhibit different properties when they are measured in different directions. Shape, stress, and magnetocrystalline anisotropy are examples of this phenomenon.
Magnetocrystalline anisotropy is a natural property in all crystalline magnetic materials. The energy, which is necessary to apply to magnetize the ferromagnetic and ferrimagnetic materials is depending on the orientation of the crystal. Therefore, crystal orientation and alignment play a crucial role. In magnetic materials two different directions are distinguished: easy axis and hard axis (Figure 2.4).

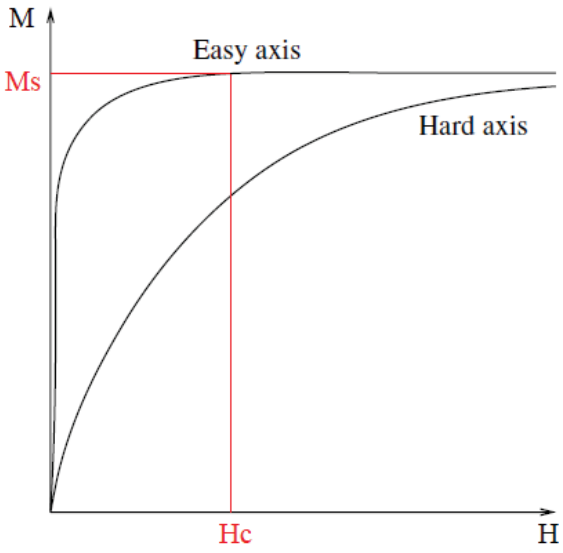

Figure 2.4: Illustration of easy and hard axes for a ferromagnet. Reprinted with permission from [7]

In ferromagnetic materials, the magnetization tends to aligned along the preferred crystallographic direction, easy axis. It is the preferred direction to magnetize the demagnetized sample to saturation point in the presence of an external magnetic field. The saturation magnetization is the same for both along the easy and hard axis but along the hard axis direction a larger external applied field is necessary to reach the saturation along easy axis. This alignment of magnetization along the preferred direction is due to the magnetocrystalline anisotropy.

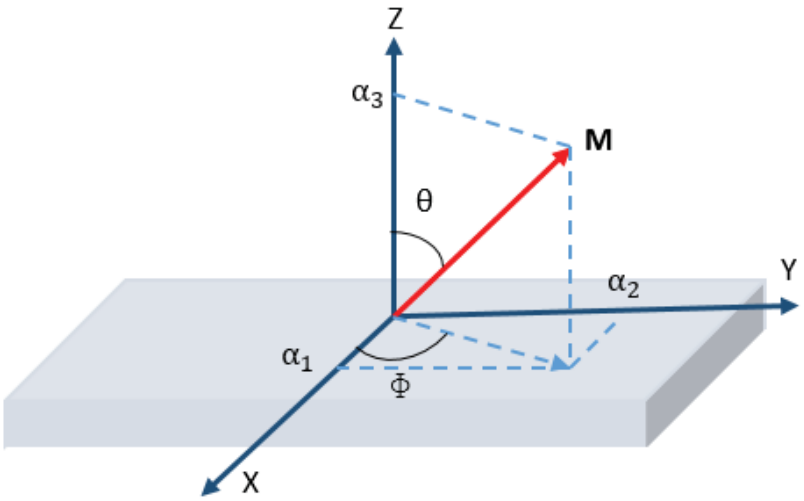

Figure 2.5: Coordinate system to describe magnetic anisotropy defining the direction of cosine. The figure is based on [3]

The spin-orbit interaction of the electrons is the origin of magneto crystalline anisotropy [3].

By application of an external field spin and orbital components need to be reoriented because of spin-orbital coupling. Cosine α_i define the direction of magnetization m with respect to coordinate axes in Figure 2.5:

$$m = \frac{M}{|M|} = (\alpha_1, \alpha_2, \alpha_3) \tag{2.15}$$

In this coordinate system α_1, α_2 and α_3 are defined as:

$$\alpha_1 = \sin\theta\cos\phi \tag{2.16}$$

$$\alpha_2 = \sin\theta\sin\phi \tag{2.17}$$

$$\alpha_3 = \cos\theta \tag{2.18}$$

Under this condition:

$$\alpha_1^2 + \alpha_2^2 + \alpha_3^2 = 1 \tag{2.19}$$

In these equations θ is the azimuthal angle and ϕ is the polar angle in a spherical coordination system.
For a cubic crystal lattice, like magnetite and iron, the anisotropy energy is given by:

$$E_{crys}^{cubic} = \mathsf{K}_0 + \mathsf{K}_1 V(\alpha_1^2\alpha_2^2 + \alpha_2^2\alpha_3^2 + \alpha_3^2\alpha_1^2) + \mathsf{K}_2 V\alpha_1^2\alpha_2^2\alpha_3^2 + ... \tag{2.20}$$

The constant magnetocrystalline anisotropy K_1 is known for most of the magnetic materials as an example for magnetite is equal to $-11 \times 10^3 \frac{\mathsf{J}}{\mathsf{m}^2}$; K_2 is rarely known and K_0 is unknown mostly [1].

2.2.3 Magnetic domains

The small region in ferromagnetic materials in which all the magnetic moments are placed parallel to each other are called ferromagnetic domains. The magnetization in different magnetic domains are aligned in spontaneous directions when the ferromagnetic materials are in demagnetized condition [7]. Most domains are aligned in the same direction at the presence of an external magnetic field. The answer of question why domains occur is raised from quantum mechanics. Electron spins are aligned due to the exchange energy

and magnetic dipole moments stay parallel to each other. The exchange energy have high tendency to align electron spins and consequently electron magnetic dipoles parallel to each other. The formation of domains minimizes the total magnetic energy of ferromagnetic materials. The other factors, which have an effect on magnetic energy are magnetostatic energy, magnetocrystalline and magnetostrictive energy, which are responsible for main driving force, shape and size domain formation, respectively [7].

The magnetized ferromagnetic material has a single domain region, which is showing a macroscopic magnetization. Due to this reason it behaves like a magnet with magnetic fields around as shown in Figure 2.6.

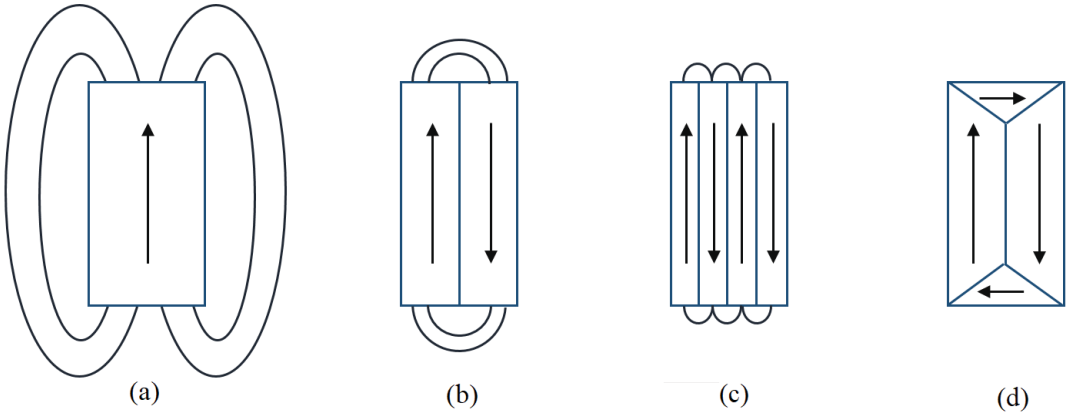

Figure 2.6: Magnetostatic energy is reduced by formation of domains in a ferromagnet material. The figure is based on [8]

As being shown in Figure 2.6, the stray magnetic fields are aligned in an opposite way of magnetic field inside the magnet and tend to magnetize the magnet in an opposite direction. That is why it is called demagnetizing field H_{d}. The magnetostatic energy, which is produced by the demagnetizing field depends on the shape of the sample. Therefore, by reducing H_{d} the magnetostatic energy can be reduced. As it can be seen in Figure 2.6 the materials with more magnetic domains has reduced external demagnetizing field.

2.2.4 Hysteresis loop

There are some characteristics that define magnetic properties of magnetic materials. The response of magnetic materials such as ferromagnetic, paramagnetic, antiferromagnetic and ferrimagnetic, to an external magnetic field is called hysteresis loop [9]. The most decisive properties are the saturation magnetization (M_{s}), remanence magnetization (M_{r}) and coercivity (H_{C}), which are obtained from hysteresis loops [9].

The relation between induced magnetic flux density B and an external magnetic field H is plotted as a hysteresis loop in Figure 2.7.

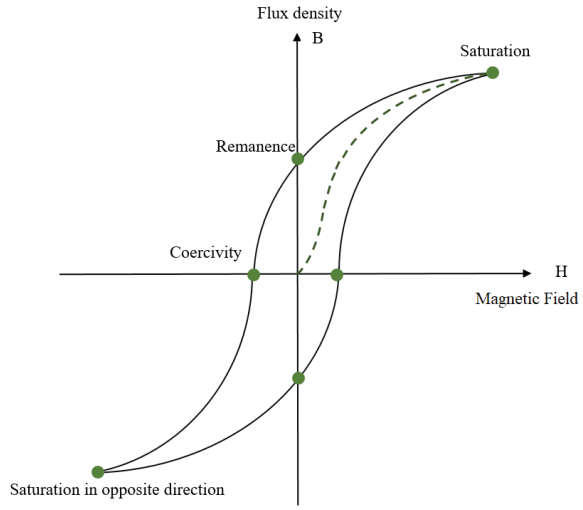

Figure 2.7: Magnetic hysteresis curve

If the magnetic field is applied to the ferromagnetic materials for the first time or ferromagnetic material is demagnetized completely, it follows the dashed line from zero point. By increasing the external magnetic field, the magnetic domains of the magnetic materials align in one direction. The saturation point is the highest value if they are all aligned in one direction. By decreasing the external magnetic field to zero, some magnetic moments still keep their alignments and the magnetic materials still show some magnetization. This phenomenon is called remanence. When the magnetic field is decreasing reversely, it meets the coercivity point H_C which has the zero induced flux. By continuing of increasing this trend in the opposite direction, the material is saturated again completely in the opposite direction. If the process continues and H decreases to zero again the residual point will cross the coercivity point. The coercivity points in both direction are equal. It is noticeable that the curve does not follow the first pathway to the zero residual magnetization, the curve is continuing to the saturation point again and completes the hysteresis loop. For the (super)paramagnetic materials, the hysteresis loop exhibits the overlap of forward and backward magnetization curves and shows no hysteresis loss.

2.2.5 Magnetism of nanoparticles

The magnetism of nanoparticles is drastically depending on shape, volume and temperature. All the interactions of atomic magnetic dipoles are the reason for this fact [6]. Bigger nanoparticles have the higher number of atoms and results in the increase of interactions of atomic magnetic dipoles. When the size of nanoparticles decrease to the critical diameter D_{C}, nanoparticles are sufficiently small to be in a single domain range. When this transition occurs H_{C} has the maximum value and largest area for hysteresis loop.

$$D_{\mathrm{C}} \approx \frac{18\sqrt{AK_{\mathrm{eff}}}}{\mu_0 M_{\mathrm{S}}^2} \tag{2.21}$$

A is exchange constant and $\mathrm{K_{eff}}$ is the effective anisotropy constant. D_{C} is achieved when the magnetostatic energy is equal to the domain wall energy. Magnetostatic energy is proportional to the materials´ volume and the domain wall energy is proportional to interfacial boundaries which are between domains [10].

Superparamagnetism Superparamagnetism exists in small enough ferromagnetic/ferrimagnetic nanoparticles which are single domain. By application of low applied fields, superparamagntic nanoparticles can be saturated with high magnetization which is one of the novel properties of these nanoparticles [6, 11]. Below the Curie temperature the magnetic domains are aligned parallel to an applied magnetic field. The superparamagnetic materials have zero remanence and coercivity. Due to this fact by removing the magnetic field magnetization direction of nanoparticles jumps easily between two stable orientations (parallel or anti-parallel easy axis orientation). There is a small energetic barrier between these two orientations.
The magnetic behavior of single domain magnetic nanoparticles is depending on two types of energy $\mathrm{K_{eff}}V$ and $\mathrm{k}_B T$. The thermal energy is comparably equal to the energy, which spins need to flip over and this leads to the random orientation of magnetic dipoles when the size of nanoparticles are in superparamagnetism area. For small and single domain particles, $\mathrm{K_{eff}}V$ is the anisotropy energy, which is concerning for alignment of all system particles in the easy axis direction. The anisotropy energy is given by [12, 13]:

$$E_a = \mathrm{K_{eff}} V \sin^2\theta \tag{2.22}$$

V is the particle volume and θ is the angle between the easy axis and magnetic moment. The two uniaxial energy at $\theta = 0$ and $\theta = \pi$ are separated with the energy barrier $\Delta E_B = \mathrm{K_{eff}}V$.

$\theta = 0$ and $\theta = \pi$ are corresponding to the parallel and antiparallel magnetization along the easy axis as shown in Figure 2.8 [11]

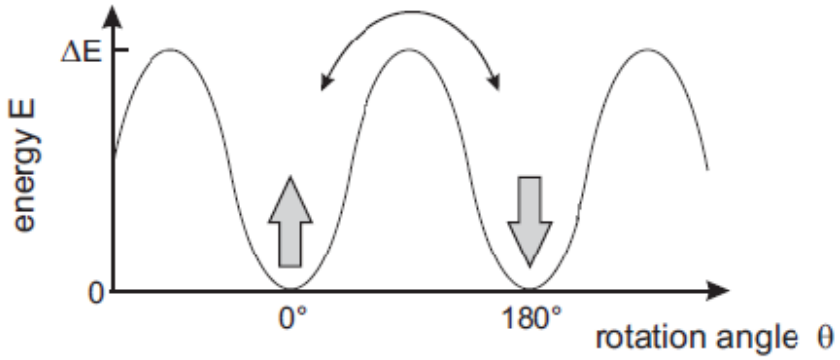

Figure 2.8: The anisotropy energy for a uniaxial particles (magnetic nanoparticles) corresponding to rotation of magnetization direction. Reprinted with permission [3].

According to Néel [14] and Brown [15] the equilibrium condition is a random process. The magnetic moment of particles fluctuate to achieve equilibrium condition with a relaxation time τ_N:

$$\tau_N = \tau_0 \exp(\frac{\mathrm{K_{eff}} V}{\mathrm{k}_B T}) \tag{2.23}$$

In this equation, k_B is Boltzmann's constant, T is absolute temperature, and τ_0 is a constant in the range of 10^{-9} s. When the anisotropic energy $\mathrm{K_{eff}} V$ is higher than $\mathrm{k}_B T$, the relaxation time is also higher than the measurement time $(\tau_N \gg \tau_m)$. This condition happens for ferromagnetic and ferrimagnetic material. On the other hand, when the size of particles is too small, the system shows $\mathrm{k}_B T \gg \mathrm{K_{eff}} V$ and the relaxation time is also small compared to the measurement time $(\tau_N \ll \tau_m)$. If $\mathrm{k}_B T \gg \mathrm{K_{eff}} V$ the materials are superparamagnetic nanoparticles. There is no hysteresis area for superparamagnetic nanoparticles in the hysteresis loop.

2.3 Iron oxide nanoparticles

There is world wide increasing attention to iron oxide nanoparticles because of their important applications specially in biomedicine. They exhibit a large variety of structures and hydration states (hydroxies and oxihydroxides) [16, 17]. Additionally, their behavior such as physical and chemical properties are dependent on size and degree of hydrations. The superparamagnetic nanoparticles are classified according to their size into superparamagnetic (SPIO) and ultrasmall superparamagnetic nanoparticles (USPIO). The SPIO and USPIO nanopar-

ticles are larger and smaller than 30 nm, respectively. Magnetite nanoparticles and their oxidation maghemite are two applicable and important families of iron oxide nanoparticles. They are used because of their high saturation magnetization, high magnetic susceptibility, and their low toxicity.

2.3.1 Magnetite nanoparticles

Magnetite nanoparticles with chemical formula Fe_3O_4 show the most fascinating properties in comparison to other iron oxide components. This is due to their chemical crystallographic structure. Magnetite consist of two iron cations, divalent Fe^{2+} and trivalent Fe^{3+}, which are placed in two valence states, in the inverse spinal structure as shown in Figure 2.9. Below 858 K the face center cubic spinel magnetite is showing ferrimagnetic properties.

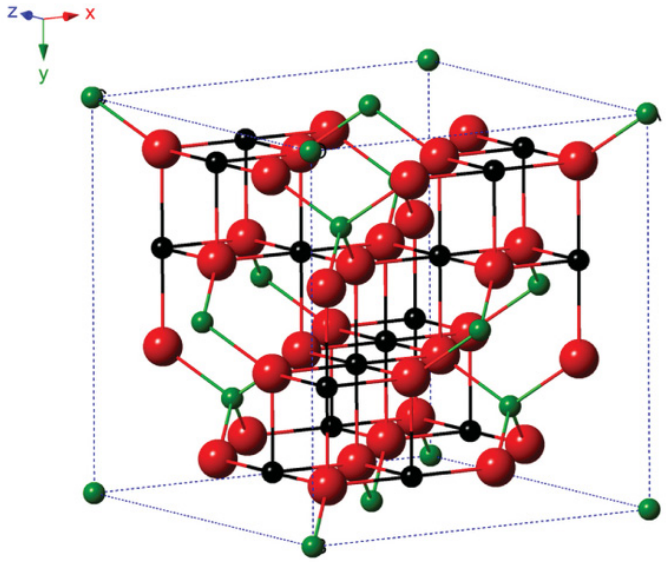

Figure 2.9: Crystal structure of magnetite nanoparticles (the black ball is Fe^{+2}, the green ball is Fe^{+3} and the red ball is O^{-2}) [9]

The cubic inverse spinel structure of magnetite Fe_3O_4 consists of cubic close packed of oxide ions along the $[111]$ direction. Half of the octahedral sites are occupied by Fe^{+2} and the rest of octahedral sites and the tetrahedral sites are Fe^{+3} [9].

2.3.2 Synthesis of iron oxide nanoparticles

In literature, a lot of different methods can be found describing the synthesis of IONPs (e.g. [18–20]). They can be divided into the chemical, physical and recently biomineralization methods. Some examples for the chemical methods to prepare the particles are: co-precipitation [21], microemulsions [22], thermal decomposition [23], sol-gel reactions [24]. Flow injection

[25], Aerosol/Vapor [26] and Pulsed laser ablation [27] are methods indicating physical type of synthesis. Magnetotactic bacteria are able to produce magnetosomes [28, 29], which is called biomineralization. In the following, co-precipitation and biomineralization methods are presented.

2.3.3 Co-precipitation synthesis

The wet chemical routes are the most and common using methods and also used in this project. Therefore, we go more in detail to describe the procedure and properties of this method. By using wet chemical methods, synthesis is simple and efficient compared to other methods and additionally there is significant control over size, shape and composition [30–32]. Iron oxides are synthesized through co-precipitation route of iron II (Fe^{+2}) and iron III (Fe^{+3}) by adding bases such as NaOH or NH_4OH [33]. The factors, which play important roles to control size, composition and shape of nanoparticles are the types of salts (e.g. chlorides, sulphates, nitrates, etc), ratio of iron salts (Fe^{+2} and Fe^{+3}) and pH and ionic strength [34, 35]. In order to synthesize magnetite Fe^{+2} and Fe^{+3} are mixed by the molar ratio of 1:2. By adding the base to the aqueous solution, the black precipitated magnetite will appear. The overall chemical reaction of iron oxide nanoparticles is [36, 37].

$$Fe^{+2} + 2Fe^{+3} + 8OH^{-} \rightarrow Fe_3O_4 + 4H_2O \tag{2.24}$$

The necessary pH for a complete precipitation is between 9 and 14. Additionally, the molar ratio of Fe^{+2} : Fe^{+3} must be 1:2 in an oxygen-free environment. If these conditions are not provided, iron oxide will be oxidized. The chemical reaction of oxidation is according to [18, 38]:

$$4Fe_3O_4 + O_2 + 18H_2O \rightarrow 12Fe(OH)_3 \tag{2.25}$$

The oxidation changes the physical and chemical properties of magnetic nanoparticles. In order to control and prevent the oxidation of magnetic nanoparticles, coating (will be explained in the next section) with organic and inorganic molecules would be a good solution. The flowing of the N_2 gas during the synthesis also controls the kinetic of the reaction which significantly affects the oxidation speed of different types of iron oxide nanoparticles. The experimental results of Kim et al. [38] have shown that the application of N_2 gas protects the nanoparticles from critical oxidation. Also a decrease of particles´ size was observed. Therefore, flowing N_2

gas and coating the particles are two ways for preventing of more oxidation.

2.3.4 Nucleation and growth mechanism

The nucleation and growth procedure are two steps in the synthesis of the particles. Nucleation is the process of new crystalline entity formation [39]. The irreversible clusters (nuclei or critical nuclei) are produced by rearrangement of the reactant atoms or molecules [40]. To have better mono-dispersed particles, these two steps have to be separated from each other. To reach this condition nucleation must occur in a short time. If the nucleation takes a long time, there could be an overlapping between the nucleations and the growth procedure. This results in a wide range of particles´ size distribution. To consider the homogeneous nuclei thermodynamically, the total free energy is defined as a summation of the surface free energy ΔG_S and the crystal free energy ΔG_V [41]:

$$\Delta G = \Delta G_S + \Delta G_V \tag{2.26}$$

$$\Delta G = 4\pi r^2 \gamma + \frac{4}{3}\pi r^3 \Delta G_v \tag{2.27}$$

r is the radius for spherical particles, γ the surface energy and ΔG_v the free energy of bulk crystal. ΔG_v is a function of temperature T, S is the entropy, and molar volume v

$$\Delta G_V = \frac{-\mathsf{k_B} T \ln(S)}{v} \tag{2.28}$$

The critical size is the smallest size of a cluster constituted of atoms or molecules which is formed in nucleation processes. The critical radius r_{crit} can be obtained by differentiation of ΔG with respect to r:

$$r_{\mathsf{crit}} = \frac{2\gamma\nu}{\mathsf{k}_B T \ln(S)} \tag{2.29}$$

The surface free energy and the crystal free energy are positive and negative, respectively. Figure 2.10 shows the changes of crystal free energy, surface free energy and total free energy as a function of the radius. It can be seen that under the critical size r_{crit} the nuclei are stable. They are dissolved into the solution with the size smaller than critical size in order to decrease the overall free energy and they grow up when their size are higher than critical value.

The second step, the growth procedure will increase the size of particles. During this proce-

dure intermediate species and growing particles both exist in the solution. The procedure is finished when the precursor or reagent are consumed. By following of the growth step in high temperature annealing, the better crystallinity can be achieved. The Oswald ripening occurs if the high temperature annealing is applied for a longer time [1].

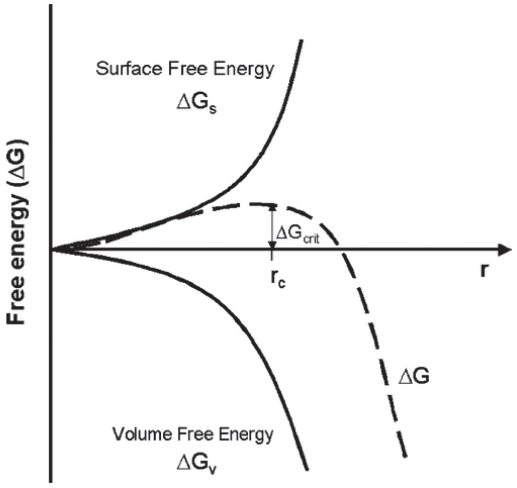

Figure 2.10: Free energy diagram for nucleation, showing dependency of volume free energy, surface free energy and total free energy to the radius.Reprinted with permission from Ref [42] Copyright 2009 American Chemical Society.

LaMer mechanism The Lamer mechanism is often used to describe the nucleation and growth procedure of nanoparticles´ synthesis. As depicted in Figure 2.11, there are three steps to explain the nucleation and growth process through the LaMer mechanism. The monomers are explained as reacted species which are dissolved in the solution to the particles or attach them:

(I) In this step, the monomers are produced and supersaturated and still no particles are formed.

(II) By increasing the monomer concentration to the critical value of supersaturation C_m, bursting the nucleation occur and the concentration of monomers is reduced significantly. When the nucleation occurs, it results in decreasing the concentration of monomers below C_m.

(III) In the last step, nucleation is stopped and the particles are formed and grown.

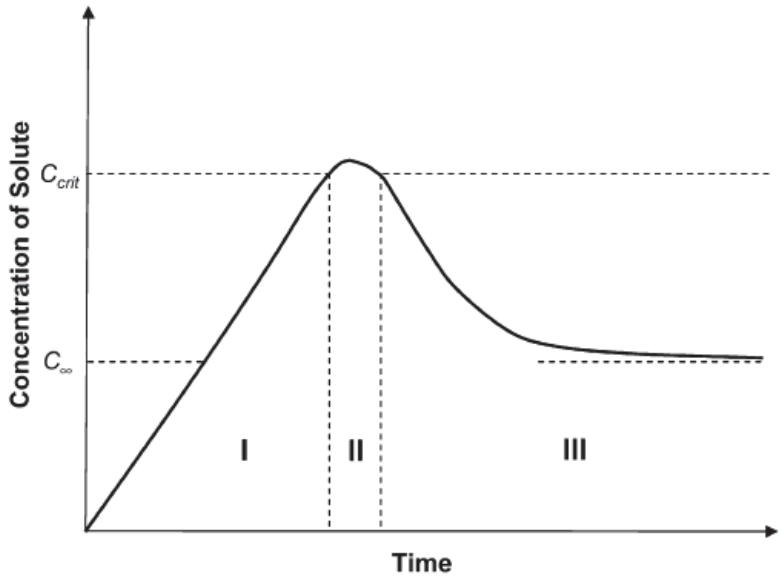

Figure 2.11: LaMer diagram illustration explaining the process of monodisperse particles´ formation. The regions I, II and III are defined as the prenucleation, nucleation, and growth stages, respectively [43]. Reprinted with permission from ref [43] Copyright 2007 Elsevier.

2.3.5 Stabilization (coating) of magnetic nanoparticles

The magnetic nanoparticles have a significant surface energy due to a high surface to volume ratio. Therefore, they minimize the energy and tend to agglomerate. Additionally, as mentioned in the last section, uncoated particles have a high chemical activity and would be oxidized easily in a short time.

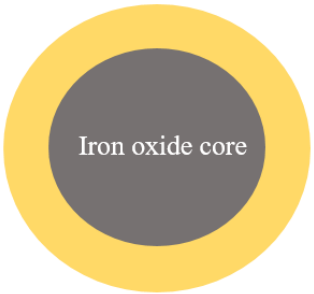

Figure 2.12: Core-shell structure of functionalized iron oxide nanoparticles. Iron oxide is assumed as the core

All these factors can result in losing magnetic properties and particles dispersibility. To overcome these problems, particles´ coating and functionalization provide the effective strategies to protect the particles (Figure 2.12). These strategies result in NP stability, protecting in oxidation, increasing viability etc. The modifications of iron oxide nanoparticles are carried out by organic or inorganic materials [44].

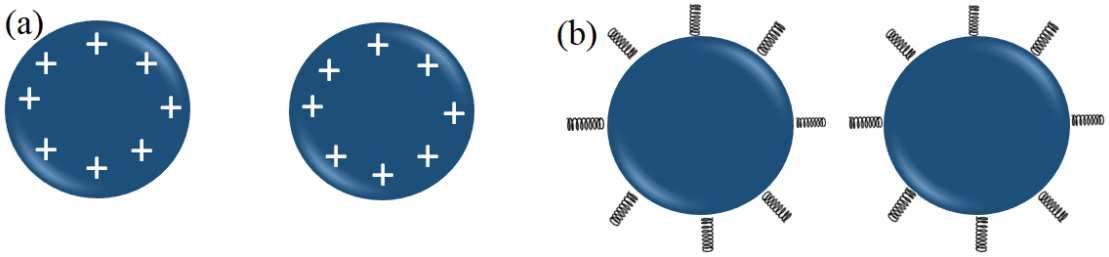

Figure 2.13: Illustration representing particles stabilized by electrostatic layer (a) and steric repulsion (b). Figure is based on [20]

The attractive forces between the particles are like van der Waals forces and magnetic dipole interaction cause this aggregation [20]. Electrostatic or steric repulsion forces play an important role in stabilization of magnetic nanoparticles. Therefore, stabilization can be achieved by modifying these factors as it is presented in Figure 2.13 [20, 37].

Organic monomeric coating The monomeric functional groups include carboxylates, phosphates and sulfates. They are well known because of binding to the surface of magnetite [17]. Carboxylates are stated in the literature as the best coating materials.

Organic polymeric coating Organic polymeric materials have been widely used for coating and stabilization of magnetic nanoparticles. Extensive work has been reported to stabilize iron oxide nanoparticles through *in situ* and *post-synthesis* coating with polymeric materials. The *in situ* process is explained as coating the particles during the synthesis of particles like development of co-precipitation method by dextran coating [45]. The *post-synthesis* occurs after synthesis of nanoparticles in an individual second step [20]. Dextran, carboxymethylated dextran, carboxydextran, starch, arabinogalactan, glycosaminoglycan, sulfonated styrene-divinylbenzene, polyethylene glycol (PEG), polyvinyl alcohol (PVA), poloxamers, and polyoxamines are the most often used polymeric coating, that are in the synthesis process [46, 47]. One of the material, which is used frequently is polyethylene glycol (PEG) due to its hydroxyl terminal group. It is also used to connect other biological groups to the surface of nanoparticles [19].

Inorganic coating A variety of inorganic materials are applied to coat the particles. The most important inorganic materials include silica [48–50] and gold [51, 52]. These nanoparticles are made of an iron core surrounded by an inorganic shell [20]. These coatings have two advantages: the first is increasing the stability of particles in a solution and the second by

application of this coating the possibility of binding various biological ligand is increased [20]. Normally, using an inert silica coating is preventing magnetite nanoparticles from agglomeration and improving its chemical stability. Additionally, the silica coating is providing better protection against toxicity, which results in increasing the viability of magnetite nanoparticles [53]. The silica shell increases the Coulomb repulsion between nanoparticles.
The advantage of a silane group (Figure 2.14) on the surface of magnetite nanoparticles is the easy reaction of this group with the wide variety of coupling groups by covalent forces [54, 55]. One of the most frequent example is amine groups which has been introduced by hydrolysis synthesis process to the silica coated magnetite nanoparticles. One of this example is aminopropyltriethoxysilane [56–58] which was also applied in this project. This method which uses aminosilane agent group is known as a silanization method [20].

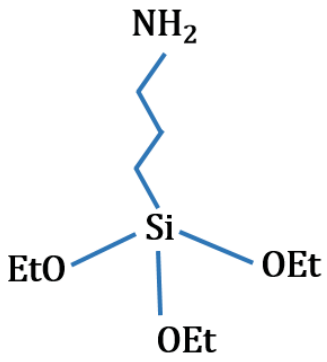

Figure 2.14: Aminosilane agent group. Figure is based on [59]

Aminosilane coating The aminosilane coated nanoparticles are synthesized and discussed in this project. Therefore, we go in more detail concerning aminosilane coating.
The silane group is an organic functional group and used for direct surface modification. Moreover, they show very high biocompatibility. Comparing to the other coating agents, they have high density of surface functional end-groups and furthermore other polymer, metal and biomolecules can connect to their surface [60, 61]. The physical characterizations of NP do not change due to the functionalization (coating). Saturation magnetization decreases less than 10 emu.g^{-1} [20]. The 3- aminopropyltriethyloxysilane (APTES) is used to provide an amino group. The average diameter of surface functionalized nanoparticles have a slight increase while maintaining the saturation magnetization of naked iron particles. The morphology of particles is retained the same by APTES agent compared to other silane groups. The coated silane agent forms the protective layer around the particles against slight acid and alkaline environment. The particles have to be water-dispersible, therefore, can be ready for biological applications. The silane group provides highly stable and water dispersible nanopar-

ticles through silane ligand-exchange [59].
As far as the magnetite nanoparticles have the huge surface-to-volume atomic ratio, they present high surface activity and large amount of dangling bonds on the surface of nanoparticles. Therefore, they (the atoms on the surface) tend to adsorb the ions and molecules existing in the solution [61]. The iron Fe and oxygen O bare atoms in a neutral solution will adsorb OH^- and H^+ and consequently the number of -OH on the surface will increase. That results in the reaction of -OH with APTES on the surface [61]. Due to this chemical reactions, magnetite nanoparticles can be coated (Figure 2.15).

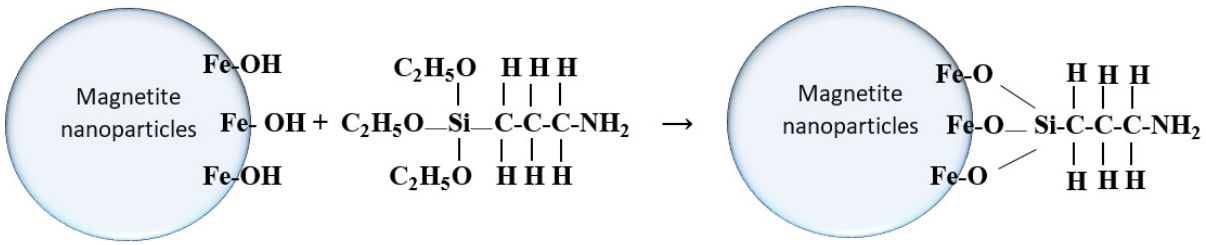

Figure 2.15: The coating reaction of magnetite nanoparticles with APTES. Figure is based on [61]

2.3.6 Surface of nanoparticles

As mentioned in the last section, nanoparticles have a high surface-volume ratio, and this causes aggregation of these small particles. By decreasing the size of particles they earn a huge surface area. In the following, the ratio of surface to volume of the geometric variable is obtained. Therefore, A is defined as a surface of one particle and d the diameter of the particles:

$$A = \pi d^2 \tag{2.30}$$

V is also considered as the volume :

$$V = \frac{\pi}{6} d^3 \tag{2.31}$$

The ratio of surface to volume R is obtained as:

$$R = \frac{A}{V} = \frac{6}{d} \tag{2.32}$$

This ratio is inverse proportional to the size. Consequently, by decreasing the nanoparticles´ size the ratio of surface to volume increases and this causes a high surface energy. To decrease this high energy, nanoparticles tend to aggregation and agglomeration [1].

2.4 Magnetotactic bacteria (MTB)

Aquatic bacteria were discovered for the first time in the early 1970s in mud collected by Richard Blakemore [62]. It has been shown that many prokaryotes build the intracytoplasmic compartments, which have a very complicated structure [63]. The magnetosomes of Magnetotactic bacteria (MTB) are one of the most attractive and fascinating examples of MTB compartment and the key component of these kind of bacteria. The magnetosomes have interaction with Earth's magnetic field and due to this work like a navigational device for magnetotaxis [64]. The process of formation the magnetosomes is called biomineralization.

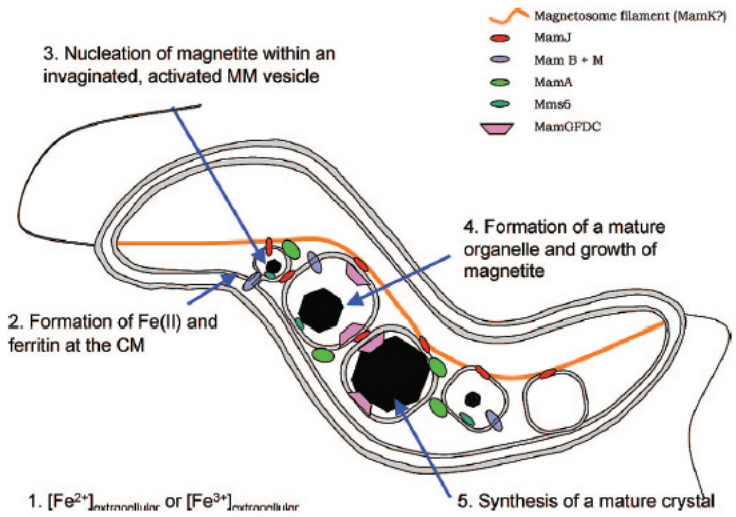

Figure 2.16: Magnetosome biomineralization pathway. Reprinted with permission from ref. [65]. Copyright 2008 American Chemical Society.

Iron biomineralization are formed in variety type of the organisms. The biomineralization of magnetic minerals (Figure 2.16) in the form of magnetosomes is one of the attractive form of biological synthesis of iron minerals [65]. The magnetotactic bacteria have the variety of different types with respect to their morphology, physiology, and phylogeny. Different cells´ morphology are rods, vibrios, spirilla, cocci, ovoid bacteria, giant and multicellular MTB [66]. The bacteria have motion by means of flagella. Their cell wall structure consists of Gram-negative bacteria [66].

There are a minority of MTB which are well known and can be cultured in laboratory environment [67], Magnetospirillum magnetotacticum strain $MS-1$ [68], M.gryphiswaldense $MSR-1$ [68, 69], and M. magneticum strain $AMB-1$ [70, 71]. Biomineralization consists of a very complex mechanism for synthesis of magnetosomes. The process includes uptake, accumulation, and precipitation of iron [63]. The ferrimagnetic iron mineral magnetite Fe_3O_4 is the most often synthesized interacytoplasmic crystal. The synthesized magnetite nanopar-

ticles in bacteria have the perfect crystalline and narrow size distribution with the average size of 35-120 nm [72]. For the synthesis and the biomineralization of magnetite, iron assimilated efficiently from low concentration in growth environment [63]. The magnetite nanoparticles are arranged in a magnetosome chain-like structure and are enveloped by the magnetosome membrane (MM) made of trilaminate structure [73]. For the formation of magnetite nanoparticles in the solution the presence of mixed valence iron complex is required. The synthesis of magnetite nanoparticles in cultured medium depends precisely on iron supersaturation, redox potential and pH [63]. Figure 2.16 shows the biomineralization pathway in bacteria.

2.5 Application of magnetic nanoparticles

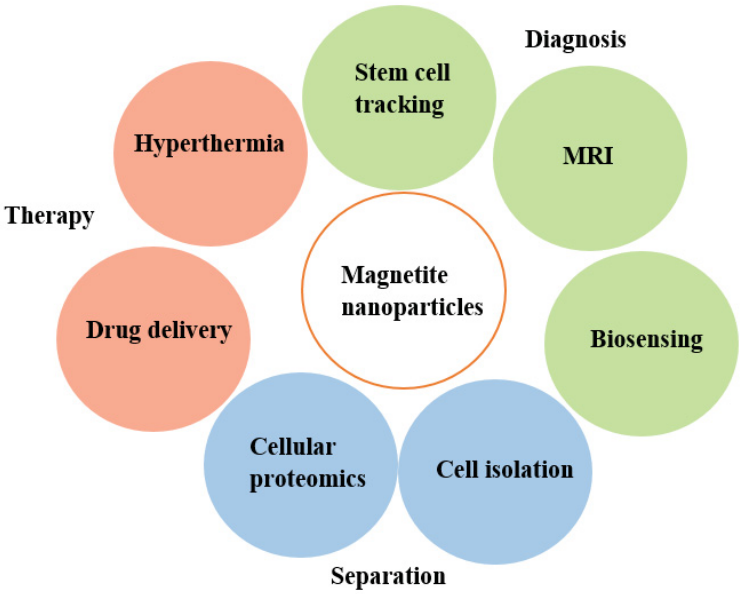

Figure 2.17: Biomedical applications of magnetic nanoparticles.

In recent years, synthesis of superparamagnetic nanoparticles has been world wide intensively increased and developed due to the industrial, technological, biological and medical applications (Figure 2.17). The technological applications are for example: magnetic storage media [74] and biosensing application [75]. Medical application are targeted drug delivery [76, 77] and contrast agent in magnetic resonance imaging (MRI) [78, 79]. Superparamagnetic iron oxide nanoparticles with different surface functions have more applications in *in-vivo*. Such applications include MRI contrast enhancement, immunoassay, tissue repair, drug delivery, cell separation, and hyperthermia [18].

2.5.1 Magnetic fluid

Superparamagnetic nanoparticles have worldwide application in variety of fields [6]. They were used to control the fluid in the space for the first time at the national aeronautical and space administration (NASA) [80]. They are colloidal suspensions consisting of superparamagnetic nanoparticles. Similar to superparamagnetic materials, they are showing the same properties by an application of an external magnetic field and that is why they found more applications in medical and industrial sectors.

2.5.2 Hyperthermia

Hyperthermia (Figure 2.18) is one of the most feasible method for cancer treatment, which is showing very low side effects.

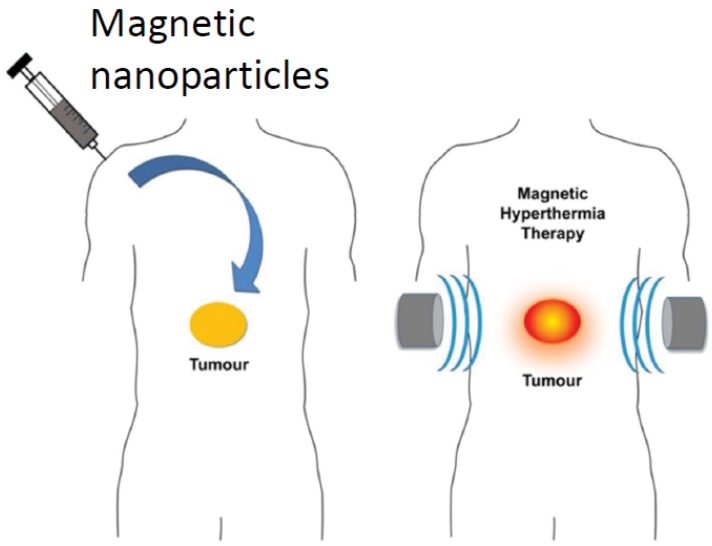

Figure 2.18: Hyperthermia. Reprinted with permission from Ref. [81].

The improved results are shown *in vivo* and *in vitro* experiments by combining hyperthermia with other therapies [10]. Some methods are developed in hyperthermia for the cancer treatment in order to increase the temperature of cancer tumor cells [82, 83]. The cancer cells are too sensitive to high temperature and due to the hyperthermia the viability of the cancer cells decreases while the sensitivity of them increases to chemotherapy and radiation.
It is normally carried out above the physiological temperature 37 ℃ in the range of 42 to 46 ℃ and called mild hyperthermia. The tumor cells are hypoxic and poorly oxygenated comparing to the normal cells, which are euoxic and well oxygenated and due to their sensitivity to higher temperature, cancer cells are killed while the normal cells survive. Additionally, they are not capable of dissipating the heat like normal cells due to the insufficient blood supply in comparison to the normal cells [10]. Some cell morphological changes are observed through *in*

vitro hyperthermia [10]. Hyperthermia has been successfully used for some recurrent cancer diseases such as breast, head, neck and skin malignancies [84].
Hyperthermia can be applied in two different temperature regimes:
1. The temperature increases moderately up to 42 to 43 ℃. This is known as an adjacent method to increase the effect of radiation and chemotherapy effect and induction of some degree of apoptosis [84, 85]
2. The second route is by enhancement of the target temperature above 46 ℃, which is defined as $thermoablation$

Methods to enhance the temperature Local hyperthermia, interstitial and endocavitary, regional and part-body and whole body hyperthermia are the different methods, which are used to increase the temperature in the body [86].

The hyperthermia modalities are dependent on some different factors. The heating source and the type of cancer play a significant role to select the modality. The hyperthermia modalities include external sources like hot bath, wax and blanket, sources without any contact to tumor such as radiofreqency, ultrasound, microwave, and infrared device and the last modality includes the heat sources, which are transferred to and inserted into the body like probes antenna, laser fibers, and mediators [87].

2.5.3 Magnetic fluid hyperthermia (MFH)

In Magnetic Fluid Hyperthermia (MFH) method the temperature of solution increases by applying an alternating magnetic field on magnetic materials such as superparamagnetic nanoparticles. The significant advantage and concept of this method are the local heating of the malignant cells without effecting normal cells by local application of magnetic field to the tumor tissue [84, 88, 89]. For the first time in 1957 Gilchrist *et al*. [90] heated the variety of tissues by $\gamma - Fe_2O_3$ under applying of 1.2 MHz magnetic field. There are lots of research that have been reported the application of magnetic fluid hyperthermia under different tested parameters such as various type of magnetic materials, different magnetic field strength and frequency [91–94]. The Charite research group in Berlin, Germany tested for the first time the clinical application of MFH on human patients [95].

Some limitation also should be considered concerning to the range of frequency f and amplitude:

$$f = 0.05 \sim 1.2 \text{ MHz} \tag{2.33}$$

$$H = 0 - 15 \text{ k Am}^{-1} \text{ (up to } \sim 18.85 \text{ T)} \tag{2.34}$$

Due to the deleterious physiological responses, frequency and the strength of the magnetic field should not exceeded these ranges [92, 96]. Some of these deleterious physiological responses include stimulation of the peripheral and skeletal muscles, cardiac stimulation, arrhythmia and nonspecific inductive heating of tissue. It has been depicted experimentally that the safe area for AC field is about:

$$H * f < 4.85 * 10^8 \text{ A m}^{-1}\text{s}^{-1} \tag{2.35}$$

The efficiency of the heating is depending significantly on the particles` magnetic properties. According to this, ferromagnetic single domain and multidomain superparamagnetic nanoparticles can be used for magnetic fluid hyperthermia.

2.5.3.1 How to deliver MNP to the tumor

There are four ways for delivering magnetic nanoparticles to the tumor:

1. Injection to the artery The magnetic fluid, which is containing the magnetic nanoparticles particles can be injected to the artery which is supplying the tumor cells. Therefore, this arterial pathways is conducting the particles to the tumor.

2. Directly injection of MNP to the tumor By injecting the nanoparticles directly to the tumor, they are placed in the tissue and its interstitial spaces. There is also the possibility of small part of particles diffusion in blood vessels and intracellular spaces [95]. Therefore, the temperature outside the cells increases by applying the magnetic field. The experiments by specific coating with antibodies are resulted in selectively up-taking the particles by tumor cells and less uptake by normal cells [97–99]. Thus, the coating increases the maintenance of NP in tumor and results in optimizing the hyperthermia effect.

3. In-situ implant formation Magnetic nanoparticles are entrapped by the gels. The injectable formulation form of this gel can be injected to the tumor [100].

4. Active targeting The antibody targeting [101] and the magnetic targeting [102] by means of an external magnetic field are complicated methods to enrich the tumor by nanoparticles. In

antibody targeting, the nanoparticles are coated by specific tumor antibodies and injected to the vessels. They find their way to bind to the tumor. This is the same for magnetic targeting. By injecting the magnetic nanoparticles to the vessels and applying an external magnetic field near the tissue, MNP in blood stream circulation are attracted to the tumor [103].

2.5.3.2 Mechanisms of heat generation

Magnetic nanoparticles can generate the heat by applying an external magnetic field due to the process of magnetic losses. The heat is produced due to the reversal magnetization process in the particles system. The losses include: hysteresis loss, Néel and Brown relaxation, and frictional losses in viscous suspensions [104]. According to Rosenzweig [105] heat generation is based on rotational relaxation and eddy current can be neglected for the particles smaller than 20 nm. The heat generation is strongly size dependent and the time constant of relaxation process also affected by the size. The bigger particles have the higher Brownian and Néel relaxation time constant. The faster relaxation time the more dominant is the dissipation process [103].

The specific absorption rate (SAR) or specific loss power (SLP) is the main parameter to determine the heating of the tissue. It is defined as the electromagnetic energy rate, which is absorbed by the unit mass in the biological materials. The unit for adiabatic condition is Watt per kilogram, which is proportional to the temperature increase rate:

$$SAR = 4.1868\frac{P}{m_e} = \mathrm{C}\frac{dT}{dt} \tag{2.36}$$

P is equal to electromagnetic wave power absorbed by the sample, m_e is the mass of sample, C is the heat capacity of medium and $\frac{dT}{dt}$ is the rate of temperature.
SAR of ferrofluid and its magnetic relaxation are related [106]:

$$SAR = 4.1868\pi\mu_0^2\frac{\varphi M_S^2 V}{1000kT}H_0^2\nu\frac{2\pi\nu\tau}{1+(2\pi\nu\tau)} \tag{2.37}$$

V is defined as the volume of superparamagnetic material, ν considered as frequency of AC magnetic field, H_0 is the magnetic field intensity and τ is the relation time. As it can be seen in the equation, SAR is strongly dependent on the nature and the specific amount of the volume.

2.5.3.3 Mechanisms of heat dissipation

The Brownian relaxation mechanism is given when the magnetic moments of particles and the crystal axis are aligned in the same direction and rotate together. Therefore, by applying

the magnetic field the magnetic moment of the nanoparticles and the particles themselves rotate simultaneously [104].

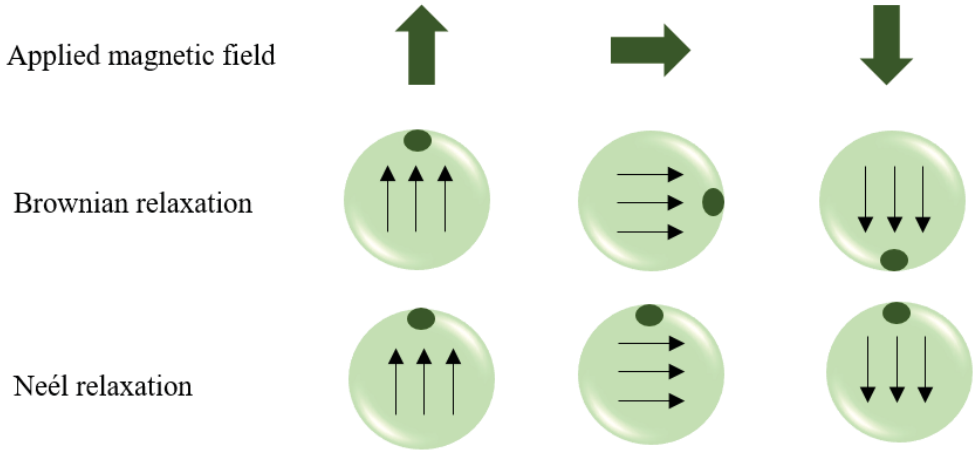

Figure 2.19: Brownian and Néel relaxation.

The Néel relaxation is found when the magnetic moments rotate with respect to the crystal. The Néel relaxation time (τ_N) and the Brownian relaxation time(τ_B) are given by:

$$\tau_N = \tau_0 e^{\frac{\mathsf{K}_{\mathsf{eff}} V_M}{\mathsf{k}_B T}} \tag{2.38}$$

$$\tau_B = \frac{3\eta V_H}{\mathsf{k}_B T} \tag{2.39}$$

$$\tau = \frac{\tau_B \tau_N}{\tau_B + \tau_N} \tag{2.40}$$

$$\frac{1}{\tau} = \frac{1}{\tau_B} + \frac{1}{\tau_N} \tag{2.41}$$

τ is typically in the range of $10^{-9}s$, τ is the effective relaxation time when the Brownian and Néel relaxation occur at the same time, $\mathsf{K}_{\mathsf{eff}}$ is the anisotropy constant, V_M is the volume of the particles, T the temperature, η the viscosity, and V_H the hydrodynamic volume of the particle.

As it has been seen in these equations, the size plays a crucial role for the relaxation time. If the magnetic reversal time is less than particles` magnetic relaxation time under AC field

application, the heat dissipation appears due to the delay of magnetic moment relaxation [103].

2.6 Fate of nanoparticles-cell interaction

Despite the fast and advanced development research and products in nanotechnology and nanoscience, relatively little is known about nanotoxicology and the fate of nanoparticles concerning their interactions with cells [10, 107]. In the last sections, the synthesis, properties and the application of magnetic nanoparticles have been explained. Herein, we focus more on the fate and interaction of nanoparticles on the cells. The importance of this issue arises from the direct exposure of nanoparticles to the cells and considers the toxicity of them. The toxicologist is investigating more the factors that explain the fate and biological reactivity of particles. The cell types and their different states play a crucial role in nanoparticles` uptake [107]. These important characteristics of nanoparticles include size, surface area, shape, bulk chemical composition (crystal structure), surface chemistry (including charge and coating) and the surface reactivity [10, 108–110]. The mechanism behind the nanoparticles` systematic toxicity is attributed to oxidative stress.

2.6.1 Internalization by endocytosis

Nanoparticles have interactions with cells, cellular components, bacteria, and viruses. They can enter the cells because of their small size. All the living cells are protected from their surrounding environment with the plasma membrane. The foreign objects can enter selectively and effectively through the plasma membrane [111]. Therefore, nanoparticles have to overcome this barrier to introduce themselves to the cells [112]. The term endocytosis implies uptake and internalization of nanoparticles to the cells due to their interactions together [10]. Multiple stages are participating in this process. Pinocytosis (cell drinking) and phagocytosis (cell eating) are two subgroup of endocytosis (Figure 2.20). By pinocytosis, fluid and molecules are internalized by small vesicles to the cells and by phagocytosis the large particulate matter are internalized to the cells such as monocytes/macrophage, neutrophils and dendritic cells [113]. Pinocytosis is also divided into four different basic categories, which include macropinocytosis, clathrin-mediated endocytosis, caveolin-mediated endocytosis and clathrin- and caveolin-independent endocytosis [114]. These mechanisms have the specific effect in intracellular trafficking and the fate of nanoparticles in the cells [113].

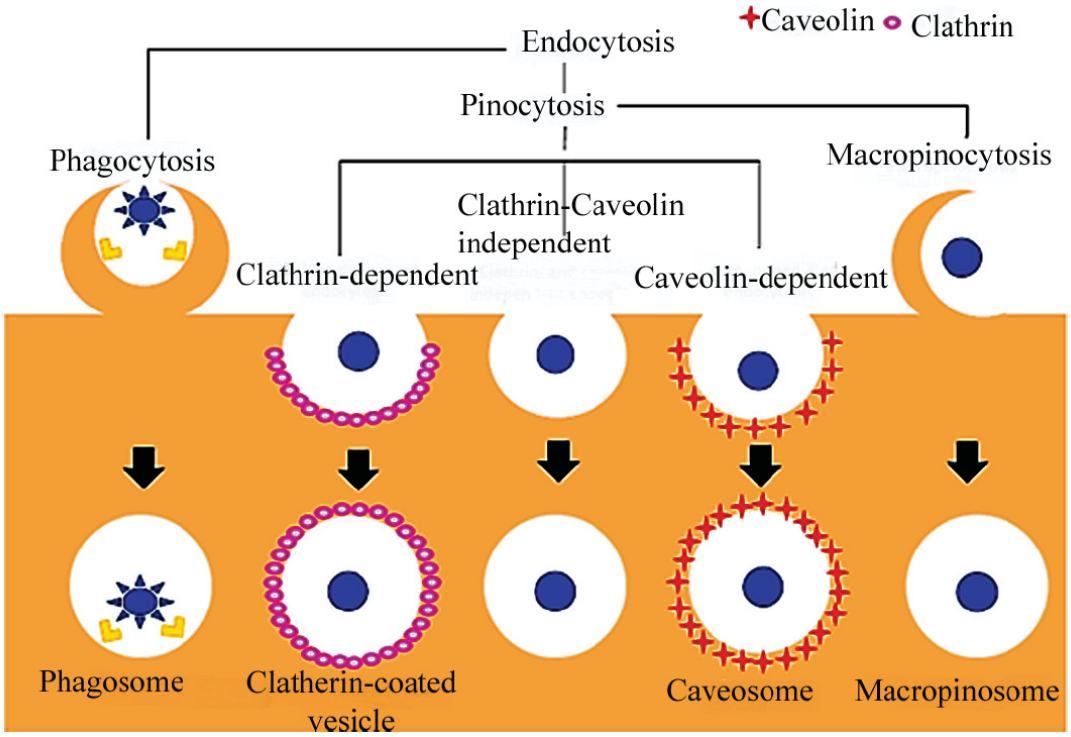

Figure 2.20: Illustration of main pathway for internalisation of nanoparticles [115]. Reprinted with permission from ref [115] Copyright 2017 journal of cellular and molecular medicine.

2.6.2 Characteristics affecting nanoparticles` uptake

The nanoparticles` characteristics that affect their uptake efficiency are size, shape, charge, and the surface modification (coating) [116]. Additionally, culture medium and cell-specific uptake properties are also some of the important factors that affect the internalization of nanoparticles [117]. By optimizing the physiochemical parameters, the efficiency of nanoparticles´ uptake can be improved [118].

Size By decreasing the size of nanoparticles, the nanoparticles` uptake by the cells increases [119]. The reduction of the nanoparticles` size increases the ratio of the surface to the volume of the nanoparticles, therefore they obtain higher contact with the biological membrane of the cells [120].

Shape Similarly, the shape of particles affect their cellular biodistribution (Figure 2.21), blood residence time and nanoparticles` uptake [116]. It is reported [121] on the higher efficiency of elongated nanoparticles in adhering to the cell in comparison to the spherical nanoparticles. The reason behind this is the higher surface area, that results in a higher ability of the nanoparticles interaction with the cell surface [121].

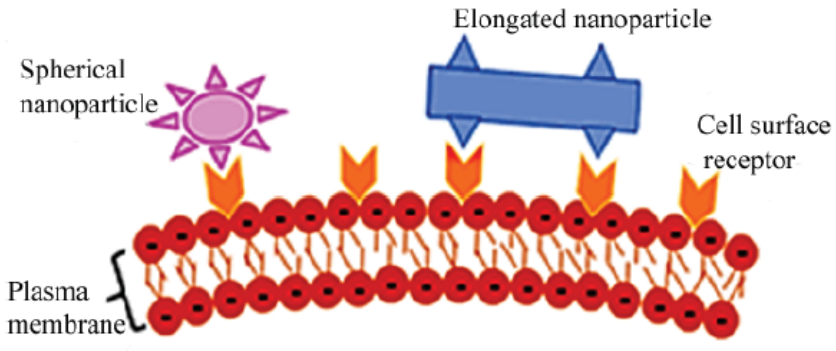

Figure 2.21: The illustration of nanoparticles` shape effect on nanoparticles-cell interactions [115]. Reprinted with permission from ref [115] Copyright 2017 journal of cellular and molecular medicine.

Charge The plasma membrane of cells interacts differently with different surface charged nanoparticles (Figure 2.22). Because of attractive electrostatic interaction, the interactions between positively charged nanoparticles with the negatively charged cell membrane are significantly higher than negatively charged nanoparticles [121].

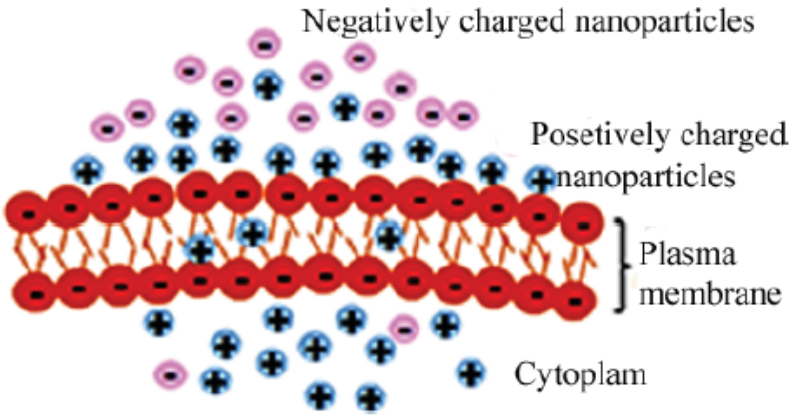

Figure 2.22: Nanoparticles` charge effect on nanoparticles-cell interaction. Reprinted with permission from ref [115] Copyright 2017 journal of cellular and molecular medicine.

Surface coating One of the powerful tool to increase the nanoparticles` uptake is the surface modification of nanoparticles especially with cell-specific targeting molecules [122]. There are variety of factors such as nature of the target cells, the constituent materials of nanoparticles, and the chemistry of conjugating ligand to apply the specific ligand on nanoparticles [115].

3 EXPERIMENTAL BACKGROUND

In this chapter the instruments are explained that are used for the experiments. It includes the instruments which are taken for characterization of the morphology and physical characterization of nanoparticles such as dynamic light scattering (DLS), transmission electron microscopy (TEM), the instruments for investigation of materials compositions like X-ray powder diffraction (XRD), fourier transform infrared spectroscopy (FTIR), instruments for the study of magnetic properties such as oscillating electromagnetic alternating field (OEMF) and vibrating sample magnetometry (VSM). Subsequently, two instruments are discussed which are used to control the viability of the cells (plate reader) and flow cytometer to investigate the nanoparticles‘ internalization to the cells.

3.1 Dynamic Light Scattering (DLS)

Dynamic light scattering (DLS) is also called Photon Correlation Spectroscopy and it is a very popular technique, which is more applicable in Chemistry and Physics laboratory and also recently in industry to be used for measuring and determining the size, size distribution, and the morphology of particles [123]. The experiment is carried out in a liquid, which particles are suspended in. What DLS measures is a Brownian motion and Doppler effect with a monochromatic laser light and the relation of it to nanoparticles‘ size. During nanoparticles‘ Brownian motion, they are illuminated with this monochromatic laser beam. Therefore, there is a small difference in the frequency between incident laser beam and scattered one after collision of beam with nanoparticles that results in Doppler shift. Due to this shift, some information emerge about size properties [123]. In a case of small particles higher Doppler shift appears while the big particles give the smaller Doppler shift. The correlation and diffusion coefficient are two parameters, emerging information about the motion and size distribution of the particles. By computing the translational diffusion coefficient, the hydrodynamic diameter of particles can be determined. The particles in a dispersion move constantly and randomly according to Brownian motions and this results in fluctuation of scattered light intensity to time. The correlation function $G(\tau)$ is determined in order to analyze scattered intensity. For

monodisperse particles the correlation function depends on the diffusion of particles:

$$G(\tau) = \int I(t)I(t+\tau)dt = \mathsf{B} + \mathsf{A}(e^{-2q})^{2D_\tau} \tag{3.1}$$

where D_τ is the translational diffusion coefficient (velocity of Brownian motion) and q is the scattering vector:

$$q = \frac{4\pi n}{\lambda_0}\sin(\frac{\theta}{2}) \tag{3.2}$$

In this equation n is the solvent refractive index, λ_0 is the vacuum wavelength of the laser, and θ presents the scattering angle. By using Stokes-Einstein equation, the hydrodynamic diameter (D_H) can be calculated according to the diffusion coefficient and amounts to:

$$D_H = \frac{\mathsf{k_B}T}{3\pi\eta D} \tag{3.3}$$

where $\mathsf{k_B}$ is the Boltzmann constant, T the temperature, and η the dispersion viscosity.

DLS components

The Dynamic light scattering instrument includes six main parts (Figure 3.1): laser, sample holder, detector, attenuator, correlator, and a computer.

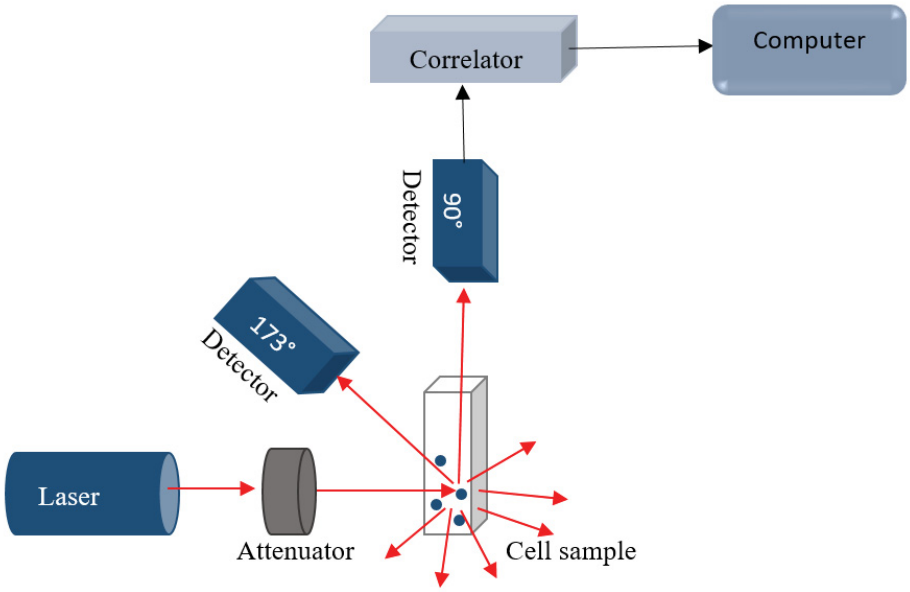

Figure 3.1: Illustration of dynamic light scattering components.

A 633 nm wavelength laser is used for sample illumination, the sample holder is placed in front of the laser beam, and the laser beam can pass through the sample. The detector

is positioned under 90° or 173° with respect to the laser beam direction and measures the scattered light. The attenuator is used to control the intensity of the laser beam scattered from the sample. The attenuator controls the intensity of the light. It means when the intensity of the scattered light is too high, the detector will be saturated. If the intensity of scattered light from the sample is not sufficient the attenuator will increase the intensity of laser radiation. The attenuator is automatically positioned in an appropriate position. Finally, the correlator is connected to a computer to analyze the data.

3.2 Transmission Electron Microscopy (TEM)

Transmission electron microscopy belongs to the electron microscopic groups and this is the most important analyzing technique for the small objects. From the historical aspect, the reason of inventing of TEM was due to the limitations in light microscopy resolution. TEM is a technique to get the higher magnification compared to the optical microscope and hence the specimen details. In the electron microscope electrons interact with the sample (specimen) and all scattered electrons will be collected to produce an image [124].
The smallest distance that our eyes can resolve between 2 point is called resolution or to be exact resolving power. According to the Rayleigh theory the resolution of the light microscope is defined as:

$$\delta = \frac{0.61\lambda}{\mu \sin \beta} \tag{3.4}$$

In this formula δ is considered as resolution (the smallest distance that can be resolved [124]), μ as refractive index of the view medium, λ is the used wavelength and β is the semi angle of magnifying lens collection. The refractive index and semi angle $\mu \sin \beta$ is called numerical aperture and is approximated to one for light microscope because $1 < \mu < 1.5$ and $\beta < 90°$ so the resolution is about half of the wavelength, for TEM it is about 0.01. According to Louis de Broglie's equation λ is related to electrons energy E. With ignoring relativistic effects we have:

$$\lambda[\text{nm}] = \frac{1.22}{\sqrt{E[\text{eV}]}} \tag{3.5}$$

Electrons have both particles and waves characteristic. According to Broglie`s idea (wave-particles dualism), through the Planck‘s constant (h = 6.626×10^{-34} N m s) the particle momentum p is related to its wavelength:

$$\lambda = \frac{h}{p} \tag{3.6}$$

when the potential drop, U, electron accelerates and obtain a kinetic energy, eU. This potential energy of electrons is equal to the kinetic energy:

$$eU = \frac{m_0 v^2}{2} \tag{3.7}$$

The momentum can easily be obtained:

$$p = m_0 v = \sqrt{2 m_0 e U} \tag{3.8}$$

By these equations the relation between electron wavelength λ and the accelerating voltage can be defined [124]:

$$\lambda = \frac{h}{\sqrt{2 m_0 e U}} \tag{3.9}$$

Equation (3.9) can be used to calculate the non-relativistic electron wavelength for operating voltages (between 100 to 1000 kV). But relativistic effect cannot be neglected at energies > $\sim$ 100 keV the reason behind is, the velocity of the electrons is higher than half the speed of light c. So the equation (3.9) must be modified to give:

$$\lambda = \frac{h}{[2 m_0 e U (1 + \frac{eU}{2 m_0 c^2})]^{\frac{1}{2}}} \tag{3.10}$$

With this equation the wavelength of high voltage electron microscopes can be obtained and be used for calculation of resolution parameter.

TEM components

The main components of TEM are electron source (electron gun), lenses, aperture, specimen and screen (Figure 3.2).

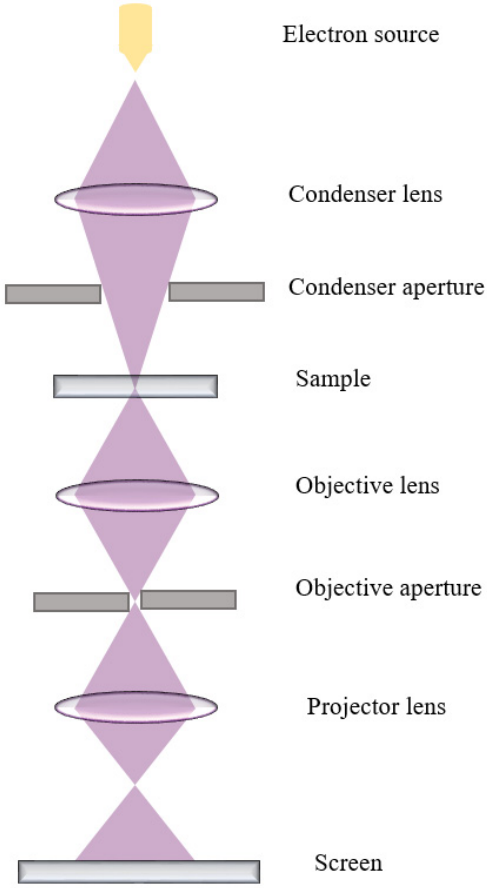

Figure 3.2: TEM components and electron beam path way.

The electron source or electron gun (the sources of high energy primary electrons) is the first component of TEM, which produces a tiny electron beam with precise controlled energy. It has a very important role in TEM to have the best images. The electron source (thermionic source) is made of a tungsten filament or lanthanum hexaboride LaB_6 and called *cathode*. If materials are heated up to a sufficiently high temperature, the electrons obtain enough energy for emission. That is how the filament produces an electron beam. In combination with the cathode, there are the Wehnelt cylinder electrode (Wehnelt Cap that covers the filament) and anode electrodes. The Wehnelt cylinder works as a first electrostatic lens and has a very small negative bias in order to have a controllable electron beam when it is passing through the anode hole and microscope. The electrons accelerate to the anode on an optic axis by

producing high value potential between cathode and anode. In the next step they pass through a Wehnelt hole. The Wehnelt hole converges beams by repelling them because of their small negative bias. All of these processes lead to very precise beams that can be formed in TEM. The electron lenses are another important component in a TEM microscope that play an important role to have the high quality images. After producing the electron beam by means of an electron gun, a condenser lens is used to form a focused, tiny and coherent beam, which determines the spot size on the specimen. As far as, all the rays from the object cannot be collected by the lenses, one aperture (condenser aperture) is used to reduce the aberration coming from scattered and reflected beams. The aperture is used to conduct effective and sharp rays to the specimen. There are three different kind of electron-sample interactions which occur when the beam from aperture hit the sample: the transmitted beam, elastically scattered electrons (called diffracted beam) and inelastically scattered electrons. In the next step, the transmitted beam passes through the objective lens, which has the crucial role in TEM. The objective lens is called the heart of TEM in combination with specimen holder. The main task of the objective lens is to focus transmitted electrons from sample to image. The objective aperture is used to increase the contrast of a picture. The last lens, which is used to enlarge the beam to the phosphor screen, is the projector lens. The phosphore screen is the last component of transmission electron microscopy to monitor the images of the samples.

3.3 X-Ray Powder Diffraction (XRD)

X-ray powder diffraction (XRD) is a fast technique applied for analytical measurements. It is used for identification of the crystalline structure of materials and atomic spacing. This technique is used for identifying elements according to their diffraction pattern when the X-ray beams are scattered from atoms in a crystal sample. Max von Laue, a German physicist in 1912, discovered that incident X-rays in an ordered array of atoms in the crystal could be scattered or diffracted in an arranged and ordered way.
That was the start of considering the crystal as three dimensional lattice with application of X-ray beams. The crystals are three dimensional unit cells, which are repeated regularly. The diffracted beam from a crystal can be intense or weak depending on how the atoms arrange in a crystal. The interaction of X-ray beam and sample shows constructive and non-constructive interferences. The constructive interference of reflected X-rays are formed when the beam scattered from sample satisfies the condition of Bragg's Law (Figure 3.3).

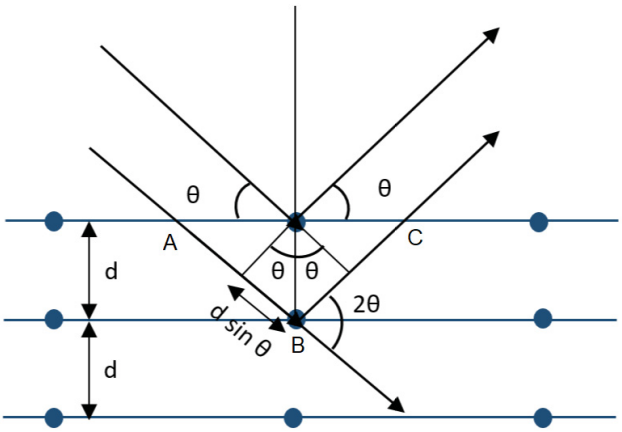

Figure 3.3: The Bragg sketch of incident beam with λ (wavelength) and scattered beam at the angle of θ from atomic plane with spacing d

.

Bragg's law is discussed when the waves with the wavelength which is comparable with the atomic spacing, are reflected from the adjacent scattered centers and results in constructive interference. The crystal solid consists of lattice planes with the equal interplanar distance d. The scattered waves remain in phase when they interfere constructively. Under this condition, two scattered waves have the path lengths difference $2d\sin\theta$ which is equal to $n\lambda$. As it is shown in Figure 3.3, two electron waves are reflected from lattice atoms and have the path length differences equal to (AB+BC). If θ is considered as an angle between incident and reflected beam with respect to plane, it can be written as:

$$AB = BC = d\sin\theta \tag{3.11}$$

$$n\lambda = 2d_{hkl}\sin\theta \tag{3.12}$$

where n is an integer, λ is the wavelength, d is the distance between planes in the lattice, which generate diffractions; hkl are also Miller index describing lattice orientation of lattice and θ is the angle of diffraction. The Bragg's law shows the relation between λ, diffraction angle and distance in lattice. Figure 3.3 shows the diffractions of X-ray beam from the atoms in the crystal lattice.

The Scherrer formula can be used to calculate the diameter D of the particles [125] from the width FWHM (full width at half maximum) of the individual reflections in the recorded diffractogram:

$$D = \frac{k \cdot \lambda \cdot \frac{180^\circ}{\pi}}{\text{FWHM} \cdot \cos(\frac{\theta}{2})} \tag{3.13}$$

The parameters in the formula are k as the Scherrer constant, λ as the wavelength of the X-ray source, FWHM as the full width at half maximum, and θ as the peak position. The broader the half-width of the reflections, the smaller the particles.

XRD components

X-ray powder diffraction includes three important parts (Figure 3.4): X-ray tube, sample holder, and X-ray detector.

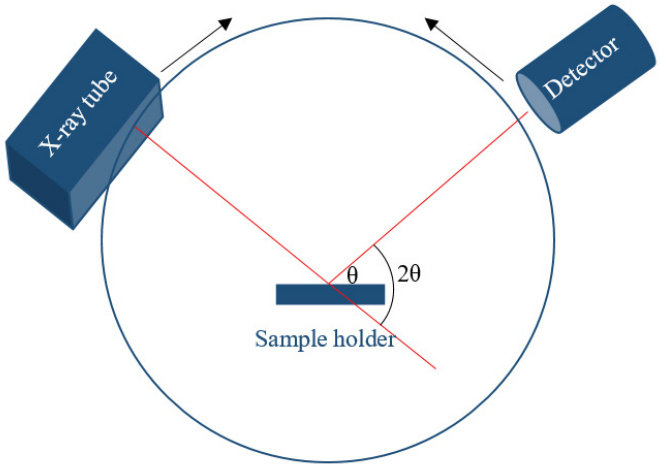

Figure 3.4: The components of X-ray diffraction systems showing X-ray tube, sample holder and the detector.

The X-ray tube itself includes the cathode filament, vacuum chamber, high voltage supply, lead shielding, filter, and anode target. The filament is negatively charged and the electrons are produced in an heated filament. The electron production rate is controlled by the filament current. If the high voltage is applied between cathode and anode in high voltage supply, an acceleration of electrons occurs towards the metal target. By bombardment of the metal target, which is normally copper, the electrons in inner shell earn sufficient energy to release from the target material. Under this condition the production of X-ray beams is possible. The X-ray tube rotates with respect to the sample holder. The second part consists of a rotatable sample holder. It is a small stage for samples and despite the fact that it rotates, it is completely stable to hold the powder samples. All collected and collimated beams strike the sample in the fine shape powder form. Finally the third part, X-ray detector, detects the diffracted beams from the sample. The detector also rotates with respect to the sample

holder during measurement as it is shown in Figure 3.4. The rotational angle between X-ray tube and detector is 2θ changing between 10 to 100 degree.

3.4 Fourier transform infrared spectrometer (FTIR)

Infrared light also called the infrared radiation is a part of electromagnetic radiation (EMR). The EMR wavelengths are longer than visible lights, therefore, cannot be seen by naked eyes. The IR spectrum range is between 10 to 13000 cm^{-1} (10^3 μm to 769 nm) and to better clarification can be divided to 3 regions; near infrared with the wavenumber of 13000 to 4000 cm^{-1} (769 to 2500 nm), middle infrared with the wavenumber of 4000 to 200 cm^{-1} (2.5 to 50 μm), which is mostly used to study vibrational and rotational structure of chemical composition and finally far infrared with the wavenumber of 200 to 10 cm^{-1} (50 μm to $10^3\mu$m). The fourier transform infrared (FTIR) spectrometer is a laboratory measurement instrument, based on IR technique. Infrared spectroscopy is one of the feasible techniques in chemical measurements, which is used for identifying and investigating the components and composition of material by means of absorption spectroscopy. The samples are in the form of solid or liquid. Infrared spectroscopy is the study and analysis of infrared light interaction with molecules. The IR graph is illustrated by the transmittance (absorbance) as a function of frequency and wave number given by the cm^{-1}.

IR spectrometers are categorized into two different classes which are dispersive and Fourier Transform instruments. As it has been explained dispersive infrared spectroscopy (IR) and fourier transform infrared spectroscopy (FTIR) are both related to electromagnetic spectrum region with a long wavelength and low frequency in comparison to visible light. The difference of IR and FTIR is that the monochromatic IR light is used in IR spectroscopy but the multi-chromatic light is used to take the absorption spectrum of the chemical compound which is more effective in compare with IR spectrum. FTIR is also employing interferometer which takes a number of scans. There are also some advantages of using FTIR than IR. For example FTIR is faster than IR and gives the better resolution because the higher number of scans per minute is taken in FTIR compared to IR.

Atoms in molecules are not fixed. They vibrate or rotate in different modes with different frequencies, this vibration or rotation is correlated with structural characteristics of a molecule. When the infrared light emerges, some of the radiations are passing through the sample and some are absorbed in the sample, which is due to a change of the rotational and the vibrational energy. The resulting spectrum is normally from 4000 to 400 cm^{-1} showing the unique spectrum of each molecule and it is called the chemical finger print of the material. When the frequency of IR light is the same as the frequency of the molecule vibrations, the

light is absorbed by the molecules and changes the molecular vibration amplitude.

IR and FTIR components

An FTIR instrument was used for this project but to distinguish the difference between IR and FTIR the components of both instruments are explained. As explained IR spectrometers are categorized into dispersive IR and FTIR. Dispersive IR instruments consist of IR light, two slits, diffraction grating, sample, and detector as shown in Figure 3.5. The fixed IR source is directed to the diffraction grating after passing through the first slit and splits the light to several single beams (monochromatic beams). By rotating the diffraction grating each single beam can separately pass through the second slit. These beams are then directed to the sample and each wave length will be individually examined. When the beam passes through the sample part of it will be reflected, absorbed or transmitted. The transmitted part that carries the molecular information of the sample is detected by the detector and displayed as a spectrum.

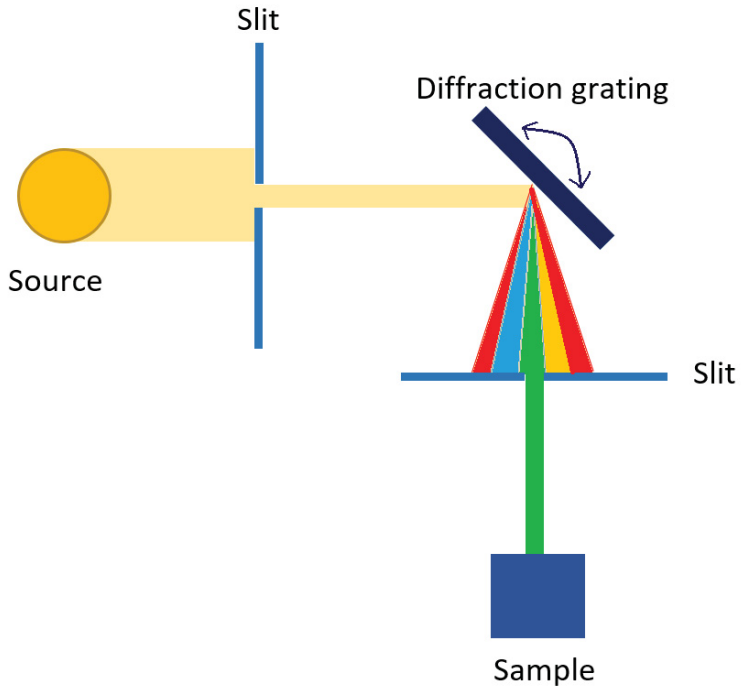

Figure 3.5: The components of dispersive IR spectroscopy

As it can be seen in the Figure 3.6 (the schematic of used FTIR instrument) fourier transform infrared instrument consists of four important parts: the light source, the interferometer, the sample and the detector. Interferometer also includes beam splitter, movable and fixed mirror.

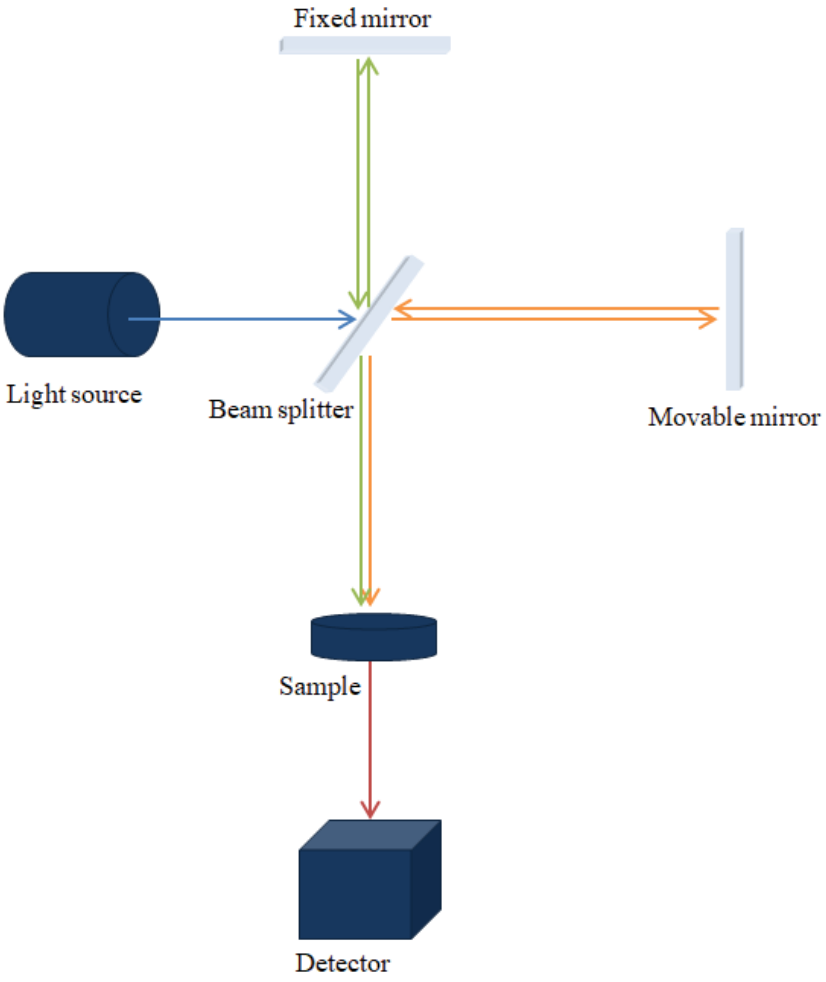

Figure 3.6: The components of the fourier transform infrared (FTIR) spectroscopy

The appropriate light is generated according to the interest of the measurements and passes through the interferometer. In the interferometer (called Michelson interferometer) by striking the light to the beam splitter, it will find two path ways perpendicular to each other. The one way goes to the fixed mirror and one goes to the movable mirror and again reflecting to beam splitter again. By moving the mirror, the interferometer will block and transmit each wavelength of light repeatedly and periodically because of wave interference. In the beam splitter they combine together again and go to the light reference and the sample. The sample holder which is called cuvettes window is made of alkali halide mono-crystals such as NaCl, KBr or CsI, which has no interference in the measurement specially KBr that shows no absorption under 400 cm^{-1}. The detector observes the waves in reference and also the wave passed through the sample and compare them together. The raw data is called interferogram. Fourier transform algorithm is used to turn raw data (the light which is absorbed for each mirror position) into desired spectrum (light absorption for each wavelength).

3.5 Oscillating electromagnetic alternating field (OEMF)

The excitation of magnetic particles with an alternating electromagnetic field causes the transformation of the electromagnetic energy into heat. This effect is described by the hysteresis loss, relaxation processes and the delay in the alignment of the magnetic moments of the particles along the external applied field. For single-domain particles, there are two relaxation mechanisms, which are responsible for heat loss. These are the Néelian relaxation, the release of the energy being described by the rotation of the magnetic moments, and the Brownian relaxation, the release of the energy being described by the rotation of the particles [103].
The Brownian relaxation is more dominant than the Néelian relaxation in the ferrofluids and it is the main reason for the heat generation. In the case of reorientation according to the Brownian relaxation mechanism, the viscosity of the surrounding medium, η, the hydrodynamic radius, r_h, do play an important role in determining the relaxation time τ_B [103].

$$\tau_B = \frac{4\pi\eta r_h^3}{k_B T} \tag{3.14}$$

Another important factor which is measured by alternative magnetic field is Specific Heat Power (SHP). SHP describes the amount of energy converted to heat per time and mass and allows an evaluation of the heatability of different particles.

OEMF components

The setup and the components of OEMF are shown in Figure 3.7: high-frequency generator, water-cooled induction coil, optical temperature sensor, isolated glass for sample.

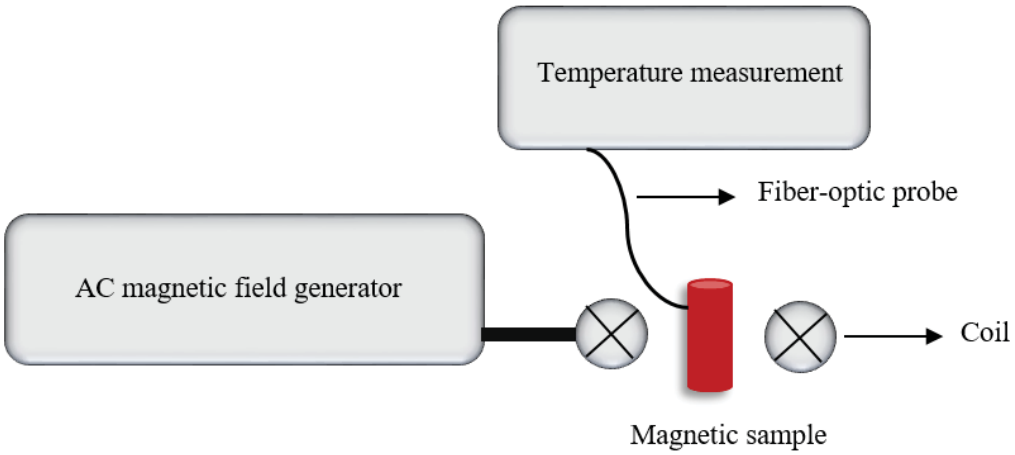

Figure 3.7: Illustration of Alternative magnetic compartment, copper coils, and a temperature measurement system. Figure is based on [103]

The OEMF is generated by a high-frequency generator, which is connected to a water-cooled copper induction coil. The temperature rise of the samples is detected as a function of time by a temperature sensor. The sample is placed in an isolated double glass, which is used for thermal insulation. The results of all the investigated systems are graphically represented with respect to their heating rate (A) and their saturation temperature (ST), and finally the specific heating power SHP values of the various systems.

3.6 Vibrating Sample Magnetometry (VSM)

Vibrating Sample Magnetometry (VSM) measurements are carried out in order to determine the magnetic properties of the materials quantitatively and qualitatively. The magnetization of a sample is measured as a function of the applied field as the sample is vibrating perpendicular to a uniform magnetic field [126, 127]. The shape of the magnetization curve is influenced by the size and shape as well as the composition [128, 129].
VSM is working based on Faraday's Law of induction. Changing the magnetic field produces an electric field, which provides information about the change of magnetic field. The sample is placed in a constant magnetic field which magnetizes the sample. Therefore, magnetic domains are aligned in this field. By applying the strong magnetic field, more magnetic dipoles will be aligned in the direction of applied magnetic field and reach the saturation point. The magnetic field, which is called magnetic stray field is produced by magnetic dipole moment. The magnetic stray field is changing when the sample moves up and down, therefore, will be sensed by pick-up coils. According to the Faraday's Law of Induction an electric field is produced by means of an alternating magnetic field. The output of VSM is monitored in a computer in a hysteresis curve format, which is showing the relation between induced magnetic

flux density and magnetizing force [130].

VSM components [130]

Figure 3.8 shows the components of VSM instrument. The components consist of: water cooled electromagnet and power supply, vibration exciter and sample holder, sensor coils, amplifier, control chassis, lock in amplifier, measuring tape, computer interface.

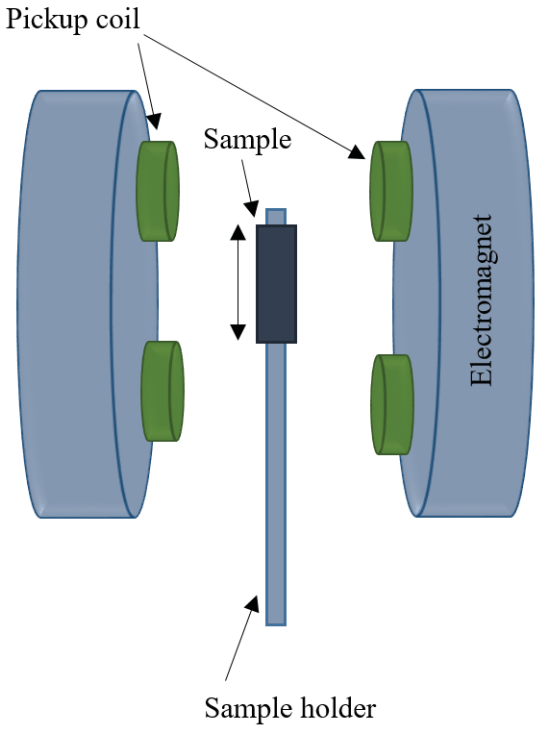

Figure 3.8: Schematic of vibrating sample magnetometer illustrating sample holder, pickup coils and electromagnet.

The constant magnetic field, which is used to magnetize the sample is generated by a water cooled electromagnet, along with the power supply. The sample holder has a rod shape and is connected to the vibration exciter, and at the end is mounted between pole pieces. The sample is moved by the exciter up and down at the set frequency. The desired orientation is obtained by rotation of the sample rod in the constant magnetic field. By movement of the sample an alternating current is produced in sensor coils at the same frequency of vibrating sample. The information of these signals is concerned about the magnetization of the sample. The sensor coils create the signal and the amplifier just amplifies this signal.
Control chassis controls the oscillation of exciter, which is normally around 85 Hz. The amplifier is used in order to pick up the signals at the vibrating frequency. The amplifier diminished

the noises from environment. This measuring tape is used to measure the important parameters, which are necessary. All data are collected by the software, which is controlling automatically all the components during data collection.

3.7 Plate reader

The instrument Elisa reader plates, which is called microplate readers or microplate photometers are designed to be used to detect biological, chemical and physical events of samples. 96-well microplate is the most common microplate, which is used in research laboratories [131]. In this project it is used for MTT assay in order to control the viability of cells. There are single and multi-mode microplate readers, which can use fluorescence, luminescence, absorbance and other light based detection techniques. Most of the detection instruments have the same component just different in light pass through the sample.

Plate reader components

Figure 3.9 shows the components of a plate reader instrument. The components consist of: light source system, excitation double monochromator, top/bottom optics, emission double monochromator, detector.

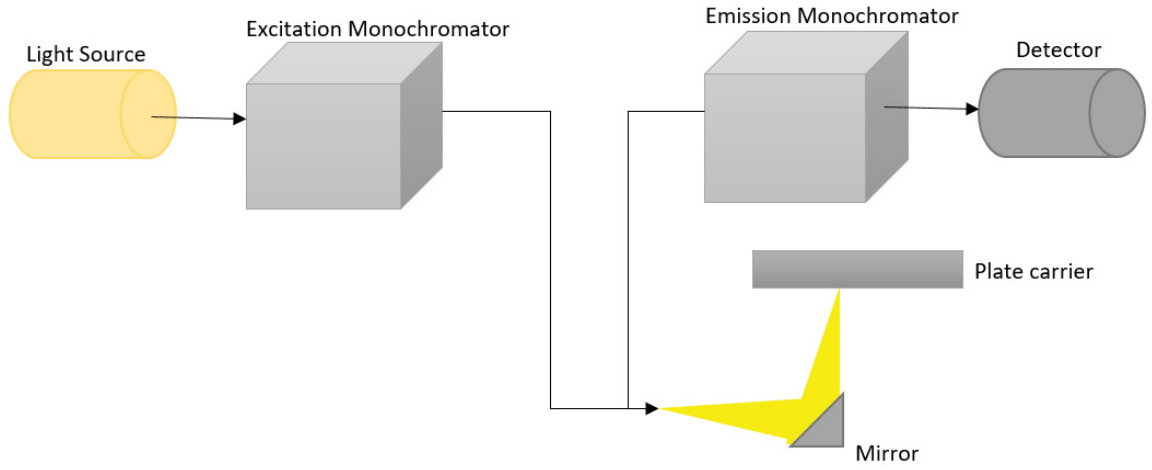

Figure 3.9: Optical System Fluorescence Bottom.

The lamp light source utilizes a high energy Xenon arc discharge lamp. The inside of lamp bulb is filled of high pressure Xenon atmosphere. When the flash lamp is sparking through a small gap between two electrode the flash decays in few microseconds with the flash frequency of 40 Hz. The flash lamp is used for fluorescence and absorbance measurement.

Any wavelength can be selected from a defined optical spectrum by means of a monochromator, which is an optical instrument. It is operating like a tunable optical filter and adjusts wavelength and bandwidth. The monochromator consists of an entrance slit and an exit slit. The Flash light is passing through the optical system by focusing onto the entrance slit of the excitation monochromator by means of a condenser. A monochromator selects the excitation light. Excitation light is coupled into the fiber bundle when it has passed the monochromator. Subsequently the light goes to the top or bottom measuring head and is focused into the sample by using the top or bottom lenses. The Excitation Double Monochromator works similar to the Emission Double Monochromator in order to select any fluorescence signal wavelength. An adjustable filter is used to discriminate scatter of excitation light and nonspecific fluorescence. The selected wavelength is between 300-660 nm with the bandwidth of 20 nm. To detect very low light intensity of fluorescence a photo-multiplier tube (PMT) is used.

3.8 Flow Cytometry

Flow cytometry is an automated method, which has a high throughput with very fast analysis of multiple chemical and physical characteristic of single cells within cell population. The special form of flow cytometry is called fluorescence-activated cell sorting (FACS). This method is using in order to sort a heterogeneous mixture of cells into two or more containers. These containers are based upon the fluorescence and/or light scatter properties of one single cell [132].

A sample consists of cells or particles, which are suspended in fluid and then injected to the flow cytometer. The cells or particles ideally flow in a single cell at a time through a laser beam. The light scattered from the laser beam characterizes cells and their components. Cells can also be stained by fluorescence marker and be detected by different detectors. The flow cytometer enables the measurement of thousands of cells rapidly. The flow cytometer has many applications in basic research, clinical practice, and clinical trials. Flow cytometry uses include: cell counting, cell sorting, determining cell characteristics and function, detecting microorganisms, biomarker detection, protein engineering detection, diagnosis of health disorders such as blood cancers.

Two most important parameters that a flow cytometer instrument measures are forward scatter (FSC) and side scatter (SSC). Overall size of cells are given by FSC while the SSC provides information about intracellular structure of cells and organelles [133]. Forward scatter is also affected by absorbing and reflecting of materials for example the cell nucleus, other organelles, cell shape, and also the particles in the cells can change the refractive index (RI), which changes FSC intensity.

Flow Cytometry components

The main parts of flow cytometry setup, shown in Figure 3.10, are: the flow cell, measuring system, detector, amplification system, and a computer for analysis of the signals.

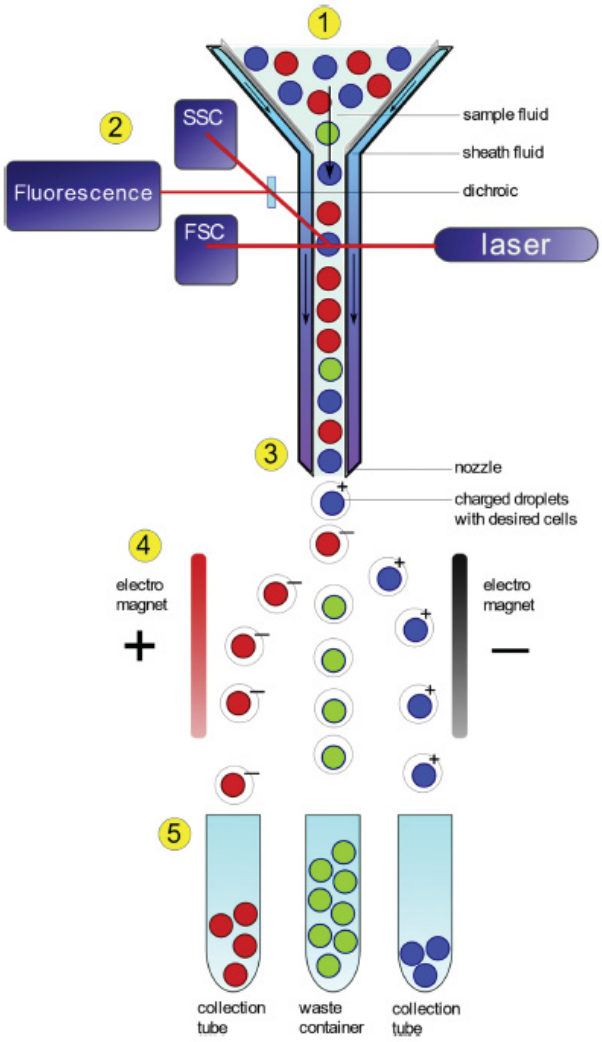

Figure 3.10: Schematic illustrates the component of flow cytometer device. Reprinted with permission from [132]

Flow part is a part of flow cytometer instrument, which is containing a liquid stream. Cells are suspended in the liquid stream and are aligned in single file and let only one single cell pass through sample cup surrounding by the fluid, which is moving downwards. There is a difference between flow speed of the fluid and the sample fluid and it results in alignment of stream of individual cells [132].

In the second step, cells are passing through a laser beam and by different detectors multiparametric measurements are carried out. There is an interaction between laser light and

each cell (called event). The laser light can be scattered, absorbed or emitted as fluorescent light. The diffracted light are FSC and SSC, which was explained before.
The events of individual cells, which are passing through the laser beam can be plotted in a computer connected to the instrument. A pulse of scattered or emitted light can be produced on a detector by passing the cell through a laser.
In the next step, the stream of cells can be positively or negatively charged when they are passing through a charging ring. If they cannot be charged they remain neutral. After passing a charging ring the stream enters the nozzle and by means of an acoustic wave produced by piezoelectric element, the stream is divided into individual droplets. There are two electromagnetic deflection plates, one positively and one negatively charged. Therefore, after passing through the plate the positive/negative droplets are collected or reflected to the tubes.

4 EXPERIMENTAL SETUP

In this chapter, the set up for each experimental technique and also the sample preparation which is used for the determination of the structural and magnetic properties will be discussed.

4.1 Reagents and material

Ferric chloride ($FeCl_3 \cdot 6H_2O$, 99%, CAS NO. 10025-77-1) was purchased from ROTH and ferrous sulphate ($FeSO_4 \cdot 7H_2O$, 99,5% - CAS NO. 7782-63-0) from ACROS (USA). Ammonium hydroxide (NH_4OH, 25%, CAS NO. 1336-21-6) was obtained from VWR. 3-aminopropyltriethoxysilane ($NH_2(CH_2)_3Si(OC_2H_5)_3$, APTES) was purchased from SIGMA ALDRICH, Germany. The PC3 prostate cancer cell line was from Professor Schulz group (Research Institute of Urology) and the BPH1 benign cell line from Professor Ahmadian group (Institute of Biochemistry and Molecular Biology, Heinrich Heine Universität, Düsseldorf). Formvar / carbon film on 200 mesh Cu nets (S162) were from Plano GmbH.

4.2 Nanoparticles experiments

In this part the synthesis and coating procedure of magnetite nanoparticles is described in detail.

4.2.1 Synthesis of magnetite nanoparticles (MNP)

Magnetite nanoparticles were synthesized by the methods from Molday [33], via the standard co-precipitation method, magnetic nanoparticles precipitated by adding alkali solution to Fe(II) and Fe(III) solution (molar ratio $2:1$). Briefly, $FeCl_3 \cdot 6H_2O$ (2.704 g, 0.0196 mol) and $FeSO_4 \cdot 7H_2O$ (1.3704g, 0.0095 mol) was dissolved in 180 ml distilled water while N_2 gas is flowing through a three-necked flask under vigorous mechanical stirring.
The experimental set up for synthesis and coating of the nanoparticles is shown in Figure 4.1 and contains stirrer, three necked flask, bubble counter, heater, bath oil, and plastic pipe for flowing nitrogen.

Figure 4.1: Experimental set up to synthesize magnetite nanoparticles wet chemically , consist of: three necked flask, reflux, heater, oil bath, nitrogen inlet and outlet, bobble counter, and stirrer.

After sufficiently stirring of the iron salt, 5.5 ml of ammonium hydroxide (NH_4OH) was injected abruptly in one portion to the reaction mixture by 10 ml syringe while continuing stirring with the same speed for additional half an hour. After injection of the base the pH of the solution was measured by a pH meter until it reached about 10. For stirring of the solution magnetic stirring was also used sometimes, whereas mechanically stirring shows better results in comparison.

Due to addition of the alkaline solution the color of the mixture changed from orange to brown and finally black (Figure 4.2), which shows the formation of MNPs precipitation immediately.

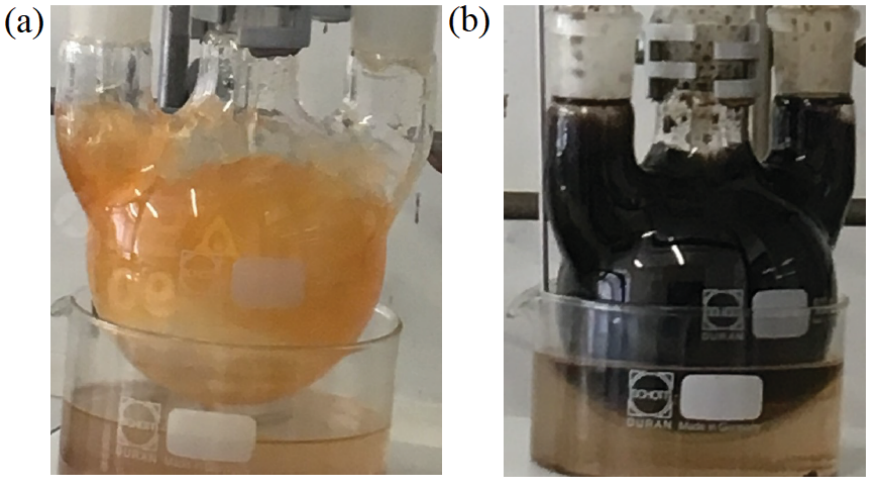

Figure 4.2: Illustration of three necked flask schematic before and after co-precipitation:
(a) iron salts are diluted in deionized water for thirty minute and figure (b) is related to co-precipitation of iron oxide after adding ammonium hydroxide, showing the black color.

In order to decrease the pH from 9.5 to 7 and to remove the residual ions the black solution was washed by magnetic separation with distilled water and ethanol. At the end, the magnetite nanoparticles were dispersed in ethanol for the subsequent coating procedure.

4.2.2 Coating procedure

In some literature it is mentioned that the sample is dried in order to be prepared for coating (e.g., [33]). In this project magnetite nanoparticles are prepared in liquid in order to protect particles from aggregation (Figure 4.3).

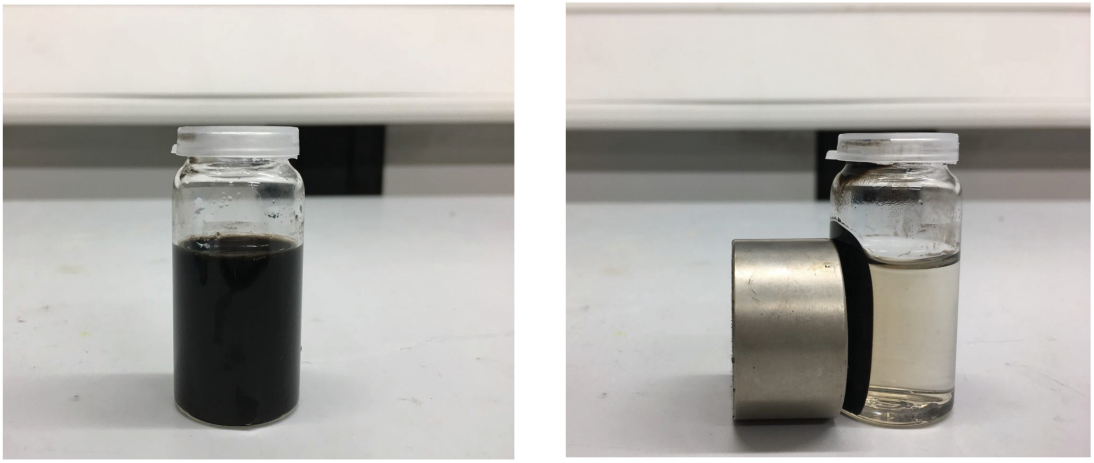

Figure 4.3: Magnetite nanoparticles behavior after applying the magnet.

The agglomeration of nanoparticles increases due to the drying procedure. In order to do that after washing the particles with water, the particles are washed with ethanol for two or three

times. 70 mg of obtained magnetite nanoparticles diluted in ethanol was added to more of ethanol (totally 150 ml) and 1 ml of water and sonicated for 5 min [61]. After sonication, 35 μl of 3-aminopropyltri ethoxysilane $(NH_2(CH_2)_3Si(OC_2H_5)_3$, APTES$)$ was added to the reaction environment while mechanically stirring (1000 rpm) for 7 hours. The aminosilane coated particles were obtained after washing 5 times with ethanol and are now ready to be prepared in two different forms, in a liquid and as a solid, for variety of measurements. Figure 4.3 shows the effect of a magnet on synthesized APTES-MNP. After few seconds, the particles are completely shifted towards the magnet.

4.3 Cell experiments

In this section, there are information about cell lines which are used in this project, in particular the cell culture, cell treatment with nanoparticles, fixation of the cells and preparation the cells for controlling the viability of cells by MTT assay.

4.3.1 Cell lines

All experiments with cells are carried out with two cell lines: PC3 and BPH1. PC3 are prostatic epithelial cells and obtained from a human prostate cancer cell line. It is used in cancer research and for development of drugs. PC3 cells are also assessing the cells response to chemotherapeutic agents. The cells are cultured in RPMI-1640 and monitored by EVOS XL core cell imaging system (Figure 4.4). Optical microscopy makes it easy to quickly analyze the status of the cells.

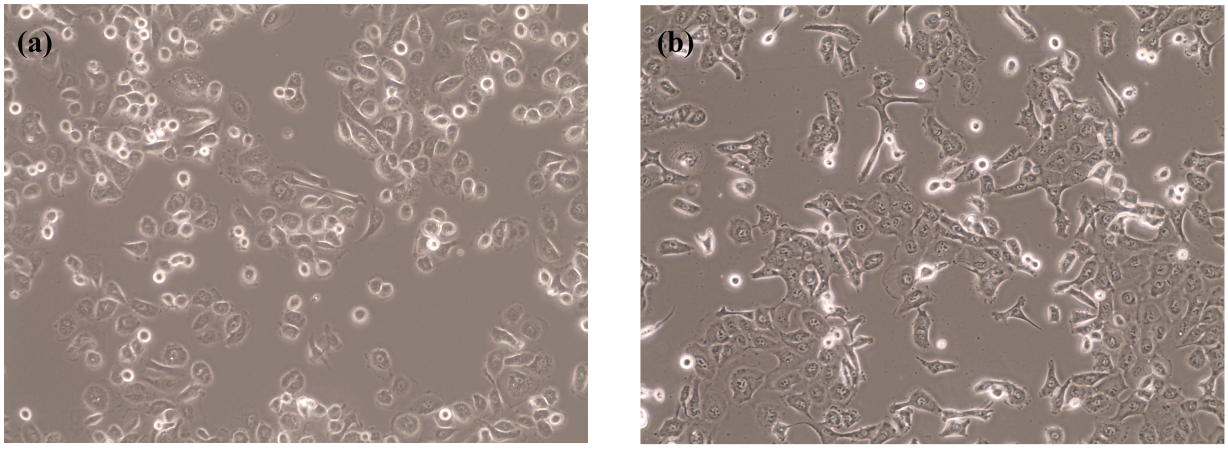

Figure 4.4: Cell images of a) PC3 and b) BPH1 taken with 20 $\times$ magnification by EVOS microscope

BPH1 cells are from the benign hyperplastic prostatic epithelial cell line and they are not from

a prostate cancer cell line (such as LNCaP, DU-145, and PC3) [134] and considered as normal cells.

4.3.2 Cell culture

Primary definition of cell culture refers to the application and removal of the cells from animal or plant and growing them in artificial condition like the animal body [135]. In this project two different cell lines are used, which are considered as a cancer cell line and non-cancer cell line. Cell line is the first subculture of the animal cell sample. They are epithelial cells, which are polygonal in shape. These cell lines are in biosafety level 1 (BSL-1), which is the basic level of protection. Each cell type has its own culture condition. It normally consists of a medium that supplies the necessary nutrients (amino acids, carbohydrates, vitamins, minerals), growth factors, hormones, and gases (O_2, CO_2), and regulates the physicochemical environment (pH, osmotic pressure, temperature). Cells are cultured in the 75 ml plastic flask. PC3 and BPH1 were cultured in RPIM 1640 medium (ThermoFisher, 11875093) supplemented with 10% fetal bovine serum (FBS) (ThermoFisher, 10270-106) and 5% penicillin-streptomycin (Genaxxon bioscience, M3140.0100). To do that first of all cells are washed with autoclaved PBS slightly in order to not remove the cells from the substrate. Subsequently, the cells are trypsinated for 5 min to detach the cells from the substrate and then centrifuged while they are diluting in medium. Depending to the size of flask we dilute the cells by 12 ml of medium for 75 ml flask or 5ml of medium for 25 ml flask. Cells need two or three days to grow and cover the substrate of the flask when they are placed in an incubator.

4.3.3 Fixation and cell embedding for TEM

For embedding the cells, they were fixed with 2,5% glutaraldehyde, 4% paraformaldehyde in 0,1 mol/l cacodylate buffer solution for at least 2 hours. Subsequently, the cells were washed and fixed with cacodylate buffer and osmium tetroxide (2%) respectively, dehydrated with 70-100% acetone and embedded in spur and cut in a tiny film using an ultra-microtome.
We separate the cells from the flask substrate by trypsin after washing with PBS, then cells are centrifuged and prepared as the pellet in small falcon. The first step of fixation starts with cover the small cell pallet with 1.5 ml of fixative for least for 2 h. After that samples are washed 4×10 min with 0.1 mol/l cacodylatpuffer. For continuing the fixation and contrasting the sample, 1 ml per sample of 1% (bzw. 2%) osmiumtetroxid in cacodylat buffer covers the samples. After 2 hours, samples are washed 3×10 min with deionized water (optional: 0, 1 mol/l cacodylat buffer). The drying of the sample starts with 1×20 min 30% Aceton, 1×20 min 50% Aceton and 1×20 min 70% Aceton and continuing with 1 hour resting of cell in 70$\%$ Acetone with 1$\%$ PWS (Phosphotungstic acid) + 0, 5$\%$ UA (Uranylacetat). Uranylacetat is a

radioactive chemical and has to be used with gloves.
In the second day, the pellet of the cells is covered with 90% Acetone and 100% Acetone for 2×30 min for each while they are turning on the rotator. In order to separate the acetone and to bring the cells in the plastic form we remove the acetone and adding spurr slightly. Therefore the pellet is covered with acetone and molecular sieve and spurr with the ratio 2+1 (2ml per sample) for one hour, acetone molecular sieve and spurr with the ratio 1+2 (2ml per sample) for one more hour, 2 hour pure spurr and another spurr overnight.

For the third day, the cells are stayed in freshly prepared spurr for four hours and the last part of embedding to form plastic sample is to apply pure spurr for 8 hours in 70 ℃. The embedded cells are cut with ultramicrotomes (Leica EM UC6) presented in Figure 4.5 in a very thin sectioning (10 nm thickness) and prepared for microscopy with TEM.

Figure 4.5: Illustration of the ultramicrotomes (Leica EM UC6) for cutting plastic form of cells embedded for TEM.

4.3.4 MTT assay

3-(4,5-Dimethyl-2-thiazolyl)-2,5-diphenyl tetrazolium bromide (MTT assay) was used to evaluate the cell viability after treatment by nanoparticles according to Mosmann [21]. 5 mg/ml of tetrazolium salt were dissolved in PBS and filtered to sterilize. To prepare the sample, PC3 and BPH1 cells were cultured with confluency of 70-80% after nearly 24 hours and were treated with 100 and 500 μg/ml of MNP and APTES-MNP in 96 well plate in an incubator (Figure 4.6).

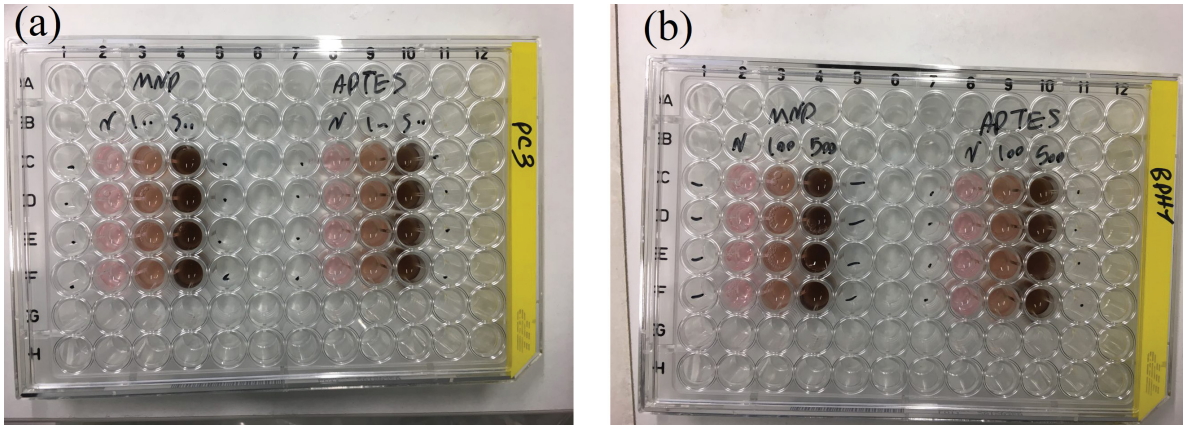

Figure 4.6: Treatment of (a) PC3 and (b) BPH1 cell line in 96 well with 0, 100, and 500 μg/ml of MNP and APTES-MNP to check the viability with MTT assay

One sample is also considered without any treatment as a control sample. The samples are removed after 24 hours, the cells were washed three times with PBS to remove the rest of particles suspended, that were not taken by the cells. MTT assay was added and incubated with 10% (20 μl per 200μl medium) concentration for 4 hours to form formazan crystal and then 150 μl DMSO was added per well to dissolve the formazan crystal (Figure 4.7). The quantity of formazan are proportional to the viable cells.

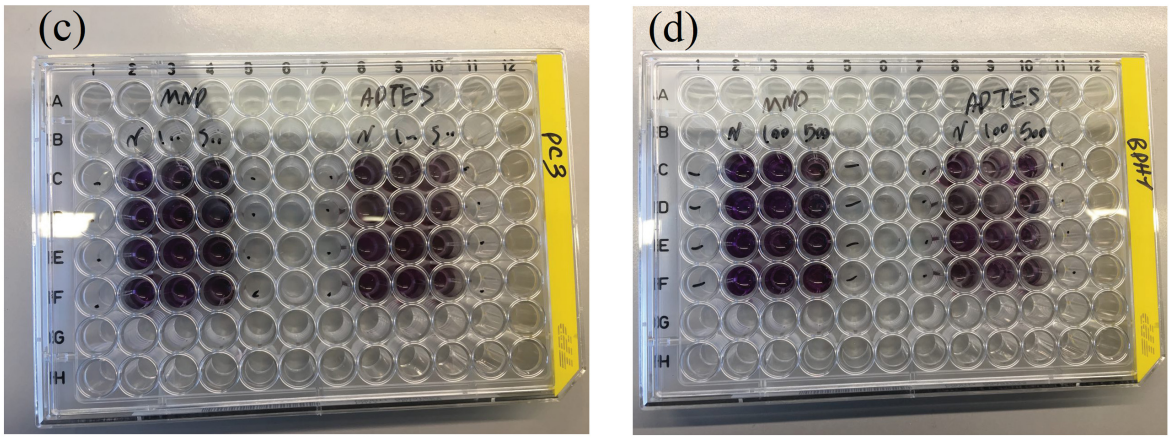

Figure 4.7: Changing the color of (c) PC3 and (d) BPH1 cell line in 96 well treated with 0, 100, and 500 μg/ml of MNP and APTES-MNP to purple because of forming formazan crystal due to application of tetrazolium salt (MTT assay).

4.3.5 Sample preparation for flow cytometry measurement

PC3 and BPH1 cells were treated with 100 and 500 μg/ml of APTES-MNP for 24 hours. For flow cytometric analysis, single-cell suspensions were obtained with trypsin and the cells were washed with ice-cold PBS. The cells were fixed in 4% paraformaldehyde (PFA; Merck) for 10 $\sim$ min on ice, followed by two times washing with PBS.

4.4 Magnetotactic bacteria

This section introduces the procedure of cultivation of magnetospirillum gryphiswaldense, enrichment and extraction of magnetosome from magnetospirillum magnetotacticum, MS-1, and magnetospirillum gryphiswaldense, MSR-1, which are carried out in the form of part of this PhD project, one master, and three bachelor projects.

4.4.1 Cultivation of Anaerobian/Microaerophilic Bacteria

In order to cultivate Anaerobian/Microaerophilic bacteria, it is important to be aware of the concentration of oxygen because these bacteria –as it can be understood from their name– are anaerobian bacteria. They do not need oxygen for their cultivation or at least a few percentages of oxygen is needed. Exposure of the atmosphere to them can inhibit their growth. Therefore, they have to be prepared in an oxygen-free medium. In order to do that cultivation is carried out in a home made glove box (Figure 4.8) being an environment under controllable oxygen amount by means of an optical oxygen sensor and also with Hungate technique.

Figure 4.8: Home made glove box for cultivation of bacteria.

Preparation of nutrition medium The medium is prepared according to the description of DSMZ company, medium 380 and medium 141. According to this procedure all the chemicals are weighted precisely and mixed in order to obtain the ideal medium. The medium is transferred to Hungate tube and then autoclaved for 15 min at 121 ℃. The sterilized and deoxygenated medium is inoculated and incubated for approximately between 48 or 72 hours.

The entire procedure is carried out in a glove box environment especially after autoclaving of the medium.

4.4.2 Extraction of bacteria

In order to be able of using the magnetosomes, extraction of bacteria is carried out. This process consists of enrichment of bacteria, washing and extraction with lysozyme and EDTA.

Enrichment The bacteria are cultivated in Hungate tubes and are dispersed in the medium. Therefore it is necessary to enrich them to achieve the higher concentration of bacteria. Magnetotactic bacteria (MTB) have the natural tendency of migrating toward oxic-anoxic transition zone (OATZ). To do that by forming the oxygen gradient in the tubes, a vertical stratification is realized by opening the butyl cap under sterile condition and let the air flow into the tube. After 5 to 7 days a milky layer near the surface appears (Figure 4.9), which can be removed with the pipette in order to start the washing process and then extraction.

Figure 4.9: The red box illustrates the milky layer of enriched MS-1 bacteria after 7 days exposure to the air. Reprinted from bachelor thesis supervised by me [136].

Washing procedure In order to remove the nutrition medium from enriched bacteria, some processes are carried out. First of all, the rest of the medium is removed by centrifuging of

the sample and resuspended in the obtained pellet with 1000 μl of PBS and pumped with a pipette. This procedure will be repeated two or three times.

Extraction of bacteria with Lysozyme and EDTA In order to extract the magnetosomes, the MTB have to be destroyed and the cell membrane must be damaged. By application of Lysozyme and EDTA, the cell membrane can be damaged and the magnetosomes can be extracted. First 50 mg of Lysozyme and 50 mg of EDTA are mixed in 1 ml water separately. Then 5 μl of each sample are added to the bacteria for 30 seconds every five minutes. This process takes 45 min. The samples are centrifuged for 15 min with a centrifugal acceleration of 10.000 g and at a temperature of 4 °C. After centrifuging, the obtained pellet is resuspended with 500 μl of PBS, pumped with the pipette and centrifuged again for 10 min. At the end the pellet is resuspended in 250 μl PBS and ready for measurement.

4.5 Characterization instruments

As described above, the sample can be prepared in a solid and liquid with respect to the measurement. For example liquid samples are necessary for dynamic light scattering (DLS), preparation for transmission electron microscopy and oscillating electromagnetic alternating field (OEMF). X-ray diffraction and infrared spectroscopy are some examples of measurement techniques that are using samples in solid form, VSM measurements are carried out with both.

4.5.1 Dynamic light scattering (DLS)

The DLS instrument from Malvern Nano S Zetasizer (Figure 4.10) is used in this project.

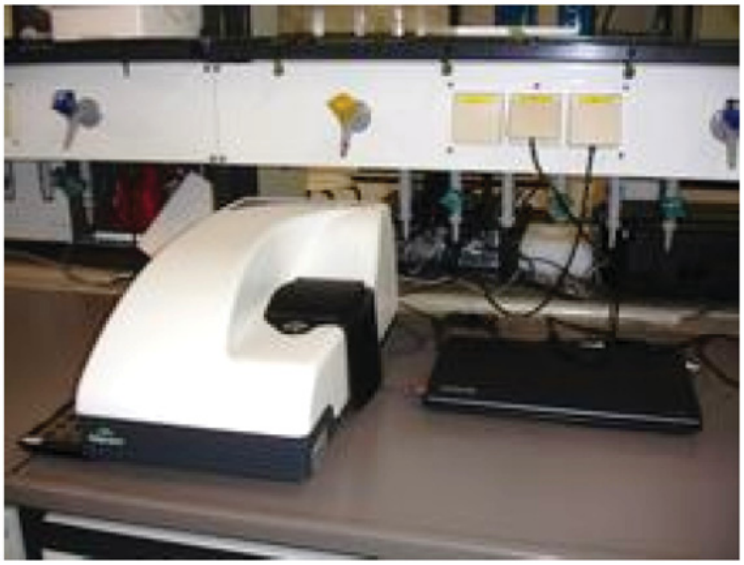

Figure 4.10: Malvern Nano S Zetasizer

The angle between laser and detector is fixed at 137°. The He-Ne (helium-neon) laser beam provides light with a wave length of 633 nm. To prepare the sample for DLS, a cuvette is used and can be filled to maximum 1 ml and additionally 1 to 2 drop of sample can be added depending on the concentration. The cuvette contains 1 ml of sample and is placed in front of the laser beam.

4.5.2 Transmission electron microscopy (TEM)

The transmission electron microscope 902 from Zeiss (Figure 4.11) was used for imaging of nanoparticles with the resolution of 1 to 2 nm and also another TEM H600 form Hitachi was used to investigate the internalization of the particles to the cells.

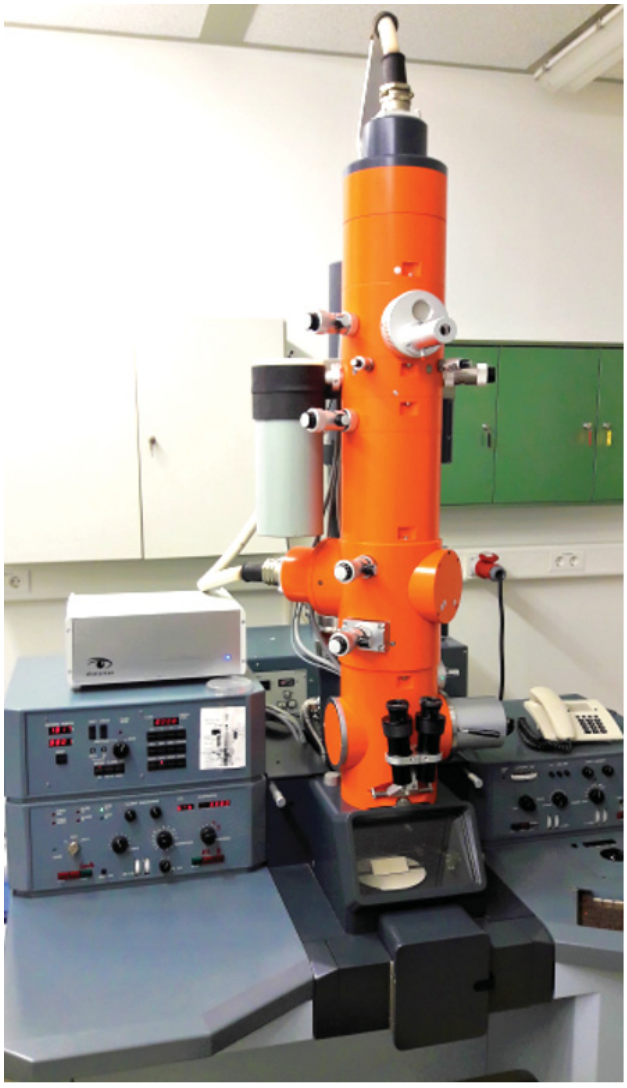

Figure 4.11: Transmission electron microscope 902 from Zeiss

In order to use TEM one drop of diluted sample in water can be placed on the top of Formvar / carbon film on 200 mesh Cu nets from PLANO GmbH and dried for approximately one hour. By drying the liquid sample placed in a small glass and heating in the oil bath over the heater in approximately 80 ℃ magnetite can be dried and is ready.

4.5.3 X-ray diffraction (XRD)

The BRUKER D2 Phaser (Figure 4.12) is used in this measurement. The Cu tube is used as an X-ray source with the wavelength of 0.154 nm. In this set up the rotational angle is set between 10° and 80° because it is expected to see the diffraction peaks of nanoparticles in this range. Additionally the lower boundary is affected by the instrument. The samples are prepared in the form of powder in order to be used for XRD measurement.

Figure 4.12: Bruker D2 Phaser.

4.5.4 Fourier transform infrared spectroscopy (FTIR)

The IR spectroscopy is measured by a Bruker Tensor 37 (Figure 4.13) in the MIR range, Mid Infrared (4000 - 400 cm^{-1}).

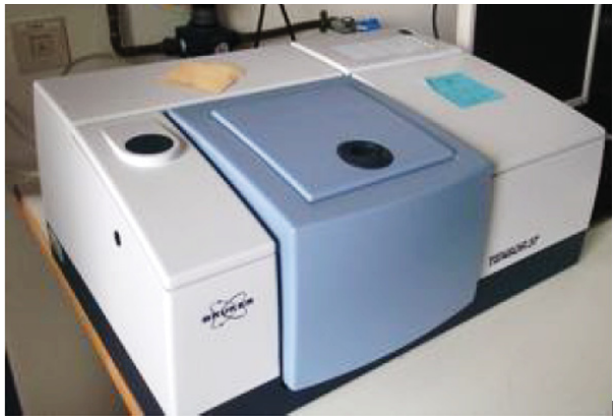

Figure 4.13: Bruker Tensor 37

The sample can be prepared as a solid or liquid. But the solvent should not be water or ethanol otherwise the spectrum exhibits a huge peak. Therefore, we used the solid form and tried to dry the sample perfectly to skip this peak.

4.5.5 Vibrating sample magnetometry (VSM)

The magnetization curves are monitored at room temperature with an ADE Magnetics Vibrating Sample Magnetometer EV7 up to maximum field strength of 1600 kA·m^{-1}. A typical experiment consists of a virgin curve, followed by a full hysteresis loop. All samples are measured in a sealed Teflon vessel, placed on a glass sample holder between two poles of an electromagnet and vibrated at a frequency of 75 Hz. The raw data is corrected by subtraction of the signal of the paramagnetic material. Saturation magnetization (M_s), remanence magnetization (M_r), coercive field (H_c) and initial susceptibility (χ_{ini}) are determined.

4.5.6 Oscillating electromagnetic alternating field (OEMF)

The measurements are carried out with a high-frequency generator AXIO T5 from Hüttinger (Figure 4.14).

Figure 4.14: Oscillating electromagnetic alternating field (OEMF) or AC magnetic field: The image is taken from Physical - Chemistry Institute, University of Cologne where the measurements were carried out

The copper induction coil consists of five windings. An optical temperature sensor OTGA-62 from Opsens was used for temperature measurements. The measurements are performed at a frequency of 247 kHz and a field strength H of 31.5 kA·m^{-1}. The temperature rise of the samples is detected as a function of time by a temperature sensor. The sample is measured in an isolated double glass (Figure 4.15), which is used for thermal insulation. The results

of all the investigated systems are graphically represented with respect to their heating rate dT/dt and their saturation temperature T_S, and finally the specific heating power SHP values of the various systems.

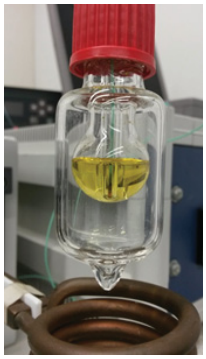

Figure 4.15: Two ml isolated glass container for liquid sample in order to be used for OEMF measurement.

4.5.7 Plate reader

In this project the infinite 200 PRO multi-mode plate reader family (Figure 4.16) from TECAN company has been used, which is a user friendly and easy to use instrument.

Figure 4.16: Eliza reader, infinite M200 PRO.

ELIZA reader is used to record the absorbance changes at 570 nm. The wavelength can be adjust according to the sample and measurement. To do the measurement the nanoparticles treated cells are placed in the device in suitable frequency and by running the device after few seconds the result are shown in an Excel format file. The results are later analyzed by Origin software.

4.5.8 Flow cytometry

The samples were analyzed with FACS Canto II (BD Pharmingen) (Figure 4.17). 200 μl of sample is placed in a special glass for the measurement. The measurement for each sample takes few seconds. The flow cytometer is connected to the computer which illustrates the result of measurement and helps to adjust the measurement area. Therefore, according to this result we can control the appropriate gate of the measurement that cells can be shown. Evaluation of data was carried out with “Flowing software” (version: 2. 5. 1) (Turku Center for Biotechnology, University of Turku, Finland).

Figure 4.17: Flow cytometer, BD FACSCanto II.

5 RESULTS AND DISCUSSION

In the first section (section 5.1), the co-precipitation method is presented to synthesize the magnetite nanoparticles and then stabilizing (coating) of the particles in order to increase the viability and biocompatibility of them. Subsequently, the measurements are carried out to characterize the physical, morphological and magnetic properties of nanoparticles. In the second section (5.2), the uptake and biocompatibility of nanoparticles are explained. Finally, in the section (5.3), the result of cultivation, enrichment and extraction of two types of bacteria are presented and discussed.

5.1 Magnetite nanoparticles

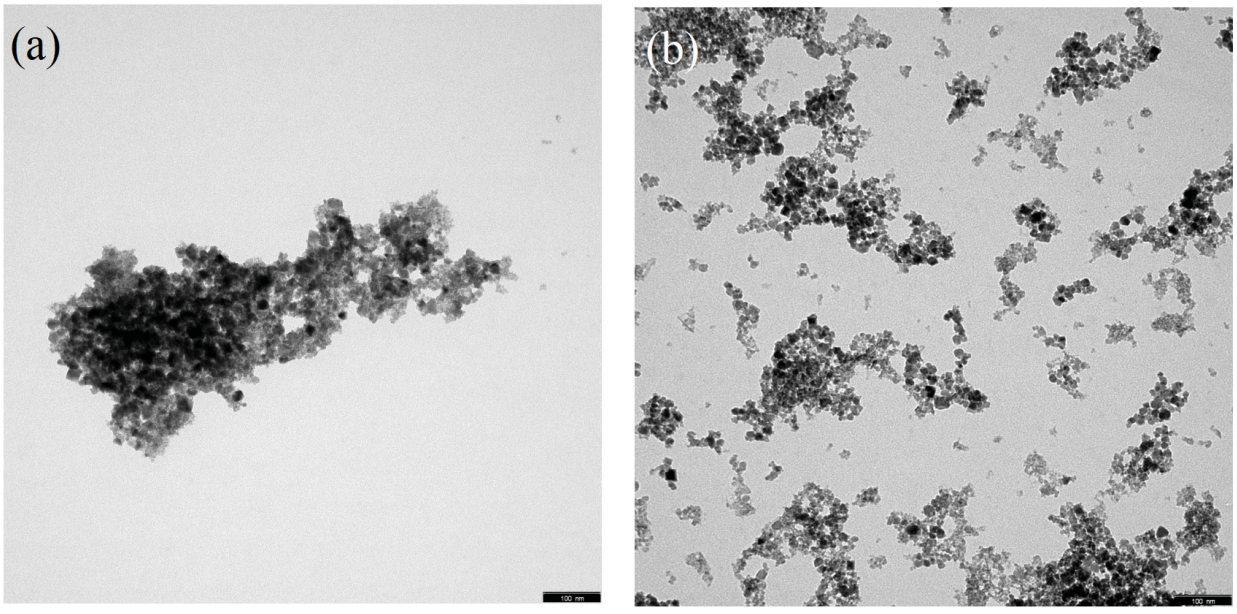

Figure 5.1: (a) TEM images for magnetite nanoparticles with 100 nm scale bar. (b) TEM images for aminosilane (APTES) coated magnetite nanoparticles with 100 nm scale bar.

The magnetite nanoparticles are synthesized by co-precipitation and evaluated using TEM. The naked nanoparticles aggregate and tend to grow, therefore, the aggregations are observed for uncoated MNP (Figure 5.1. a). Coating the nanoparticles results in decreasing the size of aggregations and appearance of more single particles (Figure 5.1. b)

5.1.1 Morphological characterization of MNPs by TEM

Figure 5.2 shows the TEM image of quasi-spherical magnetite nanoparticles coated with APTES. The average diameter of the metallic core is about (10.41 $\pm$ 1.92) nm, which can be seen from the evaluation of the size distribution of the particle diameter according to TEM measurements (Figure 5.2 b).

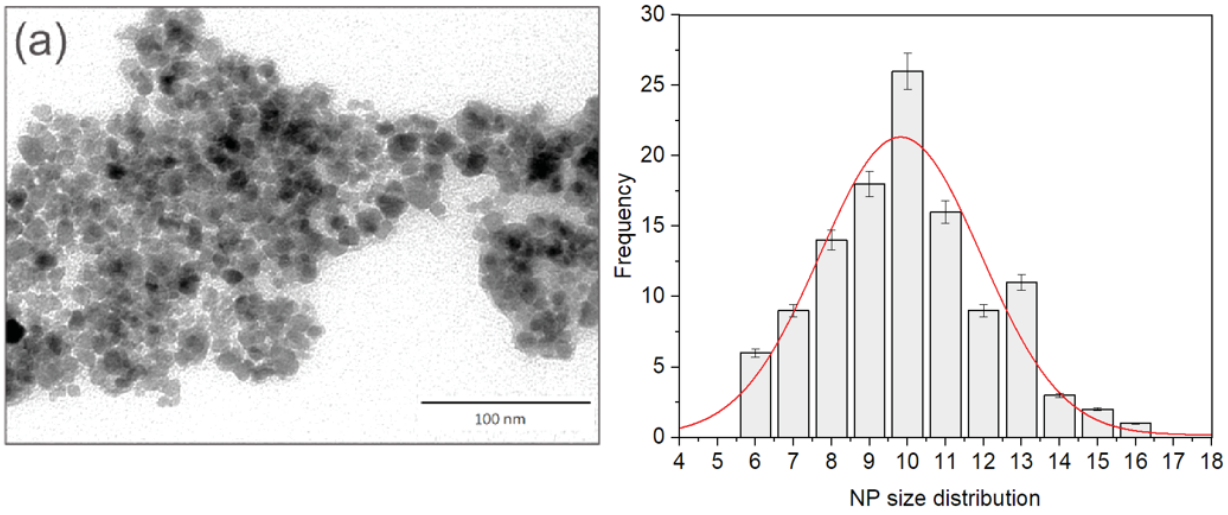

Figure 5.2: (a) TEM images [137] for aminosilane coated magnetite nanoparticles (APTES-MNP). (b) Related size distribution histogram of coated magnetite nanoparticles.

5.1.2 Measurement of MNPs size using DLS

The hydrodynamic size of nanoparticles was measured by DLS. The DLS data of MNP (Figure a) and APTES-MNP (Figure b) are presented in Figure 5.3.

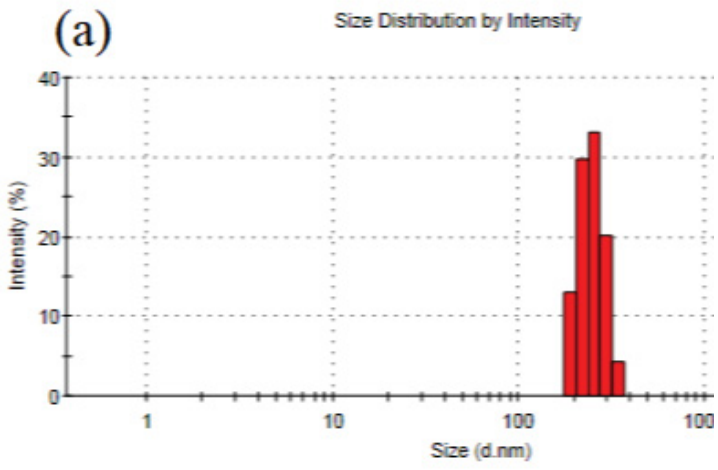

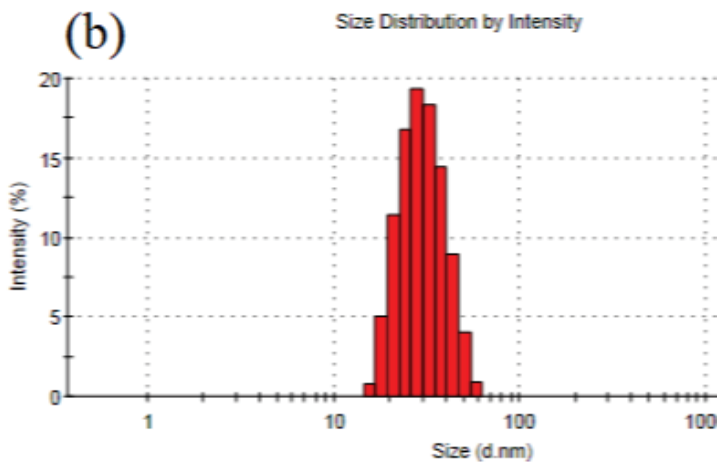

Figure 5.3: DLS histogram [137] of (a) MNP and (b) APTES-MNP. A smaller hydrodynamic size of coated particles is observed due to the stability of particles after coating.

It is obvious that the size of the particles is larger in comparison to TEM, because the hydrodynamic size of nanoparticles with their ligand are measured in DLS but the TEM shows just the metallic core of nanoparticles. Another reason is the presence of nanoparticles agglomeration in the water during the DLS measurement which is shown in [138]. The DLS illustrated larger particles for MNP than APTES-MNP. The reason is by coating the particles and increasing the stability we observe smaller agglomeration for APTES-MNP [137].

5.1.3 Measurement of nanoparticles crystalline structure using XRD

To determine the crystalline structure of the magnetite nanoparticles with and without functionalization, XRD measurements have been carried out. The XRD pattern confirm the cubic inverse structure of both MNP and APTES-MNP with their characteristic peaks (2 2 0), (3 1 1), (4 0 0), (4 2 2), (5 1 1) and (4 4 0) being shown in XRD pattern (Figure 5.4), which is in a good agreement with literature (Table 5.1) [139]. The XRD results prove that magnetite nanoparticles coated with APTES do not change the crystalline structure.

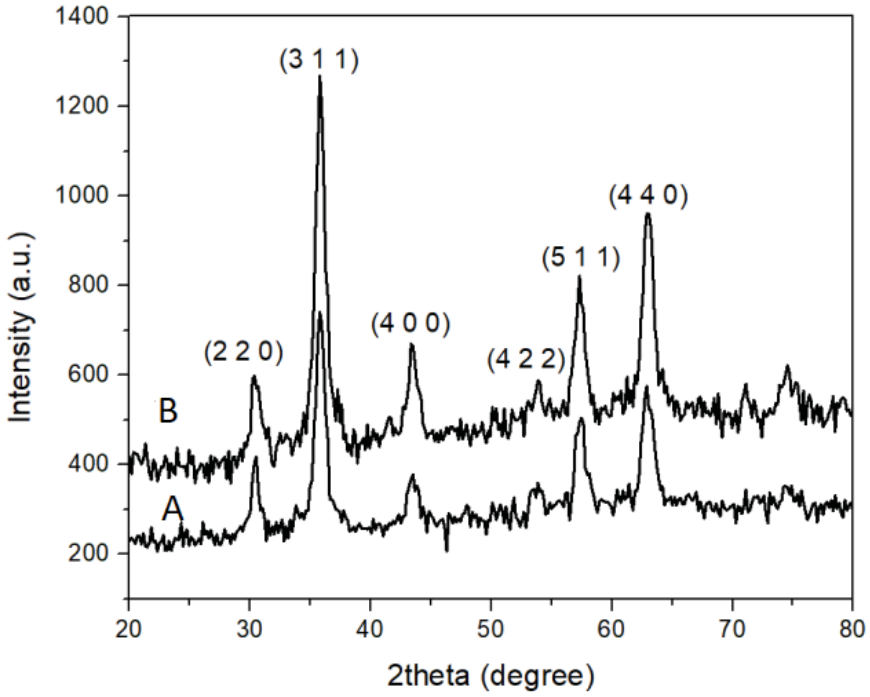

Figure 5.4: XRD of (A) uncoated and (B) coated magnetite nanoparticles.

Measured	Magnetite			Maghemit		
$2\theta_{Meas}$	(hkl)	d_{hkl} [nm]	$2\theta_{Lit}$	(hkl)	d_{hkl} [nm]	$2\theta_{Lit}$
30,3° ± 0,4°	(220)	0,2967	30,1°	(220)	0,295	30,3°
35,7° ± 0,4°	(311)	0,2532	35,4°	(311)	0,2514	35,7°
43,3° ± 0,4°	(400)	0,2099	43,0°	(400)	0,2086	43,3°
57,3° ± 0,4°	(511)	0,1616	56,9°	(511)	0,1604	57,4°
62,9° ± 0,4°	(440)	0,1485	62,5°	(440)	0,1474	63,0°

Table 5.1: Comparison of interference angle of obtained distance between adjacent plane in the magnetite powder sample with magnetite and maghemite with literature.

As it has been obtained from measurement magnetite nanoparticles and the particles coated with aminosilane have the same crystalline structure showing the structure of iron oxide

nanoparticles from literature [139]. As it can be understood from the table, magnetite and maghemite have the same value from the XRD measurement, but as far as they have different color and procedure in order to be prepared, we can be sure that our sample is presenting the magnetite nanoparticles. The XRD data determine not only the crystal structure of nanoparticles but also the size of nanoparticles can be calculated by using the Scherrer equation 3.13. For a perfect spherical shape of the particles, a form factor of $k = 0.89$ would be assumed, while for unknown particle shape the value is typically estimated to be $k \approx 0.9$ [140]. By considering the particles as an approximately spherical or slightly elliptical form, $k \approx 0.9$ is a suitable form factor.

The size calculated using the Scherrer´ formula describes the mean diameter of the particles (Table 5.2). To calculate the diameter of nanoparticles, we need to determine the peak position and FWHM from Gauss-curve and Voigt-profile. The half-value width results from individual fits to the five most distinct reflections in the diffractogram (Figure 5.5). In addition to the five Gaussian curves, five Voigt profiles are each matched to the data [140]. The average diameter of nanoparticles calculated by Scherre formula for Gauss-curve and Voigt-profile are (9,09±1,56) nm and (9,32±1.61) nm respectively.

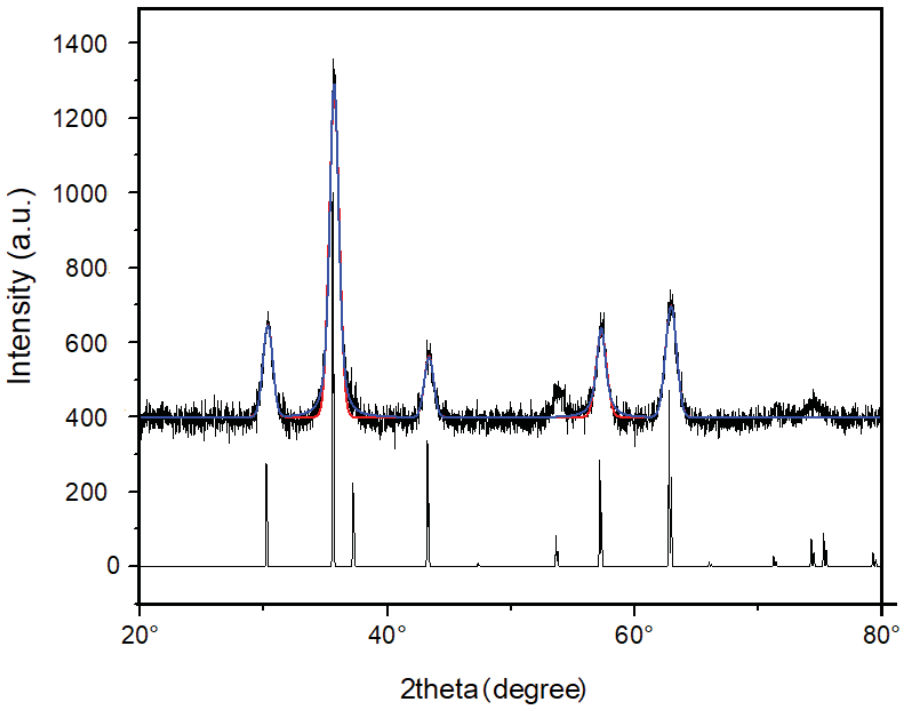

Figure 5.5: XRD of magnetite nanoparticles with Voigt profile (blue line) and Gauss fit (red line).

$2\theta_{\text{Meas}}$	Scherrer-formula (Gauss-Curve) D [nm]	Scherrer-formula (Voigt-Profile) D [nm]
30,3° ± 0,4°	8,86 ± 0,96	8,47 ± 0,92
35,7° ± 0,4°	9,09 ± 1,17	9,75 ± 1,26
43,3° ± 0,4°	9,70 ± 1,54	9,55 ± 1,52
57,3° ± 0,4°	8,98 ± 1,96	10,32 ± 2,26
62,9° ± 0,4°	8,81 ± 2,16	8,53 ± 2,09
Average	9,09 ± 1,56	9,32 ± 1,61

Table 5.2: Calculated by the Scherrer formula (equation 3.13), mean diameter of the nanoparticles of the magnetite nanoparticles; the half-widths result from the fit by Gauss curves or Voigt profiles [141]

5.1.4 Chemical component analysis of MNPs using FTIR

The stable coating with the APTES molecules is due to the large surface-to-volume ratio of the nanoparticles, the high surface activity, and the OH-rich surface [142]. This is shown in Figure 5.6 by comparing the FTIR spectra of magnetite nanoparticles without coating (A) and with coating (B).

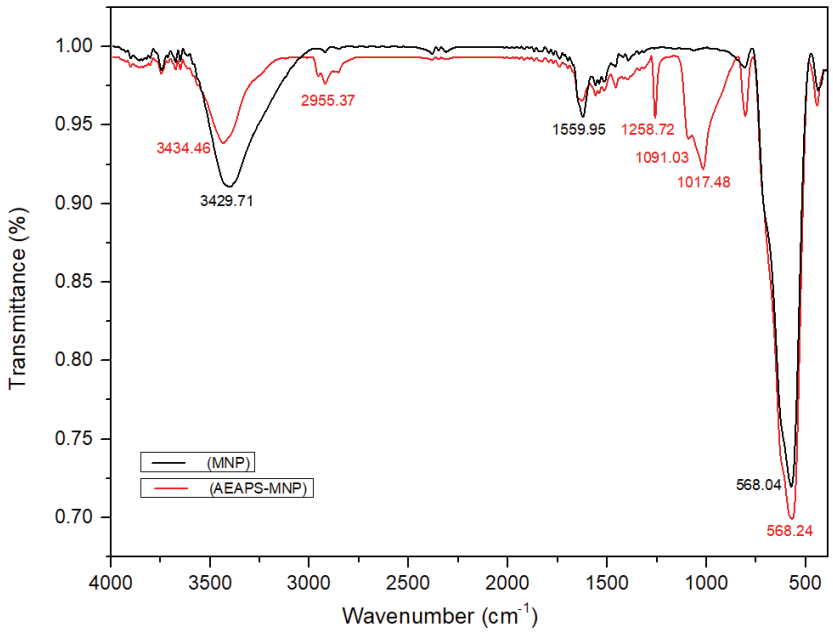

Figure 5.6: FTIR spectra of uncoated (black line) and coated magnetite nanoparticles (red line).

Fe-O bonds in bulk magnetite has $\nu 1$ and $\nu 2$ band at 570 cm^{-1} and 375 cm^{-1} , respectively [138]. The FTIR spectra in (Figure 5.6) show two absorption bands at around 568 cm^{-1} and

621 cm^{-1}, which results from splitting of the $\nu 1$ band. This split is a characteristic absorption band of Fe-O band and it is related to the split of the energy levels of quantized nanoparticles. The band at 441 cm^{-1} comes from a shift of the $\nu 2$ band.
Decreasing the size of materials from bulk to nanoparticles results the break a large number of bonds for the surface atom. Therefore, the localized electrons rearrange on the surface of particles. So when the size of Fe_3O_4 reduces to the nanoscale dimension causes increase of surface bond force constant. That is resulted on shifting the absorption bands of IR spectra to higher wavenumber.
In comparison to the coated magnetite nanoparticles, FTIR spectra of APTES–MNP show additional absorption bands at 2855 cm^{-1} and 2920 cm^{-1} due to stretching vibrations of C-H bonds. The bands at 1017 cm^{-1} and 1091 cm^{-1} is the result of stretching vibrations of Si-O. The band at 804 cm^{-1} is due to -NH_2 vibration, which only occur for aminosilane coated magnetite nanoparticles.

5.1.5 Effect of changing synthesis parameter on nanoparticles´ size

As described in chapter 2, different parameters like salts, temperature and stirring speed play an important role in the nanoparticles´ synthesis and have effect in the size and structure. Some of these parameters are controlled with different experimental techniques such as TEM and XRD and presented in more detail in a bachelor project [141]. Table 5.3 shows the parameters that have been changed through the measurement:

	Iron salts	Stirring speed	Temperature	Coating	Analyse-methods
1	$FeSO_4$ + $FeCl_3$	800 rpm	20 °C	-	TEM, XRD
2	**$FeCl_2$ + $FeCl_3$**	800 rpm	20 °C	-	TEM, XRD
3	$FeSO_4$ + $FeCl_3$	**400 rpm**	20 °C	-	TEM
4	$FeSO_4$ + $FeCl_3$	800 rpm	**75 °C**	-	TEM
5	$FeSO_4$ + $FeCl_3$	800 rpm	20 °C	**APTES**	TEM
6	$FeSO_4$ + $FeCl_3$	800 rpm	20 °C	**TMAOH**	TEM

Table 5.3: Overview of all discussed measurement. Reprinted from [141] under my supervision.

From table 5.4, it can be seen that temperature plays an important role in NP size changes due to increasing the ionic strength and also the number of nucleation due to increase of temperature up to 50 ℃.

Samples	diameter [nm]
reference sample: $FeSO_4$ + $FeCl_3$, 800 rpm, 25 °C	10,41 $\pm$ 1.92
samples with different salts (**$FeCl_2$ + $FeCl_3$**)	9,36 $\pm$ 2,72
sample with different stirring speed (400 rpm)	10,19 $\pm$ 2,41
sample with different temperatur (75 °C)	7,55 $\pm$ 1,95

Table 5.4: Effect of different salts, stirring speed and temperature on nanoparticles size. Reprinted from [141] under my supervision.

Another important factor that has an effect on nanoparticles´ agglomeration size is the amount of solution (here water). By increasing the amount of water, we observed less agglomeration of NP due to the decrease of particle interactions (Figure 5.7).

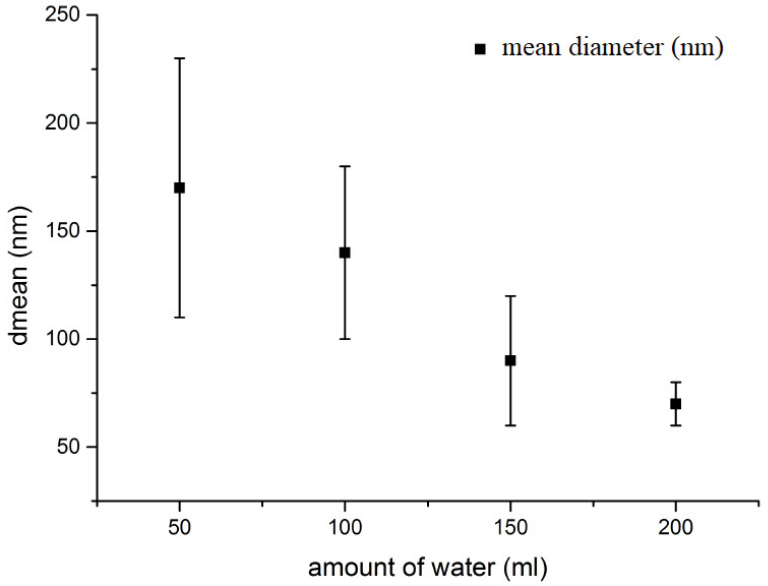

Figure 5.7: $d_{mean} \pm \sigma$ of obtained particles for different amounts of water used in synthesis. Reprinted from [143] under my supervision.

If the amount of water increases for synthesis of the NP the collision of particles are decreased due to the more distance between particles and smaller agglomerations of particles are seen.

5.1.6 Magnetic characterization of MNPs using VSM

The vibrating sample magnetometer (VSM) measurements are carried out in order to determine the magnetic properties of the magnetite nanoparticles quantitatively and qualitatively. Figure 5.8 shows the magnetization curves of particles in the dry state. All curves exhibit a

shape being characteristic for magnetic nanomaterials. The saturation magnetization (M_S) of the powders is between 55.3 $A \cdot m^2 \cdot kg^{-1}$ and 60.4 $A \cdot m^2 \cdot kg^{-1}$. Compared with the saturation magnetization of bulk Fe_3O_4 from literature 92 $A \cdot m^2 \cdot kg^{-1}$ [144] it can be seen that the measured values for the saturation magnetization M_S of all particles (Table 5.5) are smaller than the literature value. This might be due to organic rest on the particle, the crystallinity of the particle or the aminosilane coating on the particles. The closed hysteresis loop of nanoparticles (Figure 5.8) suggests that the particles show purely superparamagnetic behavior. The high values of the initial susceptibility are also due to the superparamagnetic behavior of the particles.

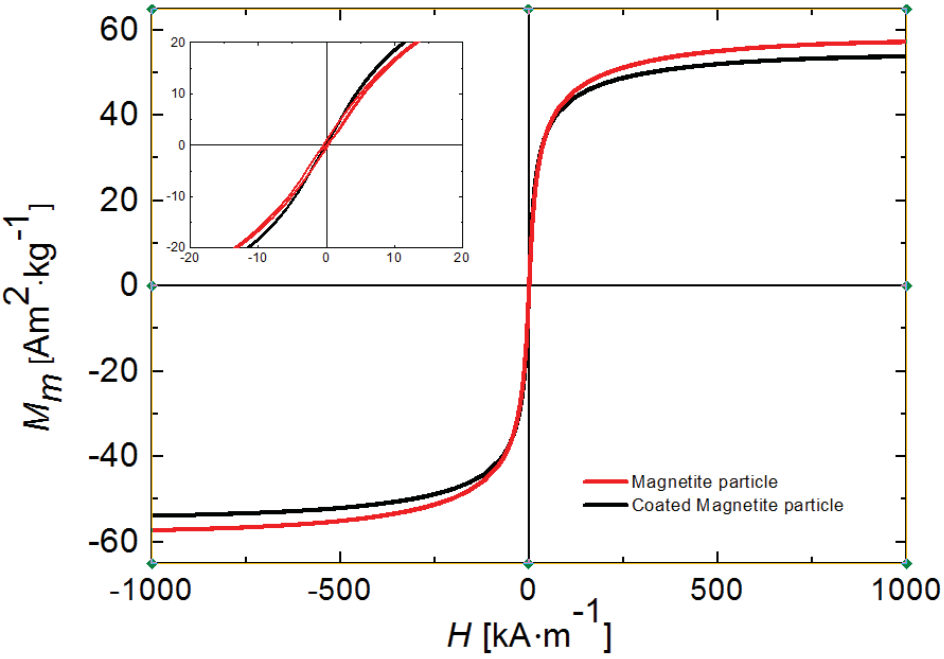

Figure 5.8: Vibrating sample magnetometry (VSM) measurement for magnetite nanoparticles (red line) and for coated magnetite nanoparticles (black line)

	samples	M_S [A.m^2]	χ_{ini} $\times 10^{-4}$ [m^3.kg^{-1}]	H_c [kA.m^{-1}]	M_R/M_S	$\mu_{Mag}[m.\%]$
1	Fe_3O_4	59.1±2.9	9.58±0.14	0.36±0.18	0.02±0.01	64.0±1.6
2	APTES-Fe_3O_4	55.3±2.8	11.5±0.9	0	0	59.9±5.7

Table 5.5: Magnetic properties of the magnetite and the coated magnetite in solid form.

The magnetic properties of the ferrofluids are also determined by VSM measurements. These measurements mainly serve to determine the magnetic component, which is necessary for the

calculation of SHP (Specific Heat Power) in the next chapter. Four samples have been measured with various concentrations of coated Fe_3O_4. Figure 5.9 shows the hysteresis curves of the measured ferrofluids. The results of all the ferrofluids measured are listed in Table 5.6. The samples show as expected similar magnetic properties to each other ($H_b, M_R/M_S$). The magnetic concentration of the samples increases form sample 1 to sample 4. The concentration of samples prepared in lab have good agreement with the measured concentration with VSM (Table 5.6).

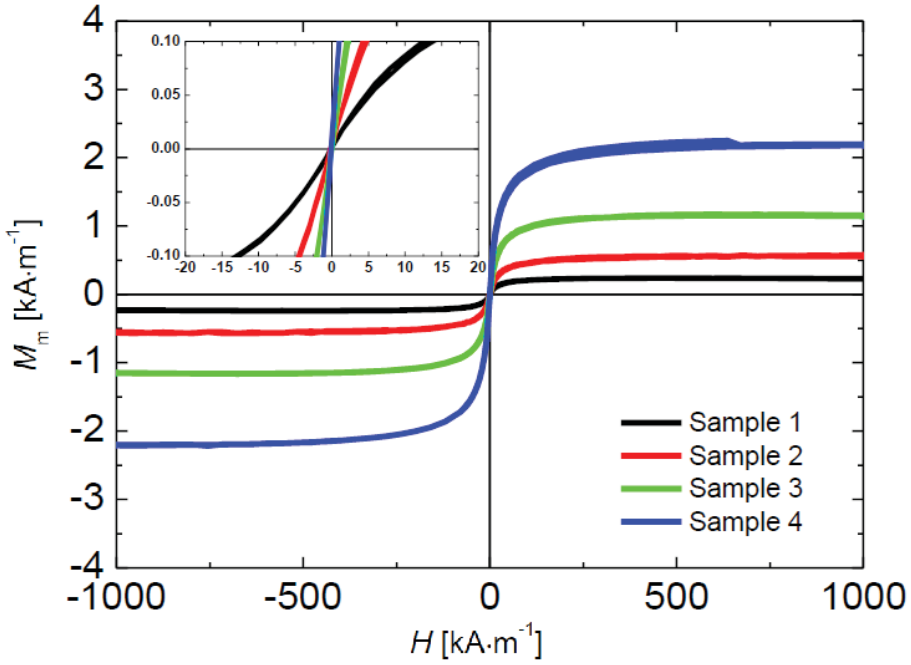

Figure 5.9: Magnetization curves of ferrofluids with different and additionally higher concentration compare to next samples: Sample 1 to 4 with 4.5, 9, 18, and 36 mg/ml, respectively.

	M_S [kA.m^{-1}]	χ_{ini} $\times 10^{-3}$ [m^3.kg]	H_c [kA.m^{-1}]	M_R/M_S	μ_{Mag}	$\mu_{Mag(exp.^a)}$ [mg.ml^{-1}]	$\mu_{Mag(exp.^b)}$ [mg.ml^{-1}]
S1	0.24±0.01	0.6±0.1	0	0	0.39±0.03	3.9±0.3	4.5±0.2
S2	0.52±0.03	1.3±0.1	0	0	0.85±0.02	8.5±0.2	9.0±0.5
S3	1.17±0.06	2.8±0.2	0	0	1.90±0.05	19.0±0.5	18.0±1.0
S4	2.18±0.11	5.0±0.3	0	0	3.46±0.07	34.6±0.7	36.0±2.0

Table 5.6: Magnetic properties of coated nanoparticles dispersed in water. The measurements were carried out by VSM.
a: The mass measured with VSM.
b: The mass measured by scale in lab after synthesis.

Figure 5.10 illustrates the correspond graph to table 5.6, showing the increased saturation

magnetization with respect to concentration of nanoparticles in liquid. As it can be seen saturation magnetization of samples increased linearly according to the concentration of samples.

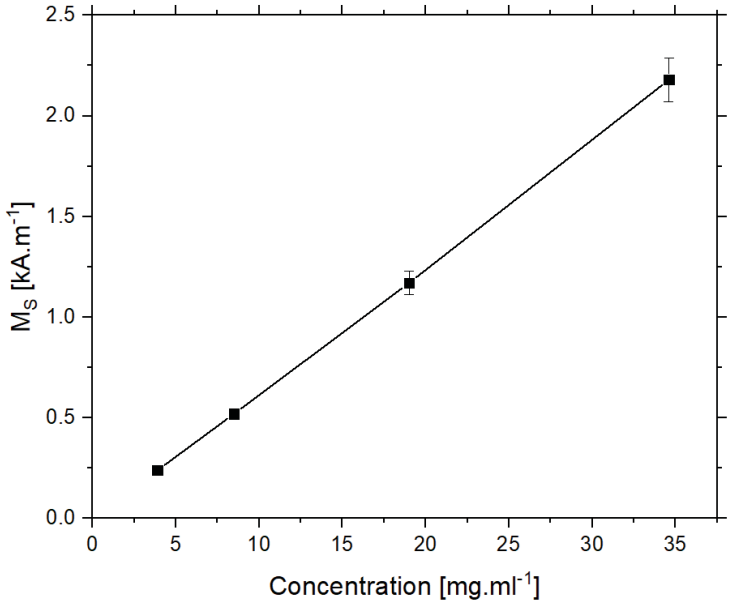

Figure 5.10: Saturation magnetization of the dispersed nanoparticles as a junction of the concentration for samples 1 to 4.

New samples are based on the particle (sample 1-4) as used before were measured. The only deference is the concentration. The concentration of nanoparticles in solution are 250, 500, 1000, and 2000 μg/ml in each samples.

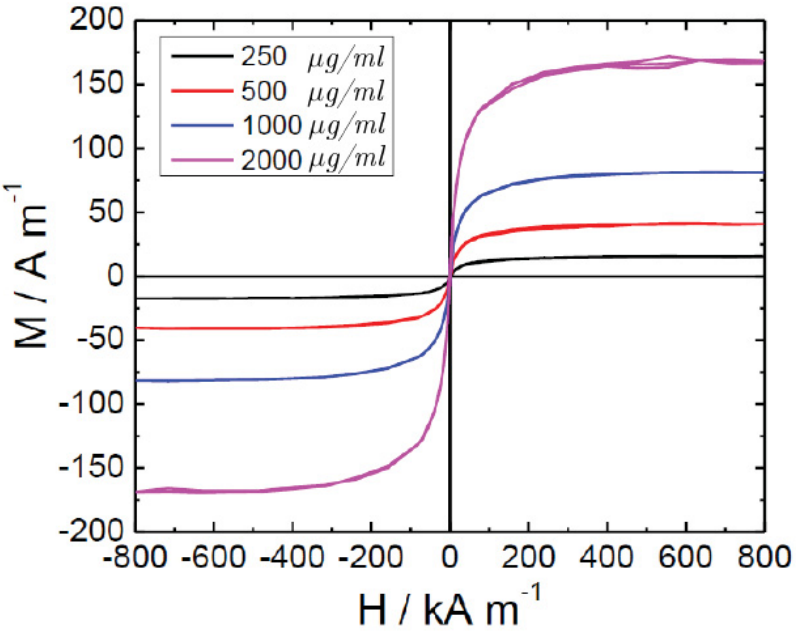

Figure 5.11: Magnetization curves for low concentration dilution of magnetite nanoparticles in water

Figure 5.11 shows the hysteresis curves of the measured ferrofluids. The results obtained from the data are listed in table 5.7.

	M_S [kA.m^{-1}]	χ_{ini} 10^{-3} [m^3.kg]	H_c [kA.m^{-1}]	M_R/M_S	μ_{Mag} [m.%]	$\mu_{Mag(exp.^a)}$ [mg.ml^{-1}]	$\mu_{Mag(exp.^b)}$ [mg.ml^{-1}]
S5	0.015±0.001	2.36±0.03	0	0	0.016±0.004	0.16±0.04	0.25±0.01
S6	0.042±0.002	0.66±0.06	0	0	0.046±0.002	0.46±0.02	0.50±0.02
S7	0.083±0.004	0.15±0.14	0	0	0.900±0.005	0.90±0.05	1.00±0.05
S8	0.173±0.008	0.26±0.25	0	0	0.187±0.006	1.87±0.06	2.0±0.1

Table 5.7: Magnetic properties of coated nanoparticles dispersed in water with the lower concentration. The measurement carried out by VSM.
a: measured with VSM.
b: measured by scale in lab after synthesis.

All samples exhibit the S-shaped curve, which is characteristic for magnetic nanomaterials. As expected, the samples show similar magnetic properties as measured before $(H_C, M_R/M_S = 0)$. The concentration of nanoparticles in water per each sample consist of 250, 500, 1000, and 2000 μg/ml. There is a good agreement between calculated concentration of nanoparticles per sample with VSM and the measured concentration (mass amount of magnetic nanoparticles in 1 ml deionized water) of each sample with scale.
Figure 5.12 illustrates the correspond graph to table 5.7, showing the increased saturation magnetization with respect to concentration of nanoparticles in liquid.

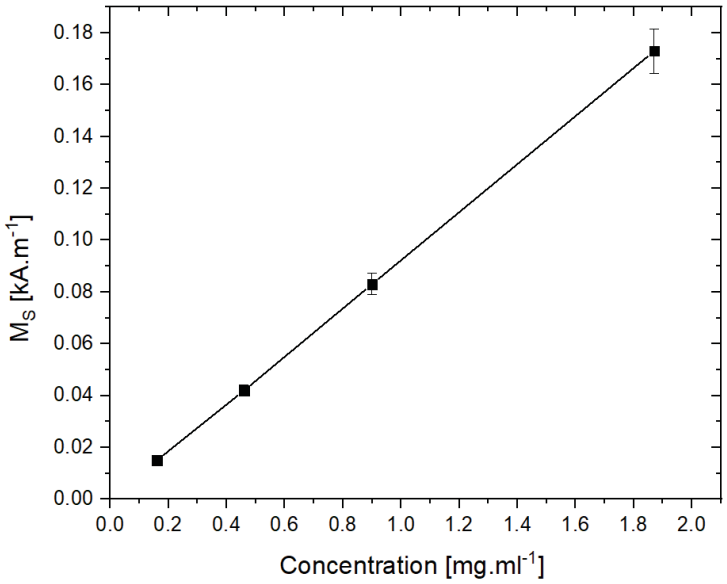

Figure 5.12: Saturation magnetization of the dispersed nanoparticles as a junction of the concentration for samples 5 to 8.

The Data of the VSM measurements are collected and processed as described above, but

within an H-field range of – 800 kAm^{-1} – 800 kAm^{-1}. The collected data are summarized in table 5.7 Four samples, composed of magnetic nanoparticle dispersed in water with different concentrations, were investigated. All curves (Figure 5.11) exhibit a superparamagnetic behavior without any sign of a hysteresis. As expected, the saturation magnetization M_S increases with increasing concentration, as shown in Figure 5.12. This trend is also observable for the volume, the mass fraction μ_{Mag}, and the initial susceptibility χ_{ini}. The magnetic moment *m* as well as the diameter *d* of the magnetic core is more or less constant.

5.1.7 Inductive heating in an oscillating electromagnetic alternating field (OEMF)

The ferrofluids with various concentrations of coated magnetic nanoparticles are investigated in the OEMF. The OEMF is generated by a high-frequency generator, which is connected to a water-cooled copper induction coil. The measurements are carried out with the high-frequency generator *AXIO T5* from Hüttinger. The copper induction coil consists of five windings. An optical temperature sensor *OTGA-62* from Opsens was used for measuring the temperature.

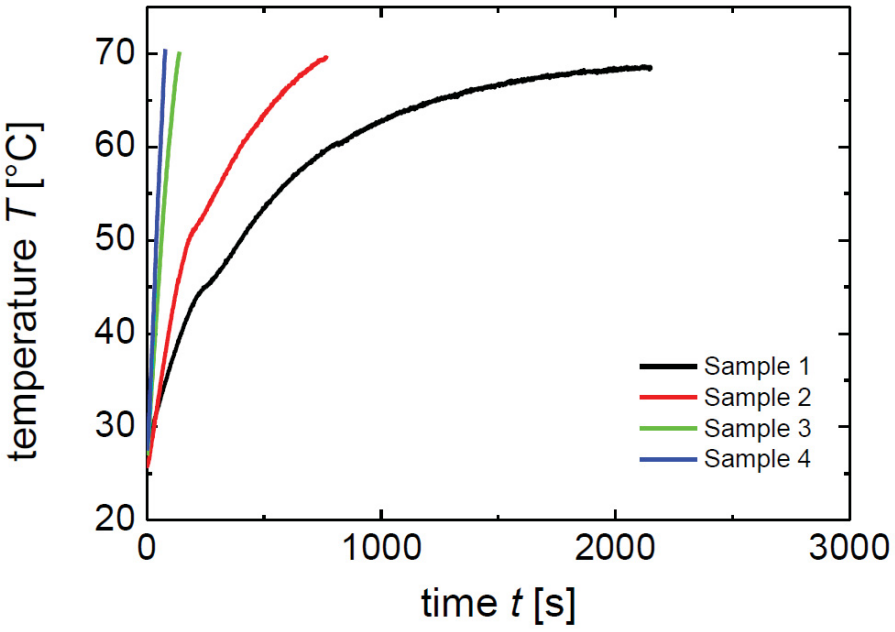

Figure 5.13: Plot of the temperature (*T*) against the time (*t*) of the OEMF-measurement for the ferrofluids with different magnetic content, $_{\text{mag}}$ = 0.39 m.% (black), 0.85 m.% (red), 1.90 m.% (green) and 3.46 m.% (blue).

The measurements are performed at a frequency of 247 kHz and a field strength H of 31.5 $\sim$ kA$\cdot$m^{-1}. The temperature rise of the samples is detected as a function of time by a temperature sensor. The sample is measured in an isolated double glass, which is used for thermal

insulation. The results of all the investigated systems are graphically represented with respect to their heating rate (A) and their saturation temperature (T_S), and finally the specific heating power SHP values of the various systems are computed and compared to each other.
Figure 5.13 shows the plot of the sample temperature *T* versus the time *t* of the OEMF measurement as a function of the particle concentration. After switching the OEM field on (*t* = 0 s), the temperature of the sample increases as a function of time. On the basis of the initial slope dT/dt, the heating rate (A) can be determined, which is required later for the calculation of the SHP (see next section). If the temperature of the sample in the OEMF remains constant, the saturation temperature T_s is reached. The equilibrium between the heat generation in a sample and the heat transfer of the sample to the environment is crucial for achieving the saturation temperature. Though the ratio of the surface area to the volume of the sample plays a large role, all samples are measured under similar conditions and with an equal volume for the correct comparison [145–147]. After the saturation temperature is reached, the applied field is turned off and the temperature of the sample is cooled to room temperature. In order to examine the efficiency of the composites in more detail, the SHP of the various systems is determined and discussed. Specific Heat Power (SHP) describes the amount of energy converted to heat per time and mass and allows an evaluation of the heatability of different particles.

$$SHP = C_p \frac{\frac{dT}{dt}}{\mu_{\text{Mag}}} \tag{5.1}$$

The SHP is calculated by equation (5.1) where C_p is the heat capacity of the matrix (water, $C_\text{p} = 4.18\ \text{J} \cdot \text{g}^{-1} \cdot \text{K}^{-1}$, the heat capacity of the particles has been neglected due to the low concentration of the particles), dT/dt is the heating rate (A) and μ_{Mag} is the mass content of the magnetic material.

Samples	Heating rate dT/dt $[\text{K.s}^{-1}]$
S1	0.088 $\pm$ 0.002
S2	0.189 $\pm$0.004
S3	0.376 $\pm$ 0.002
S4	0.647 $\pm$ 0.003

Table 5.8: Heating rate of the samples with high concentration.

The influence of OEMF on the samples with higher concentration is also measured and shown in Tables 5.8. The samples are based on the same particle charge as (sample 1-4) used before. As mentioned above, the only difference is the concentration of the particles in the fluid and that some of them are coated with Aminosilane. This was also approved via VSM measurement and the particles show similar magnetic properties.

To allow an on-demand homogenous heating of the magnetic solution, the dispersion stability is very important for the OEMF measurement and heating. Due to the reason that the solution shows no dispersion stability, it is expected to have no homogenous heating in the solution. Moreover the agglomeration of the particles will lower the Brownian relaxation of the particles and leads to lower heating rate and after very short time the Néel relaxation might be dominant. However, it is expected, that the particles in cells show just Néel relaxation.

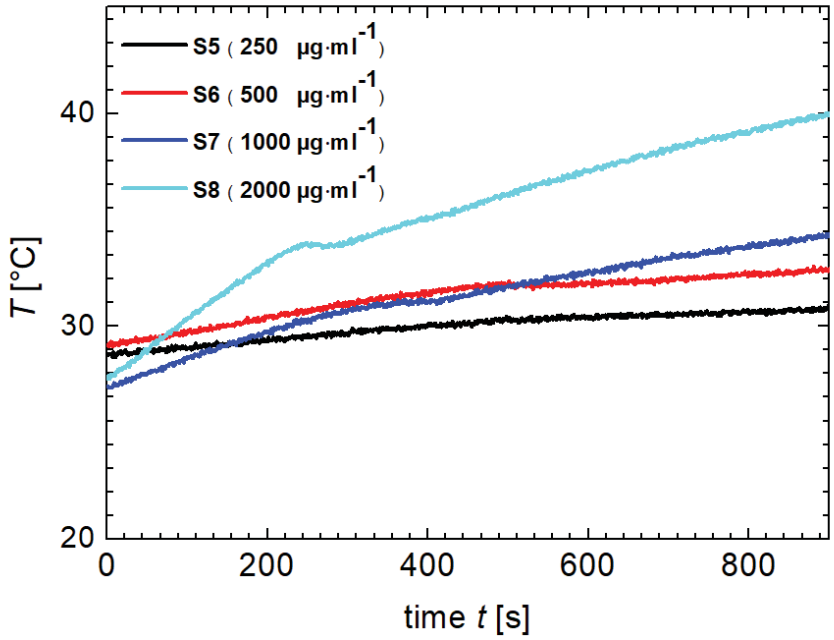

Figure 5.14: Plot of the temperature (T) against the time (t) of the OEMF-measurement for the ferrofluids (coated nanoparticles) with lower magnetic content.

Four new samples Figure (Figure 5.14) are prepared after optimizing the concentration of the particle in order to allow a noticeable increase of the temperature under OEMF. After optimizing the concentration, samples with 1000 and 2000 μg $\cdot$ ml^{-1} show a noticeable increase in the temperature. The temperature increase of an isolated sample 1000 μg $\cdot$ ml^{-1} is about $\triangle T \approx 8$℃ within 15 min and in sample with 2000 μg $\cdot$ ml^{-1} is about 13 ℃. The heating rate (Table 5.9) in a sample with 250 μg $\cdot$ ml^{-1} is about $(\frac{dT}{dt})$ $0.002K \cdot s^{-1}$. In this case the temperature remains around room temperature and the standard deviation is about 100 $\%$.

Samples	Heating rate dT/dt $[K.s^{-1}]$
S6	0.0048 $\pm$ 0.002
S7	0.0140 $\pm$ 0.001
S8	0.0360 $\pm$ 0.005

Table 5.9: Heating rate of the samples with lower magnetic content.

In Figure 5.15 the heating rate is plotted against the particle concentration. A direct dependence of the heating rate on the particle content can be seen as expected. Based on the linear relationship between the heating rate and the particle concentration, the SHP for the ferrofluids is calculated by equation (5.1), where $(\frac{dT}{dt}\frac{1}{\mu_{Mag}})$ is the slope of the curve in Figure 5.15. This results in a specific heat power of 79.6 W $\cdot$ g^{-1} for the magnetite particle.

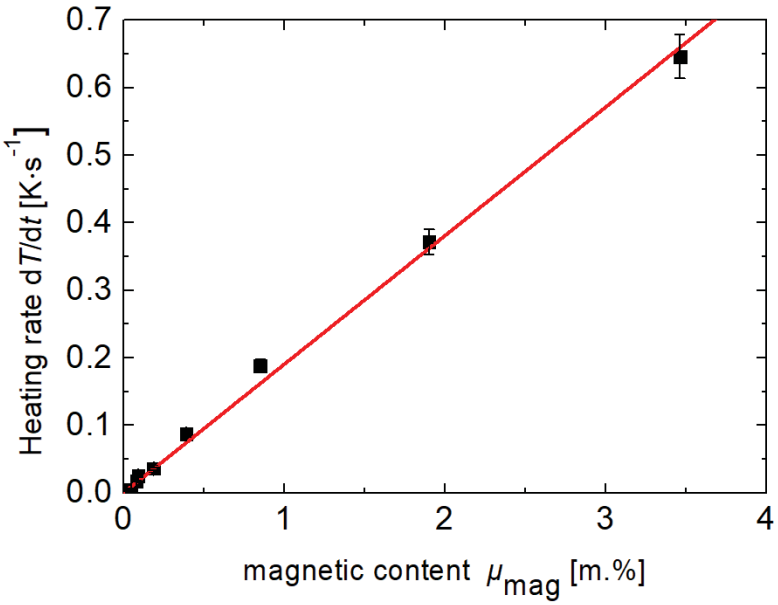

Figure 5.15: Plots of heating rate (dT/dt) against the magnetic content μ_{mag} for all the samples.

5.2 Biocompatibility and uptake of iron oxide nanoparticles by cells

5.2.1 Viability of the cell lines

The BPH1 and PC3 cells were treated for 24 hours with 100 and 500 μg/ml of MNP and APTES-MNP and the cell viability was measured by MTT assay (Figure 5.16). In both cell lines, the higher viability is observed for coated nanoparticles (APTES-MNP). The BPH1 cells treated with 100 μg/ml MNP, show 72% (MNP) and 86% (APTES-MNP) viability. Lower levels of toxicity were observed for PC3 cells with 87% and 88%. This trend is also seen for a concentration of 500 μg/ml. The higher concentration of the MNP results in the lower cell viability for both tested cell lines. Collectively, in both conditions PC3 cells illustrated more viability than BPH1 cells. In the same line of evidence, Naqvi and colleagues reported after 6 hours of treatment with MNP 95% viability at the concentration 25-200 μg/ml and 55%-65% viability at the higher concentra-tion 300-500 μg/ml [148].

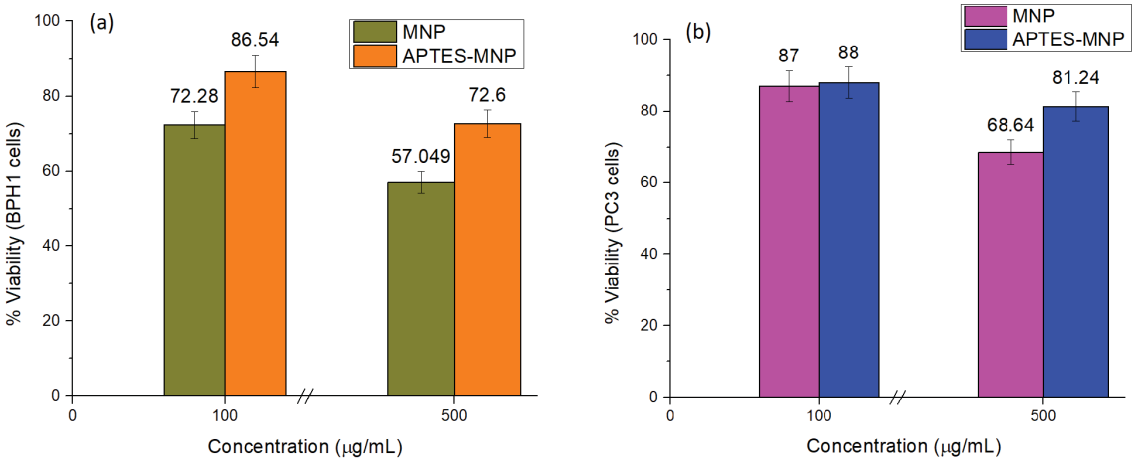

Figure 5.16: MTT analysis of cell viability of BPH1 cells (a) and PC3 cells (b) shows the decreased the cell viability depending on concentration of coated and uncoated MNPs.

5.2.2 Investigation of cellular uptake by TEM

In order to compare the effect of surface functionalization in NP uptaking and the mechanism of the internalization, the cellular uptake of MNP and APTES-MNP with different concentrations of 100 and 500 μg/ml, was examined for two cell lines of PC3 and BPH1 by TEM (s. Figs 5.17 - 5.20) and flow cytometry (s. Figs 5.21 and 5.22). The cells were seeded on 6-well plates and after reaching 70% to 80% confluency, they were treated with MNP for 24 hours. We observed that after the exposure of nanoparticles to the cells, first of all the nanoparticles

adhere to the surface and subsequently, due to endocytosis, they internalize to the cells followed by agglomeration inside the cells (s. Figs, 5.17 - 5.20) [139]. In the case of PC3 cells (s. Fig. 5.19), it is obvious that with increasing concentration of particles, the cells take up more particles, which accumulate in bigger agglomerations.

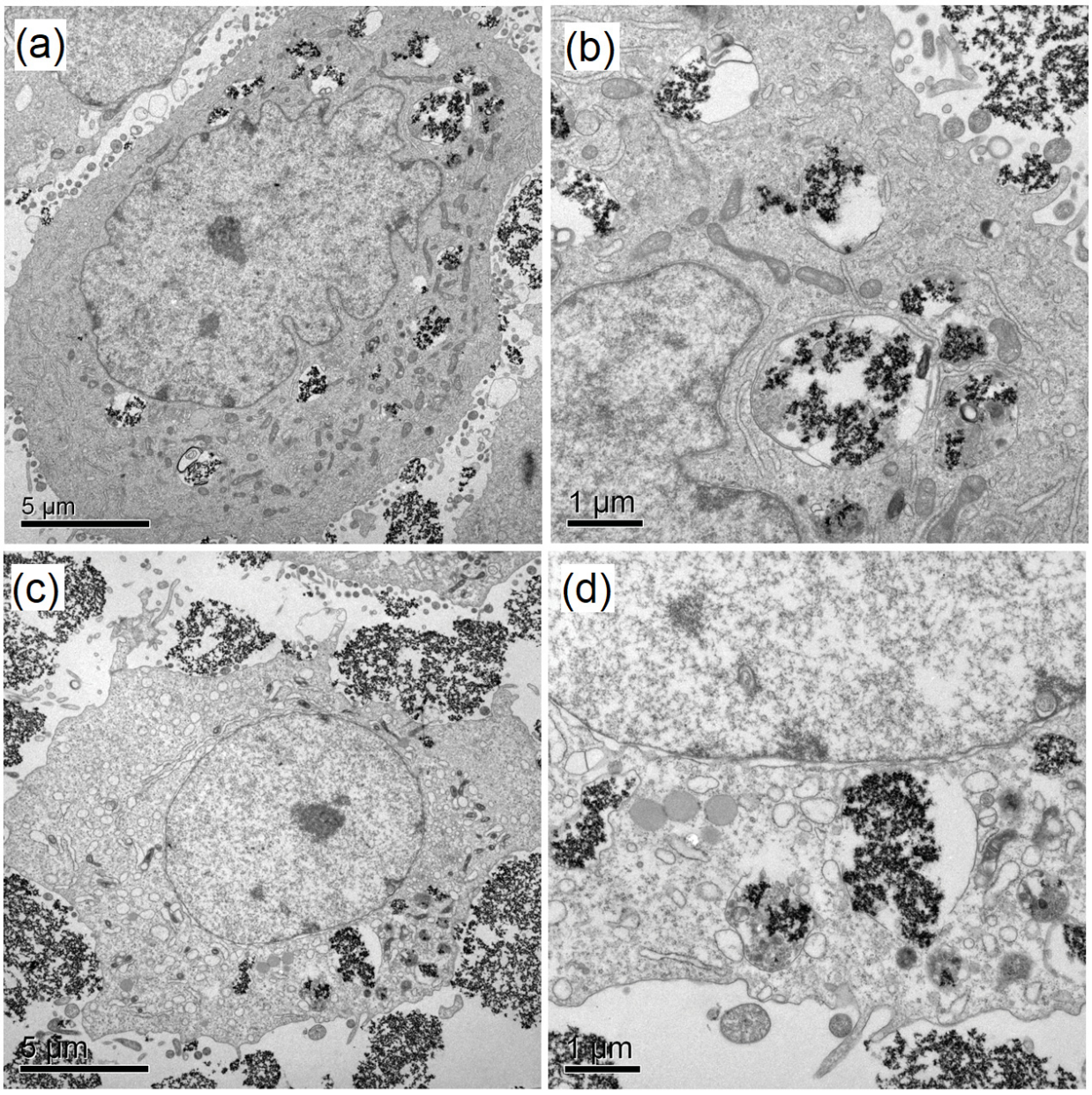

Figure 5.17: TEM images of PC3 cells fixed after treatment and incubation for 24 hours with uncoated nanoparticles (MNP): treatment with 100 μg/ml (a, b) and 500 μg/ml (c, d) with magnification of 5000× (a, c) and 15000× (b, d).

In contrast, the benign cells take up particles at the lower levels in comparison with PC3 prostate cancer cells. The same results were obtained for the both conditions, 100 and 500 $\sim\mu$g/ml of particles (s. Fig. 5.20), which is in agreement with previous studies [106]. Collec-

tively, our data indicate that the prostate cancer cells take up the coated particles with higher efficiency than benign cells. In contrast to the treatment by coated particles, treatment with MNP shows different results, which indicate the effect of surface structure in cellular uptake of NP [95]. In contrast to the coated MNP, treatment of cells with the uncoated NPs results in more particles internalized to the normal cells-BPH1 (related to the negative control) in comparison to cancer cells (Figures 5.17 and 5.18). There are different factors that may affect the nanoparticles´ uptake efficiency such as charge, size, shape and surface modification of the nanoparticles itself as well as cell types.

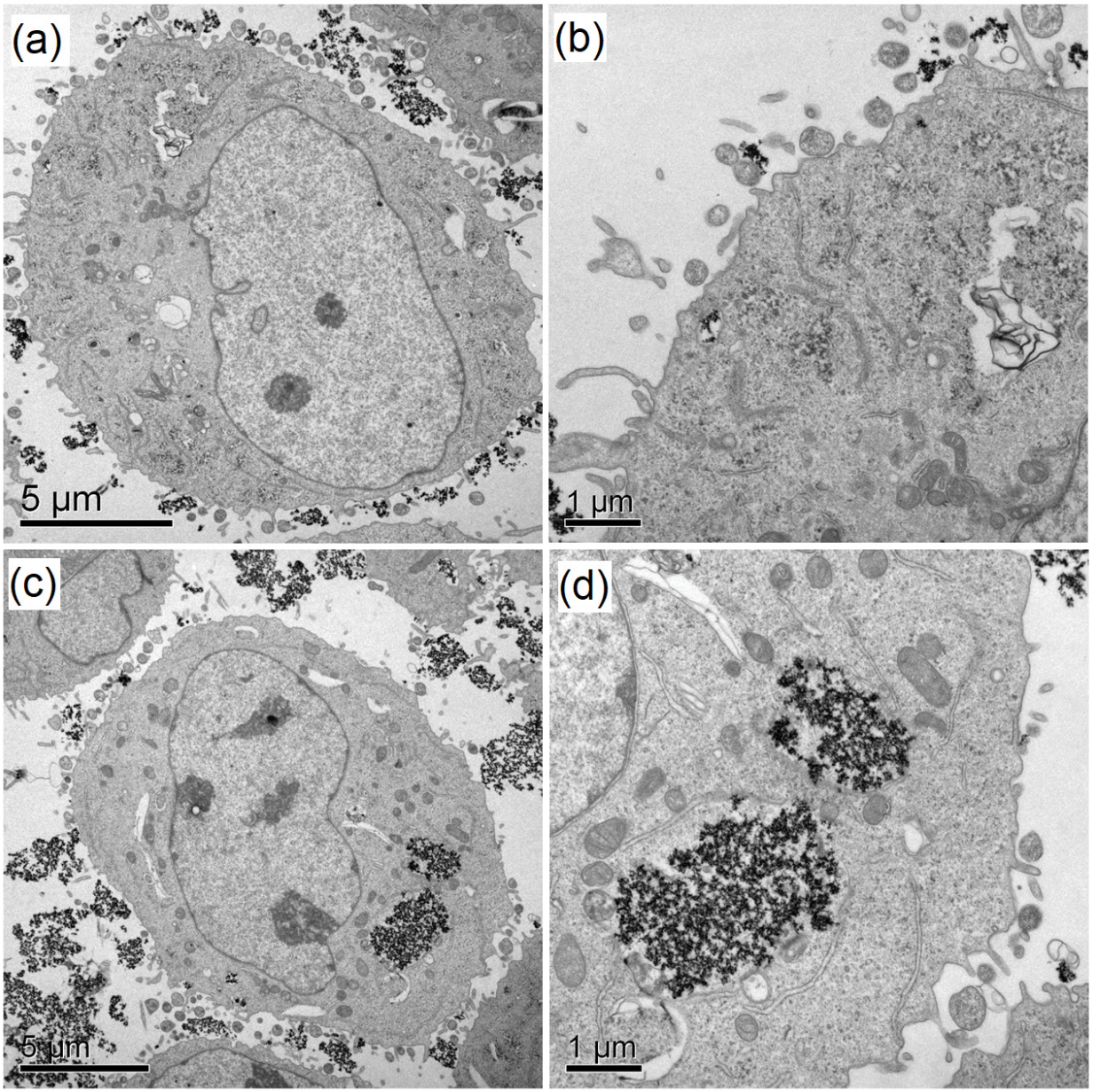

Figure 5.18: TEM images of BPH1 cells fixed after treatment and incubation for 24 hours with uncoated nanoparticles (MNP): treatment with 100 μg/ml (a, b) and 500 μg/ml (c, d) with magnification of 5000× (a, c) and 15000× (b, d).

The interaction of cells is also different with the negatively and positively charged particles because of electrostatic properties [121]. The efficiency of the cellular NP uptake could be different among the various cells and this is mainly due to the cell type specific features of various cells and cell dynamics.

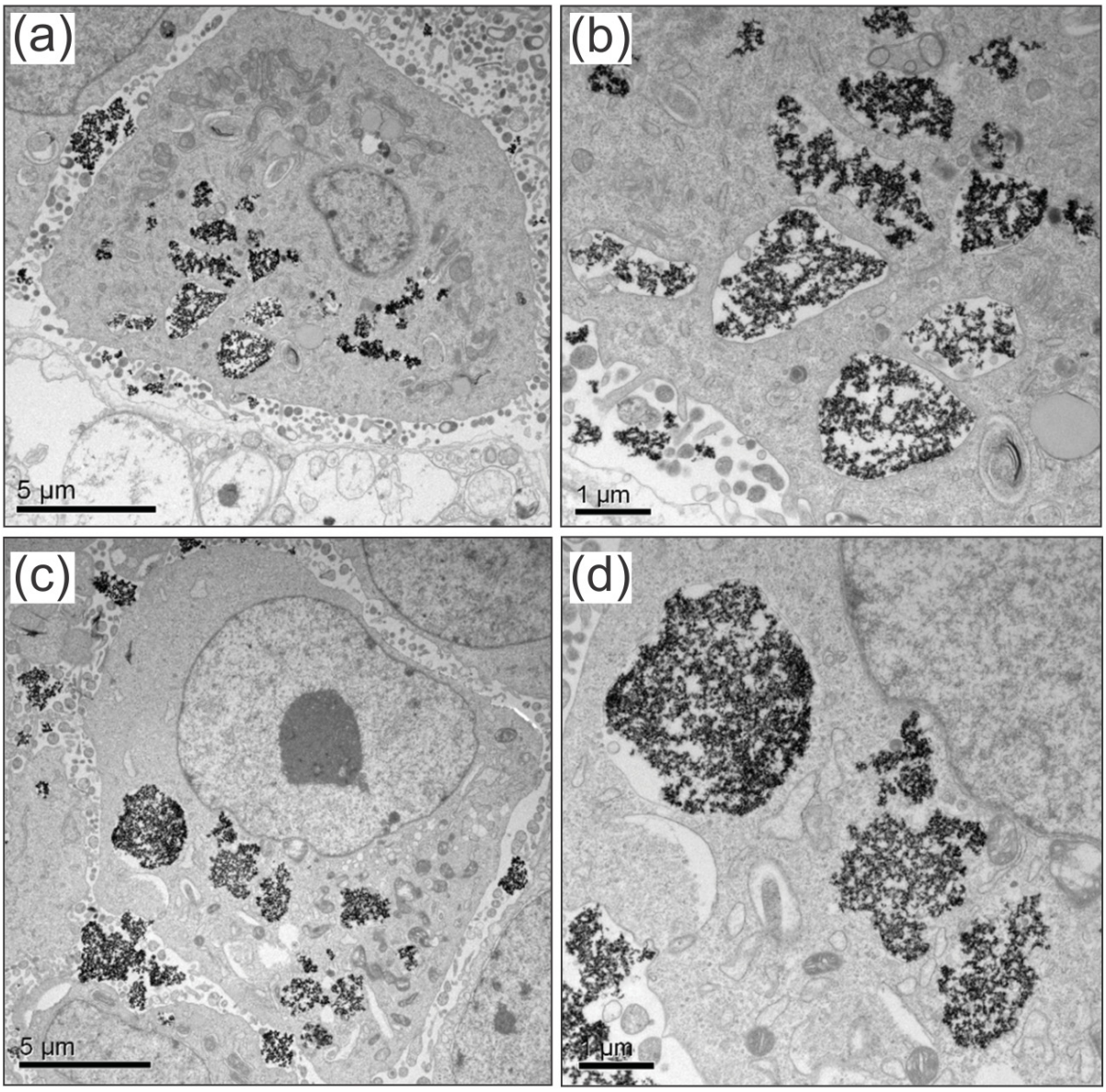

Figure 5.19: TEM images of PC3 cells fixed after treatment and incubation for 24 hours with APTES-MNP: treatment with 100 μg/ml (a, b) and 500 μg/ml(c, d) with magnification of 5000× (a, c) and 15000× (b, d).

Several endocytic pathways can regulate the nanoparticles entry to the cells, such as pinocytosis, clathrin or caveolin dependent and clatherin-caveolon independent pathways [30]. In the same line of evidence, Chaves and colleagues showed that the breast cancer cells up-

take with higher efficiency NP than normal cells [107]. They reported this is via a clathrin-dependent endocytosis pathway and cancerous cell line express higher amount of clathrin but not caveolin than normal cells. However, the exact mechanism of the cells` uptake needs further investigations in order to clarify in which pathways cells take up the nanoparticles.

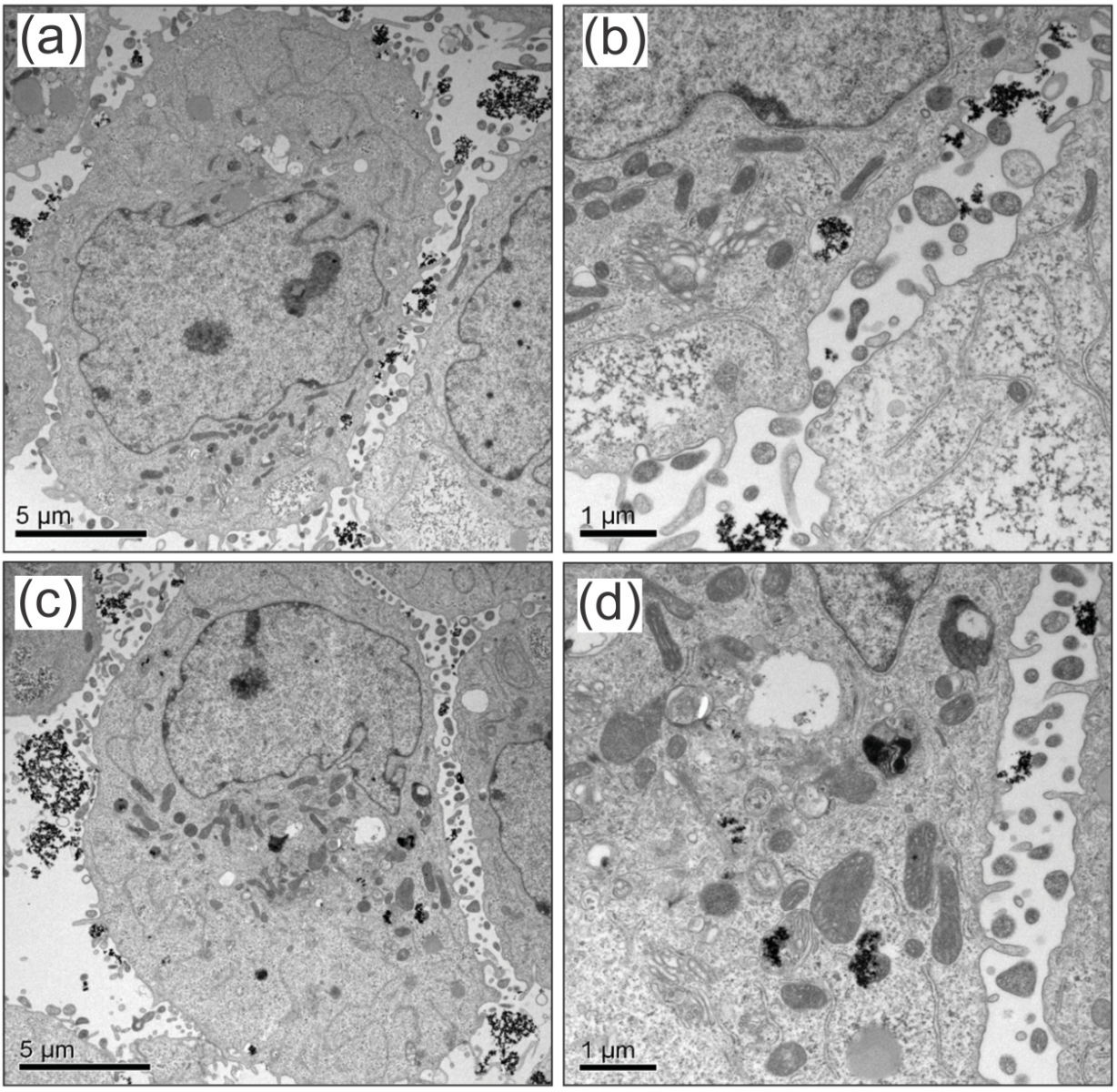

Figure 5.20: TEM images of BPH1 cells fixed after treatment and incubation for 24 hours with APTES-MNP: treatment with 100 μg/ml (a, b) and 500 μg/ml (c, d) with magnification of 5000× (a, c) and 15000× (b, d).

5.2.3 Investigation of cellular uptake by flow cytometry

To quantify the uptake of nanoparticles by the cells in a dose dependent comparison, flow cytometry measurements have been applied. This allows the determination of the magnetite nanoparticles` internalization by PC3 and BPH1 cells. The flow cytometry results of treatment with MNP to the cells are presented in Fig. 5.21 to Fig. 5.22 and with APTES-MNP are illustrated in Fig. 5.23 and Fig. 5.24. Flow cytometry measurements evaluated reactions of cells to magnetite nanoparticles with 0 (as a control), 100 and 500 μg/ml concentration quantitatively after treatment and incubation for 24 hours [133, 149]. Forward scatter (FSC) and side scatter (SSC) are two parameters to assess and observe the cellular uptake. Forward light scattering gives information about the cell size and side scattering about the internal structure, organelles and generally internal complexity [150]. As shown in Fig. 5.22 and Fig. 5.23, SSC signals grow with increasing concentration of the particles, which demonstrates higher uptake of particles.

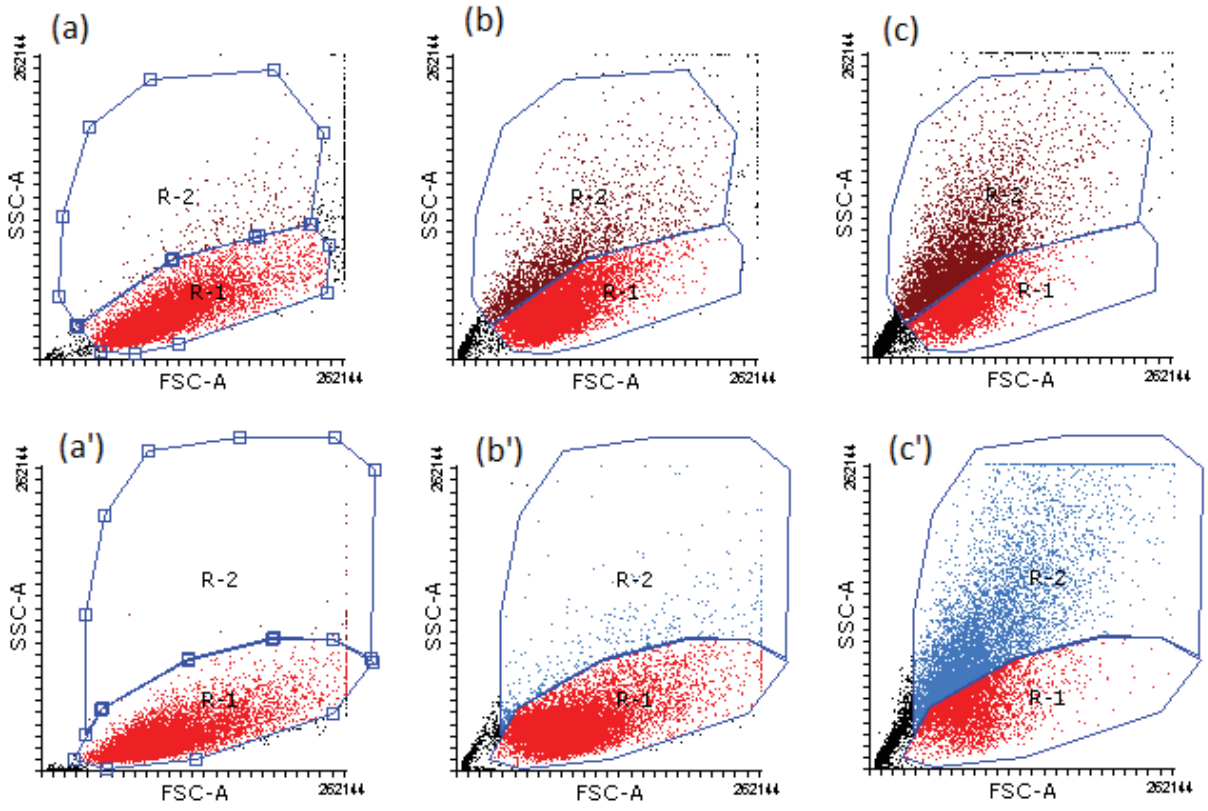

Figure 5.21: Flow cytometry cytogram of SSC and FSC which are treated by magnetite nanoparticles (MNP): (a, b, c) showing PC3 cells with a concentration of 0, 100, and 500 μg/ml, respectively and $(a^{'}, b^{'}, c^{'})$ presenting BPH1 SSC cytogram with the same concentration.

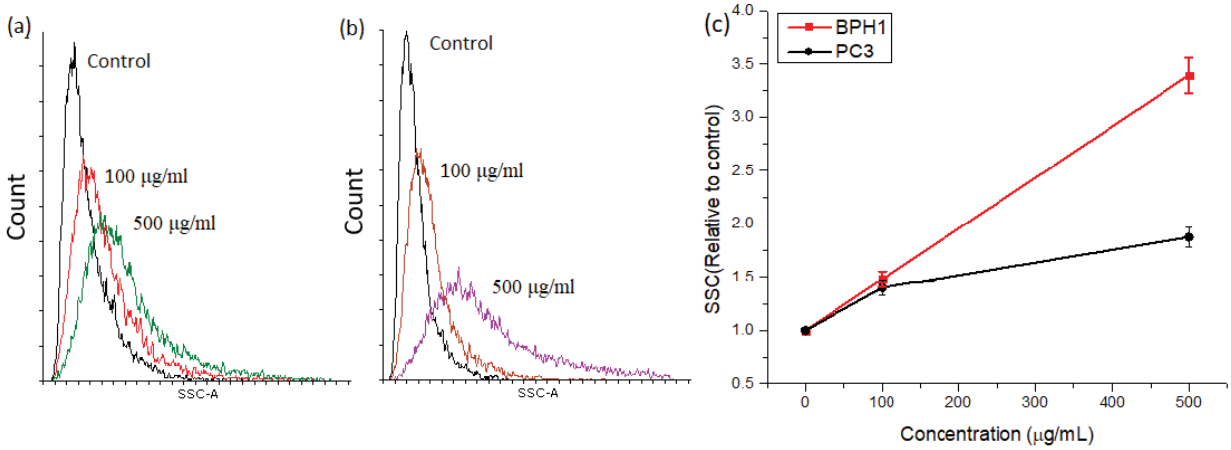

Figure 5.22: (a,b) Flow cytometric analysis of PC3 and BPH1 treated with magnetite nanoparticles (MNP), resp. SSC increases with increasing concentration in both cells by MNP treatment. (c) SSC (relative to control) changes with concentration for PC3 (black line) and BPH1 (red line).

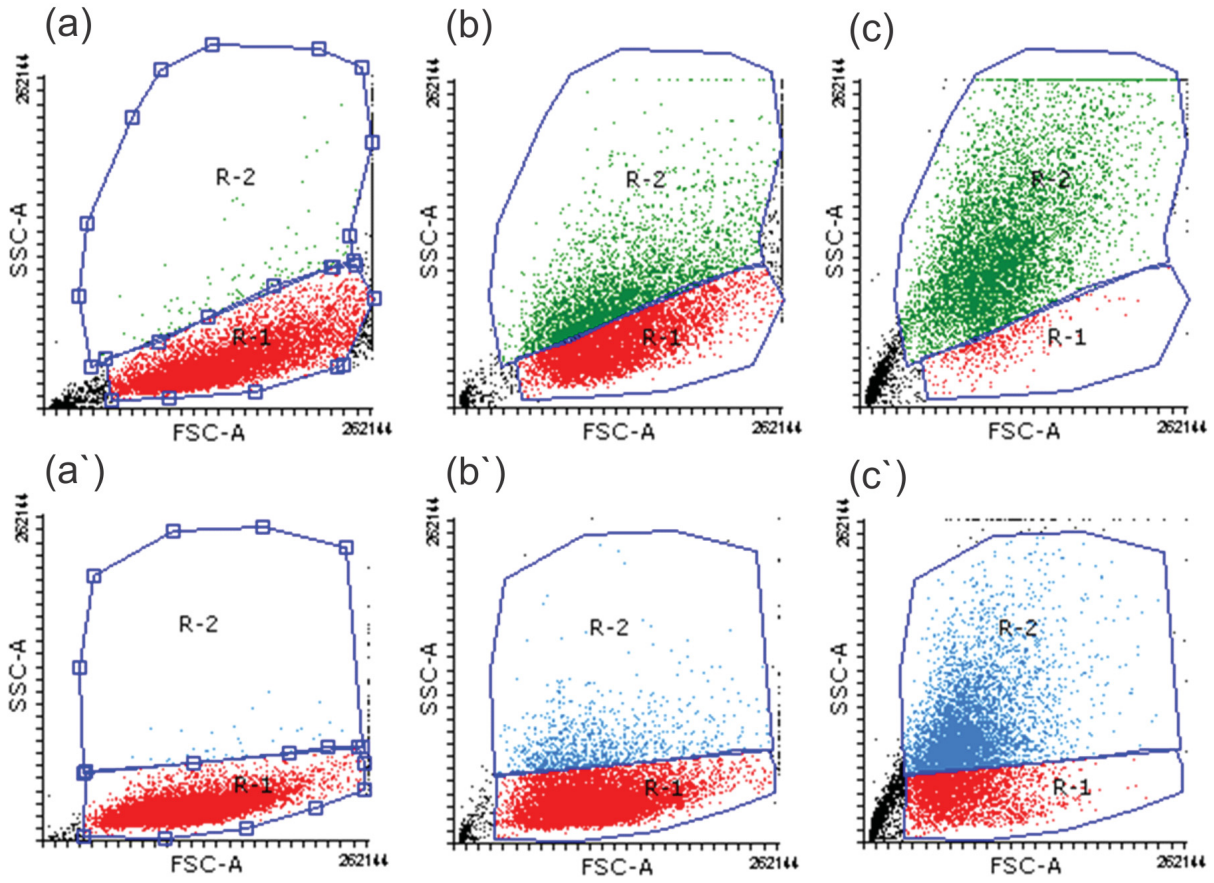

Figure 5.23: Flow cytometry cytogram of SSC and FSC which are treated by APTES-MNP: (a, b, c) showing PC3 cells with a concentration of 0, 100, and 500 μg/ml, respectively and (a', b', c') presenting BPH1 SSC cytogram with the same concentration.

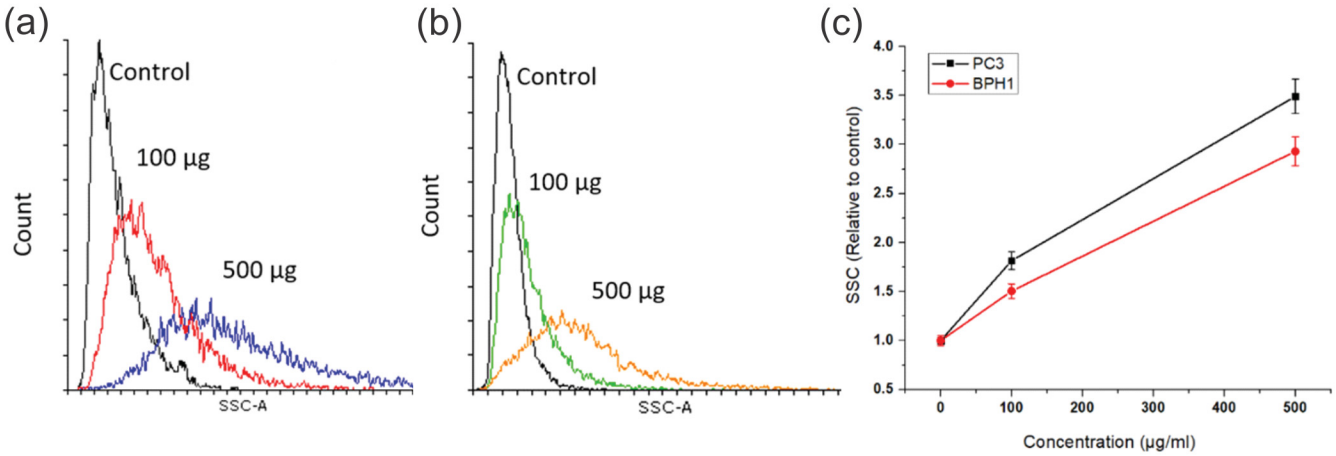

Figure 5.24: (a,b) Flow cytometric analysis of PC3 and BPH1 treated with APTES-MNP, resp. SSC increases with increasing concentration in both cells. (c) SSC (relative to control) changes with concentration for PC3 (black line) and BPH1 (red line).

In contrast, FSC intensity decreases with increasing APTES-MNP concentration that is explained because of absorbing and reflecting the light from nanoparticles [133]. To distinguish between cells with particles and without particles, two regions were defined. R-1 was used to clarify the control cell samples and R-2 was used to show cells after treatment with different concentration. These tests revealed that the cells with 500 μg/ml of particles treatment exhibit a huge growth in size. As expected, these experiments also demonstrate the same trend for BPH1. Figure 5.21 presents the application result of MNP to both cell lines. In flow cytometry histogram granularity of the cells does not show significant changes between PC3 and BPH1 but in flow cytometric analysis (Fig. 5.22), which concerns to the cells without nanoparticles treatment, granularity of BPH1 cells increased more than cancer cells.

These tests revealed that the cells with 500 μg/ml treatment exhibit a huge growth in size. As expected, these experiments also demonstrate the same trend for BPH1. There is a perfect agreement between TEM and flow cytometry results that shows PC3 take up nanoparticles significantly more than BPH1. The evaluation of dose dependent uptake is plotted in Fig. 5.24 (a, b for PC3 and BPH1 cells, resp.). It is obvious that the SSC intensity increases with increasing concentration for PC3 and similarly for BPH1. Mean side scatter changes are also plotted in Fig. 5.24 c.

5.3 Cultivation and enrichment of Anaerobian/Microaerophilic Bacteria

The procedure of cultivation, enrichment and extraction of two types of magnetotactic bacteria will be explained in this section in order to be used for hyperthermia. It seems the magnetotactic bacterium are the best candidate for hyperthermia. The reason is the nanoparticles in magnetosomes do not tend to aggregate but they are still close enough to have high heating efficiency *in-vivo*.

Magnetotactic bacteria synthesized the magnetite nanoparticles (magnetosomes). They are good self-assemble promoters because they have extremely low size, shapes, and reproducibility dispersity [151]. Due to their genetic control that bacteria perform during their biomineralization process, they perform very high chemical, structural, and magnetical quality [151]. The nanoparticles have the lipid bilayer cover with the thickness of 2 to 4 nm. This membrane causes the electrostatic stability that protect nanoparticles from aggregation. The other advantages is to control the minimum distance between nanoparticles during self-assembly [152].

The goal of this part is to optimize the cultivation of bacteria and produce higher concentration of magnetosomes in order to be used for hypertherima. Therefore, beside synthesis the magnetite nanoparticles by coprecipitation technique, we cultivate the magnetotactic bacterium that is supposed to be continued and applied for following master and PhD projects.

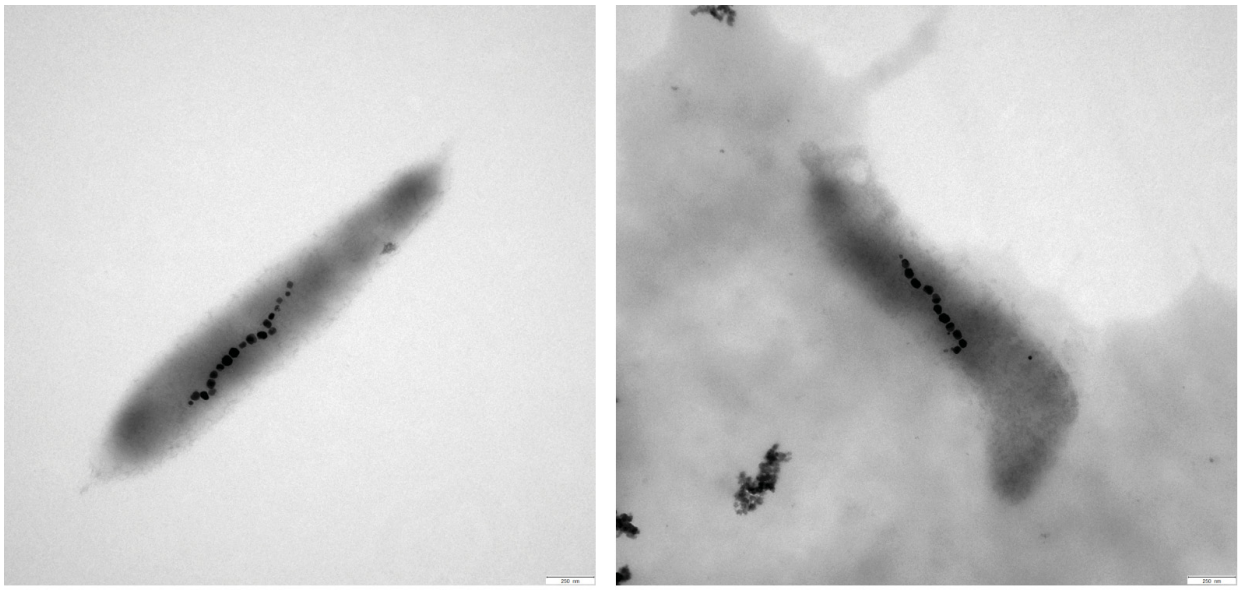

Figure 5.25: TEM images of two cultivated MS-1 bacteria holding magnetosomes in bacteria cell wall.

5.3.1 Cultivation of magnetotactic bacteria

In this section the result of the cultivation of two kinds of magnetic bacteria, magnetospirillum magnetotacticum (MS-1) and magnetospirillum gryphiswaldense (MSR-1) is presented. The measurements are carried out with TEM. The cell devision of bacteria can be seen, which is the main criteria for cultivation. The presence of cell devisions in TEM measurements is the evidence of cultivation process in the medium.

Magnetospirillum magnetotacticum MS-1 The magnetospirilium magnetotacticum bacteria were cultivated as described in the last chapter. After cultivation of bacteria they have been enriched in order to obtain higher concentrations of these bacteria. As it can be seen in Figure 5.25 and as an overview in Figure 5.28 and more examples of TEM measurements the average of nanoparticles´ number in each bacteria is approximately 16 particles. There are also some bacteria containing more and less numbers of particles. Additionally, some single particles are observable, which are not formed in the chain. The ImageJ program is used to measure the size of particles. The size distribution of nanoparticles is about 20 to 70 nm with the average size of 43 nm. The evaluation of measurement is presented in Figure 5.26, which is a common in the form of master thesis. The evaluation is calculated by Origin.

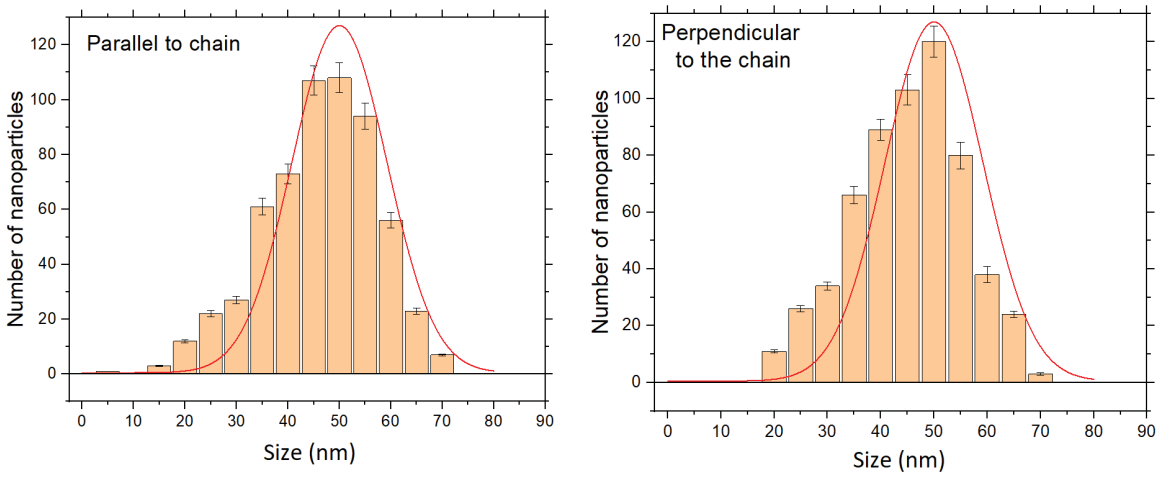

Figure 5.26: Size distribution of magnetosomes in MS-1 bacteria parallel and perpendicular to the chain.

As it can be seen in Figure 5.26 the size of more than hundreds nanoparticles are measured automatically which is calculated by means of ImageJ program in perpendicular and parallel directions. In order to investigate individually the ratio of single nanoparticles, the size of particles perpendicular and parallel to each other is measured and is shown in Figure 5.27. This analysis was carried out with limited number of nanoparticles. Therefor, the presented

distribution resulted in figure 5.27 cannot be correlated to nanoparticles distribution in Figure 5.26.

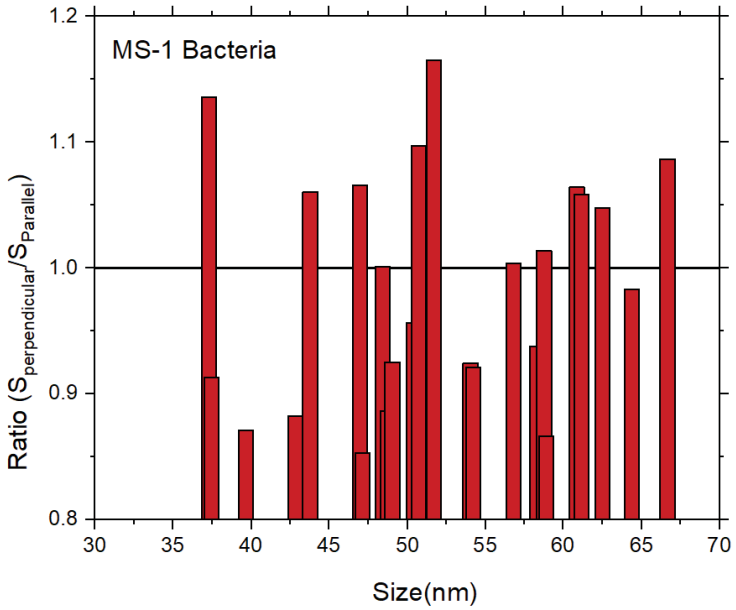

Figure 5.27: The overview of cultivated MSR-1 with the scale bar of 2500 nm.

As it can be seen they are mostly in the range of 40 to 60 nm and are more populated around 45 to 55. The size of particles in perpendicular direction is mostly smaller that the size of particles in parallel direction. It means the particles are elongated parallel to the chain that is why the graph is showing more bars smaller than one.

Magnetospirillum gryphiswaldense MSR-1 In gryphiswaldense bacteria MSR-1, around 81% contain 10 to 11 nanoparticles, which increase the ability of effective magnetotaxis. MSR-1 bacteria show better growing value compared to MS-1. The reason stays behind the less percentage of oxygen that they need to cultivate in comparison to MS-1. In other words they are less sensitive to oxygen. This makes the situation more beneficial for their cultivation. Figure 5.28 shows an overview of MSR-1 bacteria showing higher concentration of bacteria.

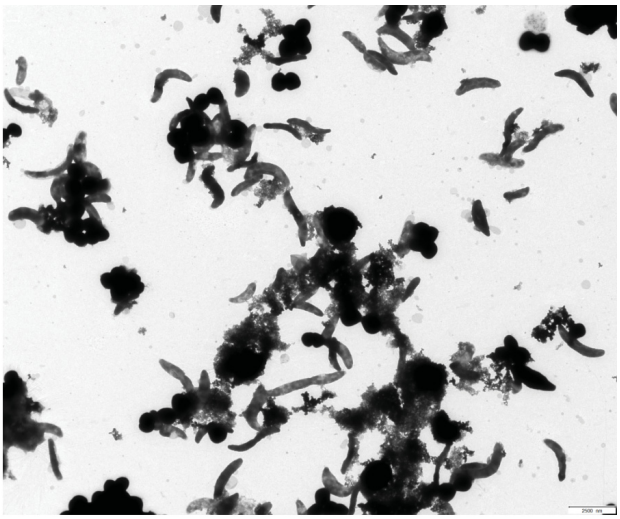

Figure 5.28: The overview of cultivated MSR-1 with the scale bar of 2500 nm.

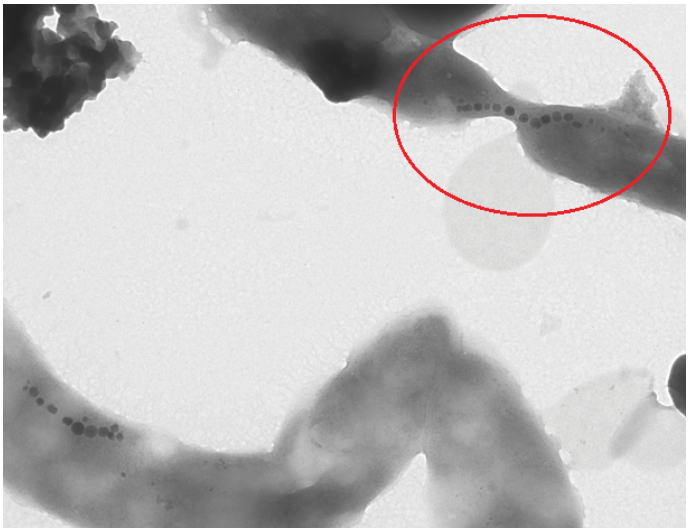

Figure 5.29: TEM images of cultivated MSR-1 bacteria. The red circle shows the cell devision of bacteria.

In figure 5.29 the cell division of one MSR-1 bacterium is shown, which is more frequent compared to MS-1 bacteria. The average size of particles are 40.3 nm with the standard deviation of 9.1 nm. The size of nanoparticles in perpendicular direction is almost the same as parallel, with 40.6 nm, with the standard deviation of 8.6 nm. Figure 5.30 shows the histogram of size distribution of particles in two directions, parallel and perpendicular to the chain. According to this analysis most of the particles are showing the size distribution between 35 to 50 nm.

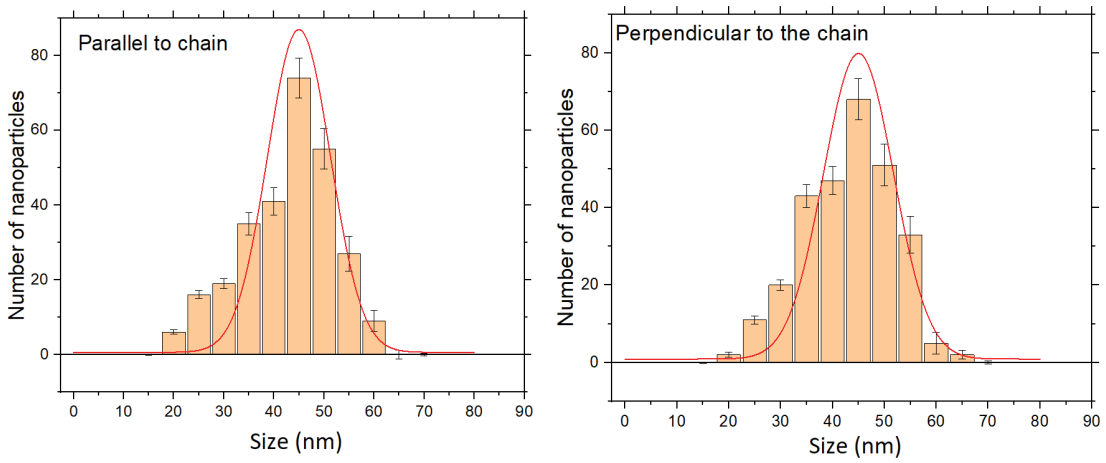

Figure 5.30: Size distribution of magnetosomes in MSR-1 bacteria parallel and perpendicular to the chain.

The ratio of nanoparticles size perpendicular and parallel to each other are also measured for MSR-1 bacteria and is shown in Figure 5.31.

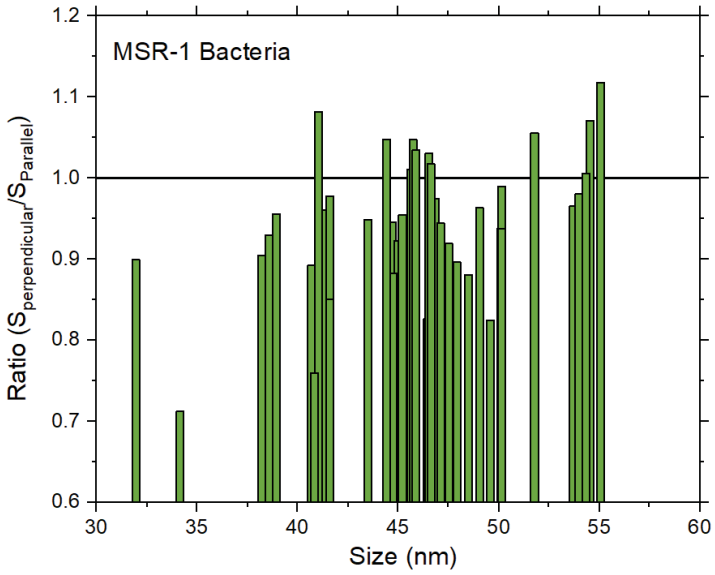

Figure 5.31: The overview of cultivated MSR-1 with the scale bar of 2500 nm.

As it explained for the ratio analysis of MS-1 bacteria, the same can be seen also for MSR-1 bacteria. It can be seen in Figure 5.30 that the size of more than hundreds nanoparticles are measured automatically which calculated by means of ImageJ program in perpendicular and parallel directions. In order to investigate individually the ratio of single nanoparticles, the size of limited particles perpendicular and parallel to each other is measured and is shown in Figure 5.31. Therefor, the presented distribution resulted in figure 5.31 cannot be correlated to nanoparticles distribution in Figure 5.30.

As it can be seen they are mostly in the range of 30 to 55 nm and like MS1 bacteria are more concentrated around 40 to 55 but mostly around 45 to 55. The size of particles in perpendicular direction is mostly smaller that the size of particles in parallel direction. The same pattern like MS1 bacteria which show elongation of bacteria in parallel direction to the chain. Therefor, more bars are showing smaller size than one.

5.3.2 Extraction of the magnetosomes from bacteria

In order to extract the magnetosomes from bacteria two different methods are applied. First of all lysozyme is used for breaking the bacterias' cell wall and then ultrasonic waves are used to extract the magnetosomes from bacteria. In another method, we combined lysozyme and EDTA to proceed the extraction.

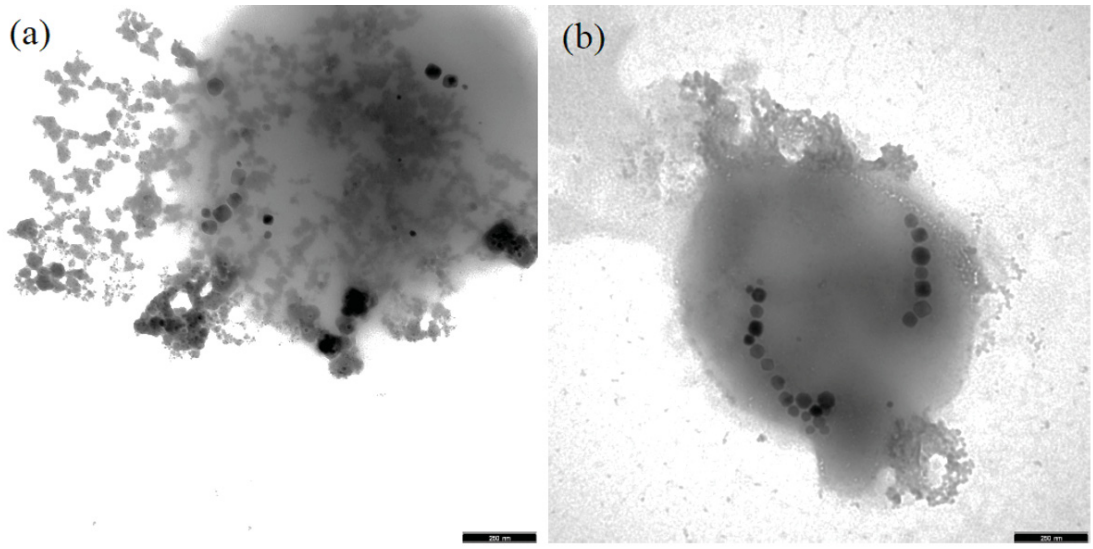

Figure 5.32: The TEM images (with 250 nm scale bar) of bacteria are shown in different forms effected by lysozyme. The nanoparticles are distributed over the sample in Figure (a) and the magnetosomes are still aligned in the form of two parallel bacteria attached together Figure (b).

Figure 5.33: The MTB bacteria containing linear magnetosomes chain in the cell wall bacteria affected by lysozyme but not destroyed. The scale bar is about 250 nm.

Using lysozyme as an extracting material As explained in experimental part, by adding the lysozyme, the cells` walls are still observable around the magnetosome and also they are still aligned in the form of chains. Figure 5.32 is showing the cell walls that are more effected by lysozyme and Figure 5.33 illustrate the bacteria in its original form, effected slightly. The results are presenting the necessity of other methods or chemicals to break the bacteria completely.

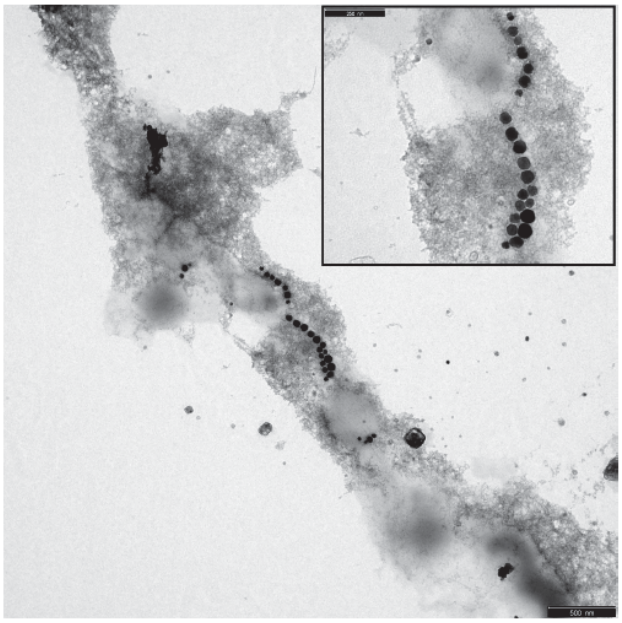

Figure 5.34: The TEM images of MTB bacteria after 10 seconds ultrasonication with 24W.

Extraction in combination with ultrasonic wave After applying the lysozyme, ultrasonic waves are used by different power. The optimal power is obtained on 40% of overall energy of ultrasonic instrument, which means 24 W. The cell walls are broken by 40% of energy. In Figure 5.34 the magnetospirilium magnetotacticum bacterium is illustrating two aligned chains of bacteria in destroyed cell wall.

Extraction with lysozyme and EDTA In the last two paragraphs the application of lysozyme and ultrasonic technique is examined for extraction of bacteria but they were not enough to break the cell wall. Therefore, EDTA was used additionally with lysozyme. In order to do that half part of lysozyme was replaced by EDTA. In Figure 5.35 the TEM images of extracted magnetosomes with lysozyme and EDTA are presented. The chain of magnetosomes are clearly separated and identified from the cell membrane. It can be seen that the magnetosomes are aligned nonlinear but still enclosing in their membran (Figure a) and in Figure b is presented the linear magnetosomes and also individual particles not in the chain.

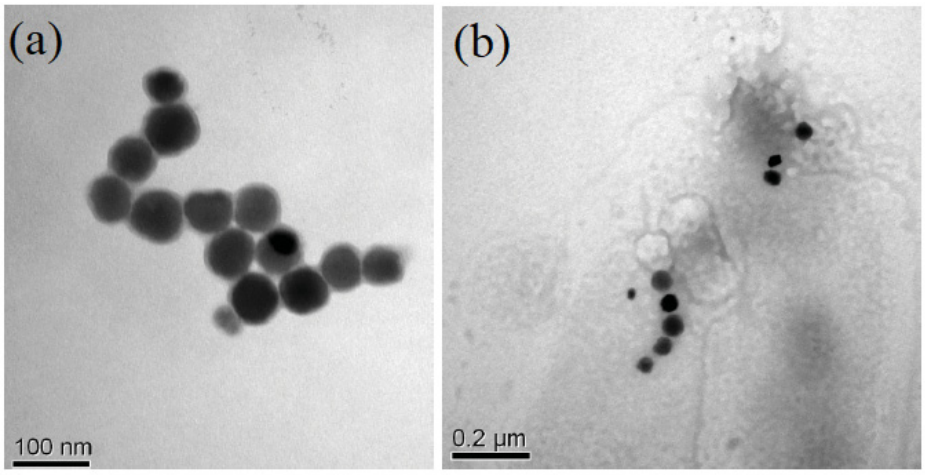

Figure 5.35: The TEM images of (a) non-linear fully extracted magnetesome chain from cell wall and (b) linear extracted and single particles of MS-1 bacteria.

6 CONCLUSION

In this chapter an overview and conclusion of the projects are given. The conclusion is divided into three parts includes: magnetic nanoparticles synthesis and related characterization, nanoparticles-cell experiments, and the third part refers to nanoparticles from microaerophilic magnetotactic bacteria.

6.1 Magnetic nanoparticles

The focus of this work is to investigate the uptake of magnetic nanoparticles in order to be applied for hyperthermia. Hyperthermia is a method to heal the cancer disease by increasing the temperature of cells in order to shrink and weak or kill the cancer cells. The magnetic nanoparticles (magnetite) are used in this project. The nanoparticles were synthesized by a wet chemical method (coprecipitation method) using hydrolysis of two iron salts, ferric chloride and ferrous sulphate, and coprecipitation by ammonium hydroxide and at the end coated with APTES (aminosilane) which increases the biocompatibility and stability of nanoparticles. Transmission electron microscopy (TEM) and dynamic light scattering are used to give information about the size, shape, and stability of nanoparticles. The results shows that particles are round-shaped having a size of about 10 nm which implies also the particles are in the superparamagnetic range. It is also shown that the particles are stable in liquid after coating. The fourier transform infrared (FTIR) spectrometer and X-ray diffraction are used to identify the components and crystalline structure of magnetic nanoparticles respectively. The comparison of FTIR results of MNP and APTES-MNP proves the presence of amino-silane structure on the surface of magnetite NP. The XRD pattern also confirm the cubic inverse structure of both MNP and APTES-MNP. The vibrating sample magnetometer (VSM) are carried out to determine the magnetic properties of magnetite nanoparticles and the measured saturation magnetization is 60.4 A.m^2.kg^{-1}. The hysteresis loop is closed which is a prove of superparamagnetic nanoparticles.

Magnetic nanoparticles uptake We investigated in vitro cellular uptake of magnetite and aminosilane coated magnetite nanoparticles by cancer prostate cells (PC3) and prostate benign cells (BPH1). Intracellular uptake of particles to cells was investigated by transmission

electron microscopy and flow cytometer. It was demonstrated that cellular uptake of particles is cell type dependent. It was also shown that prostate cancer cells take up the coated nanoparticles with a significantly higher level than benign cells which are considered as normal cells. Our experiments also indicated higher uptake of uncoated particles by BPH1 cells which totally concluded in the very efficient effect of functionalization of the NP and cell type behavior. By consideration of TEM measurement, it has not observed any interaction between NP and cell organelles.

Outlook The goal of the project is to apply nanoparticles locally to the cancer cells which increase the efficiency of heat to the cancer cells. The measurements are all carried on *in vivo* environment. That is why the next step is to apply AC-magnetic field to the treated cells (Hyperthermia). By this way we can optimize the exact concentration of our particles that have to be used fo hyperthermia. It is also interesting to examine the effect of our nanoparticles not only on prostate cancer cell but also another cancer cells can be tested.

6.2 Magnetotactic Bacteria

In this project two kinds of magnetotactic bacteria, magnetospirillum magnetotacticum (MS-1) and magnetospirillum gryphiswaldense (MSR-1), are studied and used for the experiments. The bacteria is cultivated, enriched, and extracted. MSR-1 bacteria shows better productivity because of less sensitivity to the oxygen. This situation prepares useful condition for cultivation of MSR-1 compared to MS-1 which is more sensitive to oxygen. The results from TEM measurements present higher concentration of MSR-1 rather that MS-1. The size of particles are mostly in the range of 30 to 60 nm. The magnetic nanoparticles obtained from bacteria are the perfect candidate for hyperthermia because of their membrane which protect them from agglomeration. In the TEM images the membrane of nanoparticles can be seen and no agglomeration is observed.

Outlook The higher concentration of magnetospirillum gryphiswaldense production makes them the better candidate for hyperthermia. It is still needed to optimize the cultivation of bacteria by improving the cultivation method. After that more measurement techniques can characterize their properties such as FTIR, DLS, and XRD. The cell-particles interaction is also the next step in this way.

APPENDIX

Medium 380 and 140 preparation according to DSMZ company description.

380. MAGNETOSPIRILLUM MEDIUM

KH_2PO_4	0.68	g
$NaNO_3$	0.12	g
L(+)-Tartaric acid	0.37	g
Succinic acid	0.37	g
Na-acetate	0.05	g
Vitamin solution (see medium 141)	10.00	ml
Trace element solution (see medium 141)	5.00	ml
Fe(III) quinate solution (see below)	2.00	ml
Agar (BD Bacto, for semi-solid medium)	1.30	g
Na-resazurin solution (0.1% w/v)	0.50	ml
Na-thioglycolate	0.05	g
Distilled water	1000.00	ml

Dissolve ingredients (except thioglycolate) in the order given and adjust pH to 6.75 with NaOH.
Preparation of liquid medium: Sparge medium with 100% N_2 gas for 30 -45 min and dispense under the same gas atmosphere into anoxic Hungate-type tubes to 50% of their volume. Seal vials with screw caps and gas tight butyl rubber closures. Autoclave at 121°C for 15 min. Before inoculation add thioglycolate from a 0.5% (w/v) stock solution, freshly prepared under 100% N_2 gas and filter-sterilized. Then add sterile air (with hypodermic syringe through the rubber closure) to a concentration of 2.5% (v/v) O_2 in the vial (e.g., add 2 ml air to a Hungate-type tube of 16 ml total volume).
Preparation of semi solid medium: Supplement medium with agar, bring medium to the boil and cool under 100% N_2 gas atmosphere. Dispense under same gas atmosphere aliquots of 10 ml semi-solid medium into Hungate-type tubes. Prior to inoculation add thioglycolate from a 0.5% (w/v) stock solution, freshly prepared under 100% N_2 gas and filter-sterilized. Then add sterile air (with hypodermic syringe through the rubber closure) to a concentration of 2.5% (v/v) in the vial.

Note: Prior to inoculation media should be slightly pink in color. Strongly reduced conditions will not support growth of microaerophilic Magnetospirillum *species. Use as inoculum 10% (v/v). Incubate tubes with medium without agitation in an inclined position. During growth O_2 will be consumed and the pH will increase. If higher densities of magnetic cells are wanted, feed oxygen (by adding air), succinic acid and ferric quinate from sterile stock solutions (maintain pH below 7).* ***For cultivation of magnetic cells we recommend preparation of liquid medium, while semi-solid medium is more suitable for demonstration of microaerophilic band formation and storage.***

Continued next page

Ferric Quinate Solution, 0.01 M :

$FeCl_3$ x 6 H_2O	4.50	g
Quinic acid	1.90	g
Distilled water	1000.00	ml

Sterilize by filtration under 100% N_2 gas atmosphere.

For DSM 6361 increase the amount of added O_2 to a concentration of 5% (v/v) in the vial (e.g., add 4 ml sterile air to a Hungate-type tube of 16 ml total volume).

141. METHANOGENIUM MEDIUM (H_2/CO_2)

KCl	0.34	g
$MgCl_2$ x 6 H_2O	4.00	g
$MgSO_4$ x 7 H_2O	3.45	g
NH_4Cl	0.25	g
$CaCl_2$ x 2 H_2O	0.14	g
K_2HPO_4	0.14	g
NaCl	18.00	g
Trace element solution (see below)	10.00	ml
$Fe(NH_4)_2(SO_4)_2$ x 6 H_2O solution (0.1% w/v)	2.00	ml
Na-acetate	1.00	g
Yeast extract (OXOID)	2.00	g
Trypticase peptone (BD BBL)	2.00	g
Na-resazurin solution (0.1% w/v)	0.50	ml
$NaHCO_3$	5.00	g
Vitamin solution (see below)	10.00	ml
L-Cysteine-HCl x H_2O	0.50	g
Na_2S x 9 H_2O	0.50	g
Distilled water	1000.00	ml

Dissolve ingredients (except bicarbonate, vitamins, cysteine and sulfide), sparge medium with 80% H_2 and 20% CO_2 gas mixture for 30 – 45 min to make it anoxic. Add and dissolve bicarbonate and adjust pH to 7.0, then dispense medium under 80% H_2 and 20% CO_2 gas atmosphere into anoxic Hungate-type tubes or serum vials and autoclave. After sterilization add cysteine and sulfide from sterile anoxic stock solutions autoclaved under 100% N_2 gas. Vitamins are prepared under 100% N_2 gas atmosphere and sterilized by filtration. Adjust pH of complete medium to 6.8 – 7.0, if necessary. For incubation use sterile 80% H_2 and 20% CO_2 gas mixture at two atmospheres of pressure.
Note: If the medium is being used without overpressure then adjust pH with a small amount of sterile anoxic 1 N HCl, if necessary.

Continued on next page

Trace element solution:

Nitrilotriacetic acid	1.50	g
$MgSO_4$ x 7 H_2O	3.00	g
$MnSO_4$ x H_2O	0.50	g
NaCl	1.00	g
$FeSO_4$ x 7 H_2O	0.10	g
$CoSO_4$ x 7 H_2O	0.18	g
$CaCl_2$ x 2 H_2O	0.10	g
$ZnSO_4$ x 7 H_2O	0.18	g
$CuSO_4$ x 5 H_2O	0.01	g
$KAl(SO_4)_2$ x 12 H_2O	0.02	g
H_3BO_3	0.01	g
Na_2MoO_4 x 2 H_2O	0.01	g
$NiCl_2$ x 6 H_2O	0.03	g
Na_2SeO_3 x 5 H_2O	0.30	mg
Na_2WO_4 x 2 H_2O	0.40	mg
Distilled water	1000.00	ml

First dissolve nitrilotriacetic acid and adjust pH to 6.5 with KOH, then add minerals. Adjust final to pH 7.0 with KOH.

Vitamin solution:

Biotin	2.00	mg
Folic acid	2.00	mg
Pyridoxine-HCl	10.00	mg
Thiamine-HCl x 2 H_2O	5.00	mg
Riboflavin	5.00	mg
Nicotinic acid	5.00	mg
D-Ca-pantothenate	5.00	mg
Vitamin B_{12}	0.10	mg
p-Aminobenzoic acid	5.00	mg
Lipoic acid	5.00	mg
Distilled water	1000.00	ml

For DSM 1498 and DSM 22353 adjust pH to 6.5.

For DSM 2373 increase the amount of trypticase to 6.00 g/l.

For DSM 4254 add a filter-sterilized, anoxic solution of L-histidine to a final concentration of 80.00 mg/l.

Continued on next page

For DSM 7268 and DSM 7466 use only one atmosphere overpressure of sterile 80% H_2 and 20% CO_2 gas mixture.

For DSM 15219, DSM 18860 and DSM 21220 adjust pH to 7.5.

For DSM 15558 supplement medium after autoclaving with 0.50 g/l coenzyme M (2-mercaptoethanesulfonic acid) added from a filter-sterilized anoxic stock solution prepared under 100% N_2 gas. Adjust pH to 6.5 and use only one atmosphere overpressure of sterile 80% H_2 and 20% CO_2 gas mixture.

For DSM 16458 supplement medium after autoclaving with 0.50 g/l coenzyme M (2-mercaptoethanesulfonic acid) added from a filter-sterilized anoxic stock solution prepared under 100% N_2 gas. Adjust pH to 7.5 and use only one atmosphere overpressure of sterile 80% H_2 and 20% CO_2 gas mixture.

BIBLIOGRAPHY

[1] Dieter Vollath. *Nanomaterials*. Wiley-Vch, 2013.

[2] Sergey P Gubin. *Magnetic nanoparticles*. John Wiley & Sons, 2009.

[3] Mathias Getzlaff. *Fundamentals of magnetism*. Springer Science & Business Media, 2007.

[4] Robert C O'handley. *Modern magnetic materials: principles and applications*. Wiley, 2000.

[5] Nicola A Spaldin and Neil D Mathur. Magnetic materials: fundamentals and device applications. *Physics Today*, 56(12):62–63, 2003.

[6] Unyong Jeong, Xiaowei Teng, Yong Wang, Hong Yang, and Younan Xia. Superparamagnetic colloids: controlled synthesis and niche applications. *Advanced Materials*, 19(1):33–60, 2007.

[7] Nicola A Spaldin. *Magnetic materials: fundamentals and applications*. Cambridge University Press, 2010.

[8] Charles Kittel, Paul McEuen, and Paul McEuen. *Introduction to solid state physics*, volume 8. Wiley New York, 1996.

[9] Wei Wu, Zhaohui Wu, Taekyung Yu, Changzhong Jiang, and Woo-Sik Kim. Recent progress on magnetic iron oxide nanoparticles: synthesis, surface functional strategies and biomedical applications. *Science and technology of advanced materials*, 16(2):023501, 2015.

[10] Roberta Brayner, Fernand Fiévet, and Thibaud Coradin. *Nanomaterials: A Danger Or a Promise?*. Springer, 2014.

[11] An-Hui Lu, E emsp14L Salabas, and Ferdi Schüth. Magnetic nanoparticles: synthesis, protection, functionalization, and application. *Angewandte Chemie International Edition*, 46(8):1222–1244, 2007.

[12] CB Murray, Shouheng Sun, Hugh Doyle, and T Betley. Monodisperse 3d transition-metal (co, ni, fe) nanoparticles and their assembly intonanoparticle superlattices. *Mrs Bulletin*, 26(12):985–991, 2001.

[13] Gunter Schmid et al. *Nanoparticles*. Wiley VCH, 2005.

[14] Louis Néel. Théorie du traînage magnétique des ferromagnétiques en grains fins avec applications aux terres cuites. *Ann. géophys.*, 5:99–136, 1949.

[15] William Fuller Brown Jr. Thermal fluctuations of a single-domain particle. *Physical Review*, 130(5):1677, 1963.

[16] Sergey P Gubin. *Magnetic nanoparticles*. John Wiley & Sons, 2009.

[17] RM Cornell and U Schwertmann. The iron oxide. *VCH, New York*, 377, 1996.

[18] Ajay Kumar Gupta and Mona Gupta. Synthesis and surface engineering of iron oxide nanoparticles for biomedical applications. *Biomaterials*, 26(18):3995–4021, 2005.

[19] Morteza Mahmoudi, Shilpa Sant, Ben Wang, Sophie Laurent, and Tapas Sen. Superparamagnetic iron oxide nanoparticles (spions): development, surface modification and applications in chemotherapy. *Advanced drug delivery reviews*, 63(1-2):24–46, 2011.

[20] Sophie Laurent, Delphine Forge, Marc Port, Alain Roch, Caroline Robic, Luce Vander Elst, and Robert N Muller. Magnetic iron oxide nanoparticles: synthesis, stabilization, vectorization, physicochemical characterizations, and biological applications. *Chemical reviews*, 108(6):2064–2110, 2008.

[21] Rene Massart. Magnetic fluids and process for obtaining them, May 11 1982. US Patent 4,329,241.

[22] Ang Bee Chin and Iskandar Idris Yaacob. Synthesis and characterization of magnetic iron oxide nanoparticles via w/o microemulsion and massart's procedure. *Journal of materials processing technology*, 191(1-3):235–237, 2007.

[23] Soon Gu Kwon, Yuanzhe Piao, Jongnam Park, Subramanian Angappane, Younghun Jo, Nong-Moon Hwang, Je-Geun Park, and Taeghwan Hyeon. Kinetics of monodisperse iron oxide nanocrystal formation by "heating-up" process. *Journal of the American Chemical Society*, 129(41):12571–12584, 2007.

[24] Guido Ennas, ANNA Musinu, G Piccaluga, D Zedda, D Gatteschi, C Sangregorio, JL Stanger, G Concas, and G Spano. Characterization of iron oxide nanoparticles

in an fe2o3- sio2 composite prepared by a sol- gel method. *Chemistry of Materials*, 10(2):495–502, 1998.

[25] German Salazar-Alvarez, Mamoun Muhammed, and Andrei A Zagorodni. Novel flow injection synthesis of iron oxide nanoparticles with narrow size distribution. *Chemical engineering science*, 61(14):4625–4633, 2006.

[26] Carlos Pecharromán, T Gonzalez-Carreno, and Juan E Iglesias. The infrared dielectric properties of maghemite, γ-fe 2 o 3, from reflectance measurement on pressed powders. *Physics and Chemistry of Minerals*, 22(1):21–29, 1995.

[27] YL Wang, ZC Deng, GS Fu, Y Zhou, LZ Chu, and YC Peng. The average size of si nanoparticles prepared by pulsed laser ablation in the gas mixture of he/ar, ne/ar or he/ne. *Thin Solid Films*, 515(4):1897–1900, 2006.

[28] Dennis A Bazylinski, Richard B Frankel, Brigid R Heywood, Stephen Mann, John W King, Percy L Donaghay, and Alfred K Hanson. Controlled biomineralization of magnetite (fe (inf3) o (inf4)) and greigite (fe (inf3) s (inf4)) in a magnetotactic bacterium. *Applied and environmental microbiology*, 61(9):3232–3239, 1995.

[29] D Schüler and Richard B Frankel. Bacterial magnetosomes: microbiology, biomineralization and biotechnological applications. *Applied Microbiology and Biotechnology*, 52(4):464–473, 1999.

[30] Ajay Kumar Gupta and Stephen Wells. Surface-modified superparamagnetic nanoparticles for drug delivery: preparation, characterization, and cytotoxicity studies. *IEEE transactions on nanobioscience*, 3(1):66–73, 2004.

[31] SW Charles. Magnetic fluids (ferrofluids). In *Magnetic Properties of Fine Particles*, pages 267–276. Elsevier, 1992.

[32] Ajay Kumar Gupta and Adam SG Curtis. Lactoferrin and ceruloplasmin derivatized superparamagnetic iron oxide nanoparticles for targeting cell surface receptors. *Biomaterials*, 25(15):3029–3040, 2004.

[33] Robert S Molday. Magnetic iron-dextran microspheres, June 5 1984. US Patent 4,452,773.

[34] George C Hadjipanayis and Richard W Siegel. *Nanophase materials: Synthesis-properties-applications*, volume 260. Springer Science & Business Media, 2012.

[35] Carl E Sjøgren, Karen Briley-Sæbø, Maj Hanson, and Christer Johansson. Magnetic characterization of iron oxides for magnetic resonance imaging. *Magnetic resonance in medicine*, 31(3):268–272, 1994.

[36] Albert F Cotton, Geoffrey Wilkinson, Manfred Bochmann, and Carlos A Murillo. *Advanced inorganic chemistry*. Wiley, 1999.

[37] RM Cornel and U Shwertmann. Iron oxides in the laboratory. preparation and characterization. *VCH Editions, Weinhein, Germany*, 1991.

[38] DK Kim, Y Zhang, W Voit, KV Rao, and Mamoun Muhammed. Synthesis and characterization of surfactant-coated superparamagnetic monodispersed iron oxide nanoparticles. *Journal of Magnetism and Magnetic Materials*, 225(1-2):30–36, 2001.

[39] Pablo Cubillas and Michael W Anderson. Synthesis mechanism: crystal growth and nucleation. *Zeolites and Catalysis: Synthesis, Reactions and Applications*, pages 1–55, 2010.

[40] D Kashchiev. Nucleation: basic theory with applications. 1ª edição, 2000.

[41] Nguyen TK Thanh, N Maclean, and S Mahiddine. Mechanisms of nucleation and growth of nanoparticles in solution. *Chemical reviews*, 114(15):7610–7630, 2014.

[42] Deniz Erdemir, Alfred Y Lee, and Allan S Myerson. Nucleation of crystals from solution: classical and two-step models. *Accounts of chemical research*, 42(5):621–629, 2009.

[43] Tadao Sugimoto. Underlying mechanisms in size control of uniform nanoparticles. *Journal of colloid and interface science*, 309(1):106–118, 2007.

[44] Wei Wu, Quanguo He, and Changzhong Jiang. Magnetic iron oxide nanoparticles: synthesis and surface functionalization strategies. *Nanoscale research letters*, 3(11):397, 2008.

[45] S Palmacci, L Josephson, and EVUS Groman. Patent 5,262,176, 1995. In *Chem. Abstr*, volume 122, page 309897, 1996.

[46] Yong Zhang, Nathan Kohler, and Miqin Zhang. Surface modification of superparamagnetic magnetite nanoparticles and their intracellular uptake. *Biomaterials*, 23(7):1553–1561, 2002.

[47] LM Lacava, ZGM Lacava, MF Da Silva, O Silva, SB Chaves, Ricardo Bentes de Azevedo, Fernando Pelegrini, C Gansau, N Buske, D Sabolovic, et al. Magnetic resonance of a dextran-coated magnetic fluid intravenously administered in mice. *Biophysical journal*, 80(5):2483–2486, 2001.

[48] P Mulvaney, LM Liz-Marzan, M Giersig, and T Ung. Silica encapsulation of quantum dots and metal clusters. *Journal of Materials Chemistry*, 10(6):1259–1270, 2000.

[49] Pedro Tartaj, Teresita Gonzalez-Carreno, and Carlos J Serna. Single-step nanoengineering of silica coated maghemite hollow spheres with tunable magnetic properties. *Advanced Materials*, 13(21):1620–1624, 2001.

[50] Chunfu Zhang, Björn Wängler, Bernd Morgenstern, Hanswalter Zentgraf, Michael Eisenhut, Harald Untenecker, Ralf Krüger, Ralf Huss, Christian Seliger, Wolfhard Semmler, et al. Silica-and alkoxysilane-coated ultrasmall superparamagnetic iron oxide particles: a promising tool to label cells for magnetic resonance imaging. *Langmuir*, 23(3):1427–1434, 2007.

[51] Jun Lin, Weilie Zhou, A Kumbhar, J Wiemann, Jiye Fang, EE Carpenter, and CJ O'connor. Gold-coated iron (fe@ au) nanoparticles: synthesis, characterization, and magnetic field-induced self-assembly. *Journal of Solid State Chemistry*, 159(1):26–31, 2001.

[52] Min Chen, Saeki Yamamuro, Dorothy Farrell, and Sara A Majetich. Gold-coated iron nanoparticles for biomedical applications. *Journal of applied physics*, 93(10):7551–7553, 2003.

[53] AI Lesnikovich, TM Shunkevich, VN Naumenko, SA Vorobyova, and MV Baykov. Dispersity of magnetite in magnetic liquids and the interaction with a surfactant. *Journal of Magnetism and Magnetic Materials*, 85(1-3):14–16, 1990.

[54] Kenneth E Kellar, Dennis K Fujii, Wolfgang HH Gunther, Karen Briley-Sæbø, Marga Spiller, and Seymour H Koenig. 'nc100150', a preparation of iron oxide nanoparticles ideal for positive-contrast mr angiography. *Magnetic Resonance Materials in Physics, Biology and Medicine*, 8(3):207–213, 1999.

[55] Kenneth E Kellar, Dennis K Fujii, Wolfgang HH Gunther, Karen Briley-Sæbø, Atle Bjørnerud, Marga Spiller, and Seymour H Koenig. Nc100150 injection, a preparation of optimized iron oxide nanoparticles for positive-contrast mr angiography. *Journal of Magnetic Resonance Imaging*, 11(5):488–494, 2000.

[56] M Yamaura, RL Camilo, LC Sampaio, MA Macedo, M Nakamura, and HE Toma. Preparation and characterization of (3-aminopropyl) triethoxysilane-coated magnetite nanoparticles. *Journal of Magnetism and Magnetic Materials*, 279(2-3):210–217, 2004.

[57] Aranzazu del Campo, Tapas Sen, Jean-Paul Lellouche, and Ian J Bruce. Multifunctional magnetite and silica–magnetite nanoparticles: synthesis, surface activation and applications in life sciences. *Journal of Magnetism and Magnetic Materials*, 293(1):33–40, 2005.

[58] Stéphane Mornet, Josik Portier, and Etienne Duguet. A method for synthesis and functionalization of ultrasmall superparamagnetic covalent carriers based on maghemite and dextran. *Journal of magnetism and magnetic materials*, 293(1):127–134, 2005.

[59] Randy De Palma, Sara Peeters, Margriet J Van Bael, Heidi Van den Rul, Kristien Bonroy, Wim Laureyn, Jules Mullens, Gustaaf Borghs, and Guido Maes. Silane ligand exchange to make hydrophobic superparamagnetic nanoparticles water-dispersible. *Chemistry of Materials*, 19(7):1821–1831, 2007.

[60] Xing-Can Shen, Xiu-Zhong Fang, Ying-Hua Zhou, and Hong Liang. Synthesis and characterization of 3-aminopropyltriethoxysilane-modified superparamagnetic magnetite nanoparticles. *Chemistry Letters*, 33(11):1468–1469, 2004.

[61] Ming Ma, Yu Zhang, Wei Yu, Hao-ying Shen, Hai-qian Zhang, and Ning Gu. Preparation and characterization of magnetite nanoparticles coated by amino silane. *Colloids and Surfaces A: physicochemical and engineering aspects*, 212(2-3):219–226, 2003.

[62] Richard B Frankel and Richard P Blakemore. Magnetite and magnetotaxis in microorganisms. *Bioelectromagnetics: Journal of the Bioelectromagnetics Society, The Society for Physical Regulation in Biology and Medicine, The European Bioelectromagnetics Association*, 10(3):223–237, 1989.

[63] Dirk Schüler. Molecular analysis of a subcellular compartment: the magnetosome membrane in magnetospirillum gryphiswaldense. *Archives of microbiology*, 181(1):1–7, 2004.

[64] Richard B Frankel, Dennis A Bazylinski, Mark S Johnson, and Barry L Taylor. Magneto-aerotaxis in marine coccoid bacteria. *Biophysical journal*, 73(2):994–1000, 1997.

[65] Damien Faivre and Dirk Schuler. Magnetotactic bacteria and magnetosomes. *Chemical reviews*, 108(11):4875–4898, 2008.

[66] Dennis A Bazylinski and Richard B Frankel. Magnetosome formation in prokaryotes. *Nature Reviews Microbiology*, 2(3):217, 2004.

[67] Dirk Schüler. *Magnetoreception and magnetosomes in bacteria*, volume 3. Springer Science & Business Media, 2006.

[68] Karl Heinz Schleifer, Dirk Schüler, Stefan Spring, M Weizenegger, R Amann, Wolfgang Ludwig, and Manfred Köhler. The genus magnetospirillum gen. nov. description of magnetospirillum gryphiswaldense sp. nov. and transfer of aquaspirillum magnetotacticum to magnetospirillum magnetotacticum comb. nov. *Systematic and Applied Microbiology*, 14(4):379–385, 1991.

[69] D Schüler and M Köhler. The isolation of a new magnetic spirillum. *Zentralblatt für Mikrobiologie*, 147(1-2):150–151, 1992.

[70] Tadashi Matsunaga, Toshifumi Sakaguchi, and Fumihiko Tadakoro. Magnetite formation by a magnetic bacterium capable of growing aerobically. *Applied Microbiology and Biotechnology*, 35(5):651–655, 1991.

[71] Tadashi Matsunaga, Yoshiko Okamura, Yorikane Fukuda, Aris Tri Wahyudi, Yaeko Murase, and Haruko Takeyama. Complete genome sequence of the facultative anaerobic magnetotactic bacterium magnetospirillum sp. strain amb-1. *DNA research*, 12(3):157–166, 2005.

[72] Bruce M Moskowitz. Biomineralization of magnetic minerals. *Reviews of geophysics*, 33(S1):123–128, 1995.

[73] DL Balkwill, D Maratea, and RP Blakemore. Ultrastructure of a magnetotactic spirillum. *Journal of Bacteriology*, 141(3):1399–1408, 1980.

[74] Shouheng Sun, Christopher B Murray, Dieter Weller, Liesl Folks, and Andreas Moser. Monodisperse fept nanoparticles and ferromagnetic fept nanocrystal superlattices. *science*, 287(5460):1989–1992, 2000.

[75] MM Miller, GA Prinz, S-F Cheng, and S Bounnak. Detection of a micron-sized magnetic sphere using a ring-shaped anisotropic magnetoresistance-based sensor: a model for a magnetoresistance-based biosensor. *Applied Physics Letters*, 81(12):2211–2213, 2002.

[76] Tapan K Jain, Marco A Morales, Sanjeeb K Sahoo, Diandra L Leslie-Pelecky, and Vinod Labhasetwar. Iron oxide nanoparticles for sustained delivery of anticancer agents. *Molecular pharmaceutics*, 2(3):194–205, 2005.

[77] Igor Chourpa, Laurence Douziech-Eyrolles, Lazare Ngaboni-Okassa, Jean-François Fouquenet, Simone Cohen-Jonathan, Martin Soucé, Hervé Marchais, and Pierre Dubois. Molecular composition of iron oxide nanoparticles, precursors for magnetic drug targeting, as characterized by confocal raman microspectroscopy. *Analyst*, 130(10):1395–1403, 2005.

[78] Jeff WM Bulte and Michel MJ Modo. *Molecular and cellular MR imaging*. CRC Press, 2007.

[79] Jeff WM Bulte. Intracellular endosomal magnetic labeling of cells. In *Magnetic Resonance Imaging*, pages 419–439. Springer, 2006.

[80] Patricia Berger, Nicholas B Adelman, Katie J Beckman, Dean J Campbell, Arthur B Ellis, and George C Lisensky. Preparation and properties of an aqueous ferrofluid. *Journal of Chemical Education*, 76(7):943, 1999.

[81] Ângela Andrade, Roberta Ferreira, José Fabris, and Rosana Domingues. Coating nanomagnetic particles for biomedical applications. In *Biomedical Engineering-Frontiers and Challenges*. InTech, 2011.

[82] Paul R Stauffer, Thomas C Cetas, and Roger C Jones. System for producing localized hyperthermia in tumors through magnetic induction heating of ferromagnetic implants. *Natl Cancer Inst Monogr*, 61:483–487, 1982.

[83] Ivan A Brezovich, William J Atkinson, and Michael B Lilly. Local hyperthermia with interstitial techniques. *Cancer research*, 44(10 Supplement):4752s–4756s, 1984.

[84] P Wust, B Hildebrandt, G Sreenivasa, B Rau, J Gellermann, H Riess, R Felix, and PM Schlag. Hyperthermia in combined treatment of cancer. *The lancet oncology*, 3(8):487–497, 2002.

[85] Bert Hildebrandt, Peter Wust, Olaf Ahlers, Annette Dieing, Geetha Sreenivasa, Thoralf Kerner, Roland Felix, and Hanno Riess. The cellular and molecular basis of hyperthermia. *Critical reviews in oncology/hematology*, 43(1):33–56, 2002.

[86] Ole Steen Nielsen, M Horsman, and J Overgaard. A future for hyperthermia in cancer treatment? *European Journal of Cancer*, 37(13):1587–1589, 2001.

[87] Stéphane Mornet, Sébastien Vasseur, Fabien Grasset, and Etienne Duguet. Magnetic nanoparticle design for medical diagnosis and therapy. *Journal of materials chemistry*, 14(14):2161–2175, 2004.

[88] Jill Van der Zee. Heating the patient: a promising approach? *Annals of oncology*, 13(8):1173–1184, 2002.

[89] Paul Moroz, Stephen K Jones, Jillean Winter, and Bruce N Gray. Targeting liver tumors with hyperthermia: ferromagnetic embolization in a rabbit liver tumor model. *Journal of surgical oncology*, 78(1):22–29, 2001.

[90] RK Gilchrist, Richard Medal, William D Shorey, Russell C Hanselman, John C Parrott, and C Bruce Taylor. Selective inductive heating of lymph nodes. *Annals of surgery*, 146(4):596, 1957.

[91] RT Gordon, JR Hines, and D Gordon. Intracellular hyperthermia a biophysical approach to cancer treatment via intracellular temperature and biophysical alterations. *Medical Hypotheses*, 5(1):83–102, 1979.

[92] RW Rand, HD Snow, L Lagasse, and WJ Brown. Thermomagnetic surgery for cancer. In *RADIATION RESEARCH*, volume 94, pages 567–568. RADIATION RESEARCH SOC 2021 SPRING RD, STE 600, OAK BROOK, IL 60521, 1983.

[93] Daniel CF Chan, Dmitri B Kirpotin, and Paul A Bunn Jr. Synthesis and evaluation of colloidal magnetic iron oxides for the site-specific radiofrequency-induced hyperthermia of cancer. *Journal of Magnetism and Magnetic Materials*, 122(1-3):374–378, 1993.

[94] A Jordan, R Scholz, P Wust, H Fähling, J Krause, W Wlodarczyk, B Sander, Th Vogl, and R Felix. Effects of magnetic fluid hyperthermia (mfh) on c3h mammary carcinoma in vivo. *International Journal of Hyperthermia*, 13(6):587–605, 1997.

[95] Andreas Jordan, Regina Scholz, Klaus Maier-Hauff, Manfred Johannsen, Peter Wust, Jacek Nadobny, Hermann Schirra, Helmut Schmidt, Serdar Deger, Stefan Loening, et al. Presentation of a new magnetic field therapy system for the treatment of human solid tumors with magnetic fluid hyperthermia. *Journal of magnetism and magnetic materials*, 225(1-2):118–126, 2001.

[96] James R Oleson, Robert S Heusinkveld, and Michael R Manning. Hyperthermia by magnetic induction: Ii. clinical experience with concentric electrodes. *International Journal of Radiation Oncology• Biology• Physics*, 9(4):549–556, 1983.

[97] Martin A Funovics, Barbara Kapeller, Christoph Hoeller, Henry S Su, Rainer Kunstfeld, Stephan Puig, and Karin Macfelda. Mr imaging of the her2/neu and 9.2. 27 tumor antigens using immunospecific contrast agents. *Magnetic resonance imaging*, 22(6):843–850, 2004.

[98] Xiang-Hong Peng, Ximei Qian, Hui Mao, Andrew Y Wang, et al. Targeted magnetic iron oxide nanoparticles for tumor imaging and therapy. *International journal of nanomedicine*, 3(3):311, 2008.

[99] Rita E Serda, Natalie L Adolphi, Marco Bisoffi, and Laurel O Sillerud. Targeting and cellular trafficking of magnetic nanoparticles for prostate cancer imaging. *Molecular imaging*, 6(4):7290–2007, 2007.

[100] Pol-Edern Le Renard, Olivier Jordan, Antonin Faes, Alke Petri-Fink, Heinrich Hofmann, Daniel Ruefenacht, Frederik Bosman, Franz Buchegger, and Eric Doelker. The in vivo performance of magnetic particle-loaded injectable, in situ gelling, carriers for the delivery of local hyperthermia. *Biomaterials*, 31(4):691–705, 2010.

[101] Akira Ito, Masashige Shinkai, Hiroyuki Honda, and Takeshi Kobayashi. Medical application of functionalized magnetic nanoparticles. *Journal of bioscience and bioengineering*, 100(1):1–11, 2005.

[102] UO Hafeli. Magnetic nano and microparticles for targeted drug delivery. *MML SERIES*, 8:77, 2006.

[103] Sophie Laurent, Silvio Dutz, Urs O Häfeli, and Morteza Mahmoudi. Magnetic fluid hyperthermia: focus on superparamagnetic iron oxide nanoparticles. *Advances in colloid and interface science*, 166(1-2):8–23, 2011.

[104] Rudolf Hergt, Silvio Dutz, Robert Müller, and Matthias Zeisberger. Magnetic particle hyperthermia: nanoparticle magnetism and materials development for cancer therapy. *Journal of Physics: Condensed Matter*, 18(38):S2919, 2006.

[105] Ronald E Rosensweig. Heating magnetic fluid with alternating magnetic field. *Journal of magnetism and magnetic materials*, 252:370–374, 2002.

[106] Andreas Jordan, Regina Scholz, Peter Wust, Hermann Schirra, Thomas Schiestel, Helmut Schmidt, and Roland Felix. Endocytosis of dextran and silan-coated magnetite nanoparticles and the effect of intracellular hyperthermia on human mammary carcinoma cells in vitro. *Journal of Magnetism and Magnetic materials*, 194(1-3):185–196, 1999.

[107] Natalia L Chaves, Irina Estrela-Lopis, Julia Böttner, Claudio AP Lopes, Bruna C Guido, Aparecido R de Sousa, and Sônia N Báo. Exploring cellular uptake of iron oxide nanoparticles associated with rhodium citrate in breast cancer cells. *International journal of nanomedicine*, 12:5511, 2017.

[108] Sulin Zhang, Huajian Gao, and Gang Bao. Physical principles of nanoparticle cellular endocytosis. *ACS nano*, 9(9):8655–8671, 2015.

[109] Andre E Nel, Lutz Mädler, Darrell Velegol, Tian Xia, Eric MV Hoek, Ponisseril Somasundaran, Fred Klaessig, Vince Castranova, and Mike Thompson. Understanding biophysicochemical interactions at the nano–bio interface. *Nature materials*, 8(7):543, 2009.

[110] Amir Ata Saie, Moumita Ray, Morteza Mahmoudi, and Vincent M Rotello. Engineering the nanoparticle-protein interface for cancer therapeutics. In *Nanotechnology-based precision tools for the detection and treatment of cancer*, pages 245–273. Springer, 2015.

[111] Fatemeh Madani, Staffan Lindberg, Ülo Langel, Shiroh Futaki, and Astrid Gräslund. Mechanisms of cellular uptake of cell-penetrating peptides. *Journal of biophysics*, 2011, 2011.

[112] Li Shang, Karin Nienhaus, and Gerd Ulrich Nienhaus. Engineered nanoparticles interacting with cells: size matters. *Journal of nanobiotechnology*, 12(1):5, 2014.

[113] Dagmar A Kuhn, Dimitri Vanhecke, Benjamin Michen, Fabian Blank, Peter Gehr, Alke Petri-Fink, and Barbara Rothen-Rutishauser. Different endocytotic uptake mechanisms for nanoparticles in epithelial cells and macrophages. *Beilstein journal of nanotechnology*, 5:1625, 2014.

[114] Lennart Treuel, Xiue Jiang, and Gerd Ulrich Nienhaus. New views on cellular uptake and trafficking of manufactured nanoparticles. *Journal of the Royal Society Interface*, 10(82):20120939, 2013.

[115] Sara Salatin and Ahmad Yari Khosroushahi. Overviews on the cellular uptake mechanism of polysaccharide colloidal nanoparticles. *Journal of cellular and molecular medicine*, 21(9):1668–1686, 2017.

[116] Jia Hu and Yaling Liu. Cyclic strain enhances cellular uptake of nanoparticles. *Journal of Nanomaterials*, 16(1):291, 2015.

[117] Liangke Zhang, Shixiang Hou, Shengjun Mao, Dapeng Wei, Xiangrong Song, and Yi Lu. Uptake of folate-conjugated albumin nanoparticles to the skov3 cells. *International journal of pharmaceutics*, 287(1-2):155–162, 2004.

[118] Hae Yun Nam, Seok Min Kwon, Hyunjin Chung, Seung-Young Lee, Seung-Hae Kwon, Hyesung Jeon, Yoonkyung Kim, Jae Hyung Park, Joon Kim, Songwook Her, et al. Cellular uptake mechanism and intracellular fate of hydrophobically modified glycol chitosan nanoparticles. *Journal of Controlled Release*, 135(3):259–267, 2009.

[119] Lay Hong Chuah, Clive J Roberts, Nashiru Billa, Syahril Abdullah, and Rozita Rosli. Cellular uptake and anticancer effects of mucoadhesive curcumin-containing chitosan nanoparticles. *Colloids and Surfaces B: Biointerfaces*, 116:228–236, 2014.

[120] Wim H De Jong and Paul JA Borm. Drug delivery and nanoparticles: applications and hazards. *International journal of nanomedicine*, 3(2):133, 2008.

[121] Sara Salatin, Solmaz Maleki Dizaj, and Ahmad Yari Khosroushahi. Effect of the surface modification, size, and shape on cellular uptake of nanoparticles. *Cell biology international*, 39(8):881–890, 2015.

[122] Huijie Zhang, Tomohiko Yamazaki, Chunyi Zhi, and Nobutaka Hanagata. Identification of a boron nitride nanosphere-binding peptide for the intracellular delivery of cpg oligodeoxynucleotides. *Nanoscale*, 4(20):6343–6350, 2012.

[123] El Hadji Mamour Sakho, Elaheh Allahyari, Oluwatobi S. Oluwafemi, Sabu Thomas, and Nandakumar Kalarikkal. Chapter 2 - dynamic light scattering (dls). In Sabu Thomas, Raju Thomas, Ajesh K. Zachariah, and Raghvendra Kumar Mishra, editors, *Thermal and Rheological Measurement Techniques for Nanomaterials Characterization*, Micro and Nano Technologies, pages 37 – 49. Elsevier, 2017.

[124] David B Williams and C Barry Carter. The transmission electron microscope. In *Transmission electron microscopy*, pages 3–17. Springer, 1996.

[125] P. Scherrer. Bestimmung der Größe und der inneren Struktur von Kolloidteilchen mittels Röntgenstrahlen. *Nachrichten von der Gesellschaft der Wissenschaften zu Göttingen, Mathematisch-Physikalische Klasse*, 1918:98–100, 1918.

[126] Simon Foner. Versatile and sensitive vibrating-sample magnetometer. *Review of Scientific Instruments*, 30(7):548–557, 1959.

[127] JA Gerber, WL Burmester, and David J Sellmyer. Simple vibrating sample magnetometer. *Review of Scientific Instruments*, 53(5):691–693, 1982.

[128] Stéphane Mornet, Sébastien Vasseur, Fabien Grasset, and Etienne Duguet. Magnetic nanoparticle design for medical diagnosis and therapy. *Journal of materials chemistry*, 14(14):2161–2175, 2004.

[129] Wilfried Andrä and Hannes Nowak. *Magnetism in medicine*. Akademie Verlag, 1998.

[130] BR Kirupakar, BA Vishwanath, and MP Sree. Vibrating sample magnetometer and its application in characterisation of magnetic property of the anti cancer drug magnetic microspheres. *International Journal of Pharmaceutics and Drug Analysis*, 4:227–233, 2016.

[131] Eric Jones, Sam Michael, and G Sitta Sittampalam. Basics of assay equipment and instrumentation for high throughput screening. 2016.

[132] Robert-Jan Bleichrodt and Nick D Read. Flow cytometry and facs applied to filamentous fungi. *Fungal Biology Reviews*, 2018.

[133] RM Zucker, EJ Massaro, KM Sanders, LL Degn, and WK Boyes. Detection of tio2 nanoparticles in cells by flow cytometry. *Cytometry Part A*, 77(7):677–685, 2010.

[134] Quan Wu, Ying Zhou, Linfeng Chen, Jiandang Shi, Chun-Yu Wang, Lin Miao, Helmut Klocker, Irwin Park, Chung Lee, and Ju Zhang. Benign prostatic hyperplasia (bph) epithelial cell line bph-1 induces aromatase expression in prostatic stromal cells via prostaglandin e2. *Journal of Endocrinology*, 195(1):89–94, 2007.

[135] Thermo Fisher Scientific. Cell culture basics handbook. *UK: Gibco*, 2015.

[136] L. Schwengels. Ultraschallunterstützte gewinnung magnetischer nanopartikel aus magnetotaktischen bakterien, bachelor thesis. 2017.

[137] Maryam Youhannayee, Saeideh Nakhaei-Rad, Fereshteh Haghighi, Karsten Klauke, Christoph Janiak, Mohammad Reza Ahmadian, Robert Rabenalt, Peter Albers, and Mathias Getzlaff. Physical characterization and uptake of iron oxide nanoparticles of different prostate cancer cells. *Journal of Magnetism and Magnetic Materials*, 2018.

[138] Ayman Atta, Hamad Al-Lohedan, and Sami Al-Hussain. Functionalization of magnetite nanoparticles as oil spill collector. *International journal of molecular sciences*, 16(4):6911–6931, 2015.

[139] Asahi Tomitaka, Atsuo Hirukawa, Tsutomu Yamada, Shin Morishita, and Yasushi Takemura. Biocompatibility of various ferrite nanoparticles evaluated by in vitro cytotoxicity assays using hela cells. *Journal of Magnetism and Magnetic Materials*, 321(10):1482–1484, 2009.

[140] Rudolf Allmann and Arnt Kern. *Röntgen-Pulverdiffraktometrie: Rechnergestützte Auswertung, Phasenanalyse und Strukturbestimmung (German Edition)*. Springer, 2002.

[141] J. M. Henke. Einfluss verschiedener herstellungsverfahren auf die eigenschaften magnetischer nanopartikel. *Bachelor thesis*, 2018.

[142] Tim Mosmann. Rapid colorimetric assay for cellular growth and survival: application to proliferation and cytotoxicity assays. *Journal of immunological methods*, 65(1-2):55–63, 1983.

[143] S. Fuchs. Synthesis and characterization of magnetite nanoparticles with aminosilane coating. *Bachelor thesis*, 2016.

[144] Soshin Chikazumi and Chad D Graham. *Physics of Ferromagnetism 2e*, volume 94. Oxford University Press on Demand, 2009.

[145] Andreas Kaiser, Tingting Liu, Walter Richtering, and Annette M Schmidt. Magnetic capsules and pickering emulsions stabilized by core- shell particles. *Langmuir*, 25(13):7335–7341, 2009.

[146] Igal Levine, Regev Ben Zvi, Moritz Winkler, Annette M Schmidt, and Moshe Gottlieb. Magnetically induced heating in elastomeric nanocomposites-theory and experiment. In *Macromolecular symposia*, volume 291, pages 278–286. Wiley Online Library, 2010.

[147] R Mohr, K Kratz, T Weigel, M Lucka-Gabor, M Moneke, and A Lendlein. Initiation of shape-memory effect by inductive heating of magnetic nanoparticles in thermoplastic polymers. *Proceedings of the National Academy of Sciences*, 103(10):3540–3545, 2006.

[148] Saba Naqvi, Mohammad Samim, MZ Abdin, Farhan Jalees Ahmed, AN Maitra, CK Prashant, and Amit K Dinda. Concentration-dependent toxicity of iron oxide nanoparticles mediated by increased oxidative stress. *International journal of nanomedicine*, 5:983, 2010.

[149] Michael Brown and Carl Wittwer. Flow cytometry: principles and clinical applications in hematology. *Clinical chemistry*, 46(8):1221–1229, 2000.

[150] Jesse S Aaron, Nitin Nitin, Kort Travis, Sonia Kumar, Thomas G Collier, Sun Young Park, Miguel Jose Yacaman, Lezlee Coghlan, Michelle Follen, Rebecca R Richards-Kortum, et al. Plasmon resonance coupling of metal nanoparticles for molecular imaging of carcinogenesis in vivo. *Journal of biomedical optics*, 12(3):034007, 2007.

[151] AM Huízar-Félix, D Muñoz, I Orue, C Magén, A Ibarra, JM Barandiarán, A Muela, and ML Fdez-Gubieda. Assemblies of magnetite nanoparticles extracted from magnetotactic bacteria: A magnetic study. *Applied Physics Letters*, 108(6):063109, 2016.

[152] Edouard Alphandery, Stephanie Faure, Olivier Seksek, François Guyot, and Imene Chebbi. Chains of magnetosomes extracted from amb-1 magnetotactic bacteria for application in alternative magnetic field cancer therapy. *ACS nano*, 5(8):6279–6296, 2011.

PUBLICATIONS

Youhannayee, M. Nakhaei-Rad, S. Haghighi, F. Ahmadian, M. R. Klauke, K. Janiak, C. Rabenalt, R. Albers, P. Getzlaff, M. Investigating of up taking of magnetite nanoparticle by prostate cell lines, Journal of magnetism and magnetic material, 473 (2019) 205-214

CONFERENCE CONTRIBUTIONS

• M. Youhannayee, A. Scheffzyk, A. Jaspers, M. Getzlaff. TMOKE study for characterizing magnetic properties of ferromagnetic thin films. Poster, $DPG - Frühjahrstagung$, Berlin, 2015.

• M. Youhannayee, S. Emelianov, R. Rabenalt, M. Getzlaff. Preparation and physical characterization of magnetite nanoparticles (MNP) with Aminosilane shell. Poster, $DPG - Frühjahrstagung$, Regensburg, 2016.

• S. Emelianov, M. Youhannayee, M. Getzlaff. Magnetic Characterization of Iron Oxide superparamagnetic Nanoparticles on Surfaces. Poster, $DPG - Frühjahrstagung$, Regensburg, 2016.

• A. Jaspers, M. Youhannayee, M. Getzlaff. Magnetic properties of wet-chemically prepared nanoparticles. Poster, $DPG - Frühjahrstagung$, Dresden, 2017.
• L. Schwengels, N. Juric, M. Youhannayee, M. Getzlaff. Extraction of Magnetic Nanoparticles from Magnetotactic Bacteria. Poster, $DPG - Frühjahrstagung$, Dresden, 2017.

• S. Emelianov, M. Youhannayee, M. Getzlaff. Magnetic and morphological characterization of magnetite nanoparticles with ligand shell. Poster, $DPG - Frühjahrstagung$, Dresden, 2017.

• S. Fuchs, M. Youhannayee, M. Getzlaff. Synthesis and charcterization of magnetite nanoparticles with aminosilane coating. Poster, $DPG - Frühjahrstagung$, Dresden, 2017.

• M. Youhannayee, C. Janiak, R. Rabenalt, P. Albers, M. Getzlaff. Preparation and physical characterization of magnetite nanoparticles (MNP) with aminosilane shell. Poster, $SPIE.\ Photonic\ west$, San Francisco, 2017.

• M. Youhannayee, S. Nakhaei Rad, F. Haghighi, M. R. Ahmadian, J. Nothacker, A. Schmidt, A.Barbian, K. Klauke, C.Janiak, R. Rabenalt, P. Albers, and M. Getzlaff. Uptake

of iron oxide nanoparticles of different prostate cancer cells. Talk, $12th\ International\ Conference\ on\ the\ Scientific\ and\ Clinical\ Applications\ of\ Magnetic\ Carriers$, Copenhagen, 2018.

ACKNOWLEDGEMENT

First of all I would like to thank my supervisor Professor Mathias Getzlaff for giving me the opportunity to do my Ph.D. in our group at Heinrich Heine University. I am grateful for his kindness, his motivation, for his valuable suggestions and discussions. I appreciate his extensive supervision and full support which guides me through in my research work.

I would like to express my gratefulness to PD Dr. med. Robert Rabenalt from Urology clinic Düsseldorf as my second supervisor for his kind support and always availability. I want to thank Prof. Dr. med. Peter Albers for his support.

I owe many thanks to Düsseldorf School of Oncology (DSO) and the selection committee for selecting me as a Ph.D. student and the financial support through my work especially and in particular Dr. Cornelia Hoener.

I would also like to thank Junior Scientist and International Research Center (JUNO) of Heinrich Heine University for their financial support through writing my dissertation and in particular Dr. Sigrun Wegener-Feldbrügge and Dr. Gellert for all of their supports during last year of my work.

I must show my gratefulness to Professor Mohammad Reza Ahmadian who gave me the possibility to visit and attend his cellular laboratory at Heinrich Heine University. I want to thanks also his group member Saeideh Nakhaeirad.

Regarding chemical experiences, I want to thank to Professor Christof Janiak who gave me the possibility to visit and attend his laboratory at Heinrich Heine University and thanks to his group member Hajo Meyer, Karsten Klauke, and Birgit Tommes for their cooperations.

I want to thank Professor Anette Schmidt and her group members Ahmad Shabaan and Johanna Nothacker for their valuable cooperation for the hyperthermia and VSM measurements.

A personal thanks to Dr. Andreas Barbian for the helpful discussions and Mrs. Elisabeth

Wesbuer from Anatomy institute who kindly and patiently support me through Cell-TEM measurements.

I am also very thankful to Mrs Niesen from Center of Advance imaging CAi Düsseldorf who always very friendly and kindly helped me for nanoparticles TEM measurements.

For our bacteria cultivation I would like to thank nice help and cooperation of Professor Klaus Pfeffer, Andrea Peter, and Quynh Hoang Bao Nguyen.

I would like to thank to all of my friends who make a lots of good memory in my life story: to Elmira, Niloufar, Rozhin, Maryam, Thomas, Venous, Reza, Mahboobeh, Christiane, Tobias, Hsiao-Ching, Maja.

My special thanks to Torsten one of my best friends, who always supports me endless from the first day.

To all of my students who cooperate very well during their projects: Aniela, Adrian, Thomas, Nadja, Lea, Stephanie, Stanislav, Paula, Fabian, and Jan.

Lastly, but always first in my heart, thanks to my family, to my mother that her love inspired me all the time, to my sister who help me in every second of my life, to my lovely brother, to my sister in law, to my lovely niece and nephew Niki and Mahan and in the end to My father's soul.

Eidesstattliche Versicherung

Ich versichere an Eides statt, dass die Dissertation von mir selbstständig und ohne unzulässige fremde Hilfe unter Beachtung der „Grundsätze zur Sicherung guter wissenschaftlicher Praxis“ an der Heinrich-Heine Universität Düsseldorf erstellt worden ist. Die aus fremden Quellen direkt oder indirekt übernommenen Gedanken sind als solche kenntlich gemacht. Die Arbeit wurde bisher weder im Inland noch im Ausland in gleicher oder ähnlicher Form einer anderen Prüfungsbehörde vorgelegt. Es wurden keine früheren erfolglosen Promotionsversuche unternommen.

Düsseldorf, den 5. Mai 2020

Maryam Youhannayee